NOTICE

AVIS

Canadä

UNIVERSITY OF ALBERTA

ORGANIZED MOTION IN THE ATMOSPHERIC SURFACE LAYER

BY

Yahui Zhuang

(C)

A thesis submitted to the Faculty of Graduate Studies and Research in partial fulfilment of the requirements for the degree of Doctor of Philosophy

IN

METEOROLOGY

Department of Geography

Edmonton, Alberta

Spring 1994

Canada

UNIVERSITY OF ALBERTA

RELEASE FORM

NAME OF AUTHOR: Yahui Zhuang

TITLE OF THESIS: ORGANIZED MOTION IN THE ATMOSPHERIC SURFACE

LAYER
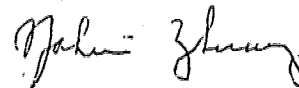
DEGREE : Doctor of Philosophy

YEAR THIS DEGREE GRANTED: 1994

Permission is hereby granted to the University of Alberta library to reproduce single copies of this thesis and to lend or sell such copies for private, scholarly or scientific research purposes only.

Yahui Zhuang

(signature)

P. O. Box 186

Pinawa, Manitoba, Canada

ROE 1L0
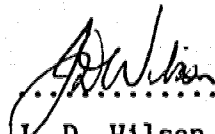
Date: *April 14, 1994*

UNIVERSITY OF ALBERTA
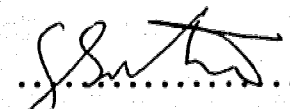
FACULTY OF GRADUATE STUDIES AND RESEARCH

The undersigned certify that they have read, and recommend to the

Faculty of Graduate Studies and Research for acceptance, a thesis

entitled ORGANIZED MOTION IN THE ATMOSPHERIC SURFACE LAYER submitted by

Yahui Zhuang in partial fulfilment of the requirments for the degree of

Doctor of philosophy in METEOROLOGY

J. D. Wilson

E. P. Lozowski

D. J. Wilson

G. E. Swaters

G. Reuter

R. H. Shaw

date: 11. April /94

ABSTRACT

In this thesis, turbulence in the atmospheric surface layer has been studied using "structural" and "deterministic" approaches. The thesis is broken into four papers. The first two papers (Chapters II and III) concern the search for, and interpretation of coherent structures in experimental data. The third and fourth papers (Chapters IV and V) develop and apply a low-order model to study the dynamics and energetics of convective plumes in the atmospheric surface layer.

In Chapter II, experimental data on windbreak flows have been analysed, using several statistical methods. I have proposed and shown that coherent structures DO exist in the mixing region of a porous windbreak (50% porosity) flow, and are largely responsible for the momentum transport that re-accelerates the leeward flow. A comparison between windbreak flow and the laboratory turbulent mixing layer suggests that the dominant structures in these two flows are similar. Some previous numerical and experimental results are interpreted in light of the coherent structures and the self-similar property in the mixing region of a windbreak flow.

In Chapter III, the Shot-Effect method has been used to extract "statistical" coherent structures from velocity and temperature fluctuations measured in the atmospheric surface layer. The extracted coherent structures retain objectively the cross-covariances of velocities and temperature. The transport characteristics of the coherent structures and their variation with atmospheric stratification agree with the common perception of the transport processes in the atmospheric surface layer.

In Chapter IV, based on a simple application of the dynamical systems theory and experimental evidence of coherent motions in the convective atmospheric surface layer, I have developed a low-order model (15 ordinary differential equations) to study coherent flow dynamics, by performing a Galerkin projection of the Navier-Stokes equations on a set of 15 orthogonal functions $\phi(x,z)$, extracted from an ensemble of experimentally observed convective plumes (or coherent structures) with the Proper Orthogonal Decomposition method. These orthogonal functions, defined on a two-dimensional domain (640 m x 150 m), are typical of large-scale turbulent velocity and temperature fluctuations in the convective atmosphere, and are assumed to have embedded enough physics to model the most important aspects of the coherent structures. The effects of the unresolved turbulence on the coherent structures are modelled by the Smagorinsky eddy viscosity closure. This low-order model provides a means to study instantaneous coherent dynamics in the atmospheric surface layer, an aspect not emphasized before.

In Chapter V, budgets of the horizontal and vertical momentum, and of the turbulent kinetic energy associated with vertical motion, within updrafts of convective plumes are evaluated, using experimental observations of the velocities and temperatures within the plumes, and the corresponding pressure fluctuations calculated by the low-order model developed in Chapter IV. Detailed pressure distributions within a convective plume, and the role of the translation velocity in the development of the convective plume are discussed using the simulated flow fields. The force balances revealed by the momentum budget study suggest a shape-preservation mechanism for the plumes, which is consistent with the experimental observations. The transport and

redistribution of turbulent kinetic energy seen from the study of the turbulent kinetic energy budgets explain the relatively long lifetime of the convective plumes. Implications of the transport properties of the convective plumes for modelling atmospheric turbulence and air quality problems are also discussed.

ACKNOWLEDGEMENTS

TABLE OF CONTENTS

Chapter V DYNAMICS AND ENERGETICS OF CONVECTIVE PLUMES IN THE
          ATMOSPHERIC SURFACE LAYER

LIST OF TABLES

LIST OF FIGURES

APPENDICES

LIST OF SYMBOLS

CHAPTER II

H	Height of the fence
k	Turbulent kinetic energy
ΔP	Pressure difference between upstream and downstream of the fence
T	Time
U	Mean wind speed
u, w	Instantaneous flow velocities in alongwind (x) and vertical (z) directions
C_d	Drag coefficient of the fence
$F_n(t)$	Variable matrix used to calculate the covariance function
$f_n(t)$	Signal realization
$f(Hz)$	Frequency
H_0	Hole size used in quadrant analysis
k_r	Resistance coefficient of the fence
$R(t_m, t_k)$	Two-time covariance function
$S(f)$	Power spectrum
u_*	Friction velocity
z_0	Surface roughness
α_n	Expansion coefficients appearing in the Proper Orthogonal Decomposition
β	Incident angle of upstream approaching wind
λ_n	Eigenvalues appearing in the Proper Orthogonal Decomposition
k_v	Eddy viscosity
σ	An empirical constant
σ_u, σ_w	Standard deviations of velocities u and w.
$\phi_n(t)$	Orthogonal functions appearing in the Proper Orthogonal Decomposition
τ	Momentum flux
η	The similarity variable used in mixing layer scaling (dimensionless)
erf	Error function
Sk	Skewness
Kurt	Kurtosis

CHAPTER III

L	Monin-Obukhov length
T	Time
u, w	Velocity components in alongwind (x) and vertical (z) directions, respectively
$F_n(z_m, t)$	A velocity and temperature matrix used to calculate the covariance function
$f_i(z_m, t)$	A deterministic function or coherent structure for variable i
R	A two-point, two-time covariance function
H_0	Hole size used in Quadrant analysis
σ_u, σ_w	Standard deviations of u and w, respectively.
ϕ_n	Eigenfunctions resulting from the Proper Orthogonal Decomposition

CHAPTER IV

$A_i(t)$	Generalized expansion coefficients or the generalized coordinates of a flow in phase space
B	A 15 x 15 matrix consisting the expansion coefficients $\alpha_{i,j}$
c	An empirical constant used in eddy diffusivity model
C(r)	Correlation dimension of a dynamical system in phase space
c_{ij}, c_{ijk}	The coefficients of the low-order model
E	A 768 x 15 matrix consisting the 15 eigenfunctions
E^i	Momentum equations for u or w, or thermodynamic energy equation
F	A 15 x 768 matrix consisting of velocities and temperatures of the 15 selected coherent structures
$F(k_m,z)$	Fourier Transform of the variable $f(x,t)$
$F_i()$	A generalized ordinary differential function decomposed from the Navier-Stokes equations
$F_m(x,z)$	A composite matrix of velocities and temperature
$f(x,t)$	An instantaneous flow variable (velocity or temperature)
G()	A Nth order nonlinear function of a phase variable
g	Gravitational acceleration
H(x)	The Heaviside function
K_h	Eddy diffusivity for heat
K_m	Eddy diffusivity for momentum
N_p	Total samples of phase variables constructed from experimental data.
p	Pressure
P_r	Turbulent Prandtl number
$R(\Delta x, \Delta z)$	Two-point covariance matrix formed using $F_m(x,z)$
T	Temperature
t	Time
u,w	Velocity components in alongwind (x) and vertical (z) directions
$X(t_i,M)$	A vector phase variable of embedding dimension M
$\alpha_j(t)$	Phase space coordinates of the low-order model
$\phi_j^i(x,z)$	The ith component of the jth eigenfunction
θ	Temperature fluctuation
λ	Eigenvalues
ρ	Density
τ	Delay time used to construct phase space from experimental data
τ_{ij}	The Reynolds stress due to subgrid turbulence
Π	Pressure forcing in the low-order model
~	Instantaneous value
—	Horizontal mean
{}	Small volume average
'	fluctuation

CHAPTER I

INTRODUCTION

In recent years, attempts to better understand atmospheric turbulence, and demands to minimize uncertainty in air quality modelling, have placed an increasing emphasis on the study of instantaneous plumes or coherent structures, in the convective atmosphere. The occurrence of the coherent structures strongly influences higher-order velocity statistics and pressure fluctuations. For example, an analysis of experimental data by Hunt et al. (1988) showed that the variability of the vertical velocity within plume updrafts produces more than half of the contribution to the total (unconditional) variance $\overline{w^2}$ and to the third moment $\overline{w^3}$. Wilczak and Businger (1984) found that the pressure perturbations associated with the coherent structures are essentially responsible for the pressure-velocity and pressure-temperature covariances in the ensemble-average budget equations for the momentum, heat and turbulent kinetic energy, in the convective atmospheric surface layer.

Higher-order statistics and pressure perturbations are difficult to measure in experiments. Yet turbulent transport (vertical derivatives of triple-velocity correlations) and pressure covariances, important processes in many turbulent flows, must be parameterized in ensemble-average turbulence models (Zeman, 1981). The effects of the convective plumes have not been considered or well parameterized in most ensemble-average turbulence models. For example, lack of understanding of the pressure perturbations (larg-y contributed by the thermal plumes) is one of the reasons that ad hoc adjustments of

1

pressure covariance terms in the second-order closure are necessary in order to model convective atmospheric turbulence (Zeman, 1981; Wyngaard, 1984). Thus, successful modelling of atmospheric turbulence requires insight into mechanisms, particularly the large-scale coherent dynamics, which are invisible from the ensemble average perspective.

In this thesis, coherent structures in the atmospheric surface layer have been investigated along structural and deterministic lines in four separate studies. In Chapters II and III, several statistical methods are used to extract coherent structures from turbulence records, measured in a windbreak flow, and in an undisturbed atmospheric surface layer. The dynamics of these coherent structures are discussed in terms of their role in the transport of momentum and heat. The transport properties of coherent structures in windbreak flow offer an explanation for the success of a numerical simulation using the Reynolds equations (Wilson 1985), and for some previous experimental observations. The "statistical" coherent structures in the atmospheric surface layer and the variation of their transport characteristics with atmospheric stratification are demonstrated by the Shot-Effect method (Lumley 1981). The results agree with the common perceptions of turbulent transport in the atmospheric surface layer.

In Chapter IV, the observed coherent structures in the convective atmospheric surface layer are embodied into a mathematical framework, and a low-order model for studying coherent dynamics is developed. This low-order model is based on the recent understanding of turbulent structure provided by the dynamical systems theory (Ruelle and Takens 1971). This so-called "deterministic" study of turbulence claims that solutions of equations for a forced dissipative system, such as that of

the Navier-Stokes equations, are likely attracted to low-dimensional manifolds in phase space (a space where each point corresponds to a solution of the Navier-Stokes equations). These manifolds, which are characterized by their fractal (usually small) dimensions, are called "strange attractors" (Chapman and Tobak, 1987). Due to the nonlinearity of the governing equations, turbulent flows dominated by strange attractors in phase space possess the property of extreme sensitivity to the initial condition. Sensitivity to the initial condition produces randomness in flow variables, and the folding process manifests as intermittency, which may correspond to chaotic coherent motions, i.e., a seemingly chaotic motion could be produced by a simple underlying mechanism. This deterministic view of turbulence provides a hope to study the dynamics of coherent structures with a low-order model.

A simple analysis of turbulence data measured in the atmospheric surface layer, taking the dynamical systems point of view, suggests that coherent structures in the convective atmospheric surface layer may be described by a low-order dynamic model. A low-order model is then derived by projecting the Navier-Stokes equations along a set of basis functions, the latter obtained by performing a Proper Orthogonal Decomposition (Lumley 1981) on the experimental data. The orthogonal functions, defined on a two-dimensional domain (640 m x 150 m), are typical of large-scale velocity and temperature fluctuations in the convective atmosphere, and are assumed to have embedded enough physics to model the most important aspects of the coherent structures. The effects of the unresolved turbulence on the coherent structures are modelled by the eddy viscosity closure. The model treats boundary

conditions objectively, uses experimental data as the initial conditions, and provides a means to study the time-dependent behaviour of a coherent structure, an aspect not emphasized before.

In Chapter V, budgets of the horizontal and vertical momentum, and of the vertical component of the turbulent kinetic energy, within updrafts of convective plumes, are evaluated using experimental observations of the velocities and temperatures within the plumes, and the corresponding pressure fluctuations calculated by the low-order model developed in Chapter IV. The convective plumes are found to be characterized by strong turbulent and pressure transport (i.e., local equilibrium does not prevail). The phase relationships observed between pressure and velocity fluctuations within the convective plumes minimise energy redistribution between alongwind (u) and vertical (w) motion by the agency of pressure fluctuations. Such a decoupling of u and w effectively inhibits vertical transport of alongwind momentum in the convective atmosphere, and allows a convective plume to exist as an anisotropic identity for a relatively long time (i.e., a time of order of a few times necessary to travel its own length).

Detailed pressure fields within a convective plume, and the role of the translation velocity in the development of the convective plume, are discussed using the simulated flow fields. The transport characteristics and pressure distributions of the persistent convective plumes revealed in this study provide information that could be useful for improving atmospheric turbulence modelling, and for understanding the uncertainty in air quality problems.

References

Chapman, G.T., and M. Tobak, 1987: Observations, theoretical ideas, and modeling of turbulent flows --- past, present, and future. In Theoretical Approaches to Turbulence. eds. Dwoyer, D.L., M.Y. Hussaini, and R.G. Voigt. Springer-Verlag, New York.

Hunt, J.C.R., J.C. Kaimal and J.E. Gaynor, 1988: Eddy Structure in the Convective Boundary Layer - New Measurements and New Concepts. Q. J. R. Meteorol., Soc. 114, 827-858.

Ruelle, D., and F. Takens, 1971: On the nature of turbulence. Comm. Math. Phys., 82, 137-151.

Lumley, J.L., 1981: Coherent structures in turbulence. In trans. and turb. R.E. Meyer, ed., Academic Press, 215-241.

Wilczak, J.M., and J.A. Businger, 1984: Large-scale eddies in the unstably stratified atmospheric surface layer. Part II: turbulent pressure fluctuations and the budgets of heat flux, stress and turbulent kinetic energy. J. Atmos. Sci. 41, 3551-3567

Wilson, J.D., 1985: Numerical studies of flow through a windbreak. J. Wind Eng. and Indust. Aerodynamics. 21, 119-154.

Wyngaard, J.J., 1984: Large-Eddy simulation: Guidelines for its application to planetary boundary layer reserach. U.S. Army Research Office. Contract No. 0804.

Wyngaard, J.C., 1988: Structure of the PBL. In Lectures on Air pollution Modelling. A. Venkatram and J.C. Wyngaard, eds, Ameri. Meteorol. Soc., 9-61.

Zeman, O., 1981: Progress in the modeling of planetary boundary layers. Ann. Rev. Fluids Mech., 13, 253-272.

CHAPTER II

COHERENT MOTIONS IN WINDBREAK FLOW

1. Introduction

A windbreak, i.e., a wall-mounted fence, represents a simple example of a two-dimensional bluff obstacle. The flow behind the fence, influenced strongly by the aerodynamic interaction between the fence and the upstream wind field (the fence exerts a form drag force[1] on the wind field), is characterized by strong velocity and pressure gradients in both horizontal and vertical directions (Plate, 1971: Bradley and Mulhearn, 1983).

Intuitively, a windbreak flow is likely to be a flow where coherent motions play an important role. However, ensemble-average turbulence models, which ignore the existence of coherent motion, have had some success in describing windbreak flows: for example, Wilson (1985) showed that the mean wind and some second order statistics of a windbreak flow can be simulated reasonably well at least close to the windbreak with a second-order closure model. It is a curiosity about structures and their possible role in a windbreak flow that has resulted in this study.

All previous studies of windbreak flows concerned ensemble-average properties, such as the attenuation of mean wind and turbulence by fences. Plate (1971) reviewed several aerodynamic aspects of a solid windbreak flow and demonstrated its complexity by dividing the flow

_____

1. Defined as $D = 0.5 C_d \rho H U_h^2$, where C_d is the drag coefficient, ρ the air density and U_h the approaching wind speed at the fence height H.

6

into seven regions, each having different aerodynamic factors acting on it. In particular, Plate used a control volume to analyse alongwind momentum loss in the flow over a fence, and proposed a theoretical model relating windbreak drag to the leeward mean velocity field.

Using wind directions and fluctuations observed with a rotating vanes (which are of cause not sensitive to fast fluctuations), Baltaxe (1967) showed clearly in the lee of fences the presence of large-scale flow patterns, which varied with porosity of the fences, and disappeared when the porosity of the fences is larger than 25%. Raine and Stevenson (1977) demonstrated the domination of the downstream flow by the fence-top generated turbulence, using measurements of turbulence intensity and spectra of the alongwind velocity downstream of the fences. Mulhearn and Bradley (1977) found, in their wind tunnel experiment, that the mean flow and momentum transport downstream of porous fences are very sensitive to the incident wind direction. In addition, it has been shown that a number of other factors, such as terrain roughness and the approaching wind profile can also influence the downstream turbulence field (Plate, 1971).

Although it seems to have been generally accepted in previous studies that fence-top generated large-scale motions could be important in downstream flow, especially in the case of a solid fence, no study reported has discussed the detailed momentum transport processes associated with them, or explicitly taken into account their effects on downstream flow development. We feel that some of the experimental observations may be better understood from the instantaneous and structural points of view. It is with the large-scale structure in the

downstream mixing region (Figure 1), and its role on downstream flow development, that the present study is concerned.

In this study, experimental data from earlier authors (Mulhearn and Bradley, 1977; Bradley and Mulhearn, 1983), and from our own experiments to specifically investigate coherent structures in the windbreak flow, will be used. By examining the long-time turbulence statistics and the instantaneous flow structure, we will show that coherent structures DO exist, and make a substantial contribution to momentum transport in the mixing region of a windbreak (50% porosity) flow. A comparison between windbreak flows and the laboratory turbulent mixing layer (Brown and Roshko, 1974) will demonstrate that the momentum transport achieved by the dominant structures in these two flows is similar, although a windbreak flow is more complex because of the unsteadiness (on long time scales) of the wind speed in the atmosphere, and the presence of the ground. Such a comparison suggests that, as in the turbulent mixing layer, the windbreak flow is self-similar in the mixing region, i.e., "motions at different sections differ only in velocity and length scales, and are dynamically similar in these aspects of controlling mean velocity and Reynolds stress" (Townsend, 1976).

We believe that coherent motions in the mixing region of a windbreak flow have a major influence on important aspects of the flow, such as intermittent flow reversal (observed behind dense windbreaks; Baltaxe, 1967), and the rate of downstream flow recovery. Wilson's (1985) numerical simulation, and some previous field observations of windbreak flow will be discussed in light of the self-similar property and the observed coherent motions.

2. The Ellerslie experiment and data analysis

Our experiment was conducted at Ellerslie, Alberta, in the summer of 1989. A plastic fence (90 m long and 2.34 m high) was erected in an open field (Figure 1). The porosity of the fence was 50%, and its resistance coefficient ($k_r = \Delta P/\rho U^2$), measured in a wind tunnel, was 1.66. The upstream fetch of uniform and level terrain was about 1 km. The surface was covered by long grass of about 30 cm. A log-law fit to an upstream wind profile measured under near neutral stratification yielded a surface roughness, $z_0 \simeq 0.1$ m.

The instrumentation included two 3-dimensional sonic anemometers (Applied Tech. Inc., 25-cm path length), two 1-dimensional sonic anemometers (Campbell Sci. Corp., 10 cm path length) and five cup anemometers. Using the sonic anemometers, time series of (u, v, w) were sampled at 20 Hz, at points both upstream and downstream (mostly in the mixing region). In some cases the cup anemometers were mounted on the upstream tower to measure the approaching mean wind profile U(z). In other cases, the mean wind profiles and turbulent fluctuations (u,v,w) were measured simultaneously at the downstream tower. Data acquisition was accomplished by an analogue-to-digital converter coupled to a personal computer.

Since the heat flux was not measured, the Monin-Obukhov length, listed in Table 1, was crudely estimated using the flux-gradient relationships, i.e., $\kappa z/u_*$ $\partial U/\partial z = \phi_m(z/L)$ (Dyer, 1974) from the the upstream mean wind profiles and weather conditions (used to determine the atmospheric stability condition) recorded nearby at the Edmonton

International Airport. A total of 15 hours of data were collected under different atmospheric stability conditions. The long path length of the three-dimensional sonics filtered high frequency turbulent fluctuations, but these have no relevance to the present study of large-scale turbulence. To check the quality of the data, the mean horizontal velocity $\overline{\sqrt{u^2+v^2}}$ according to the sonic anemometer(s) was compared with that of the cup anemometer(s) at the same location(s). We accepted the sonic data provided the discrepancy was less than 10%. To minimize the influence of unsteadiness in wind direction on the data analysis, only the data collected under "steady" wind conditions, characterized by a small standard deviation of the wind direction ($\sigma_\beta \lesssim$ 20°), have been selected (Table 1).

2.1 Long-time statistics revealing organization and gustiness behind a windbreak

To examine the role of coherent motion in a windbreak flow, we have assumed that if the postulated structures exist, and have persistent and important impact on the flow, their effect should be seen not only in the instantaneous flow field, but also in the long-time statistics.

Table 1 lists some turbulence statistics both upstream and downstream of the windbreak. Most runs included simultaneous measurements by sonic anemometers upstream and downstream. The ratio of the momentum flux ($-\overline{uw}$) to the turbulent kinetic energy (k), $-\overline{uw}/k$, measures the effectiveness of the turbulence in terms of momentum transport (Townsend, 1976). Upstream, on average, $-\overline{uw}/k = 0.14$, which is consistent with the value measured by Hogstrom (1990) in the

atmospheric surface layer, while in the downstream mixing region this ratio is considerably larger. The variations of $-\overline{uw}/k$ upstream are perhaps due to changes in atmospheric stability and boundary-layer depth. The variations downstream are attributed to variations in the incident wind direction, sensor location, and atmospheric stability etc. Also notable in Table 1 is the significant difference between the skewness (Sk_w) of the vertical velocities upstream and downstream. Sk_w is generally positive upstream, which agrees with previous observations for the atmospheric surface layer (e.g., Hunt et al., 1988). But, large negative values of Sk_w were seen in most of the observations made in the mixing region (runs 4, 5, 6 and 7), indicating strong sweeping motions (or gusts). Note that since most of the runs lasted more than 15 minutes, during which time the wind conditions vary, the effect of changing wind directions was averaged into the quantities in Table 1.

Figures 2(a,b) show spectra of the fluctuating alongwind component (u) and the momentum flux (-uw), calculated for run 4, upstream and in the downstream mixing region. Upstream, the u spectrum peaks at considerably lower frequency than the -uw co-spectrum, which is consistent with the study by Kaimal et al. (1972). Downstream, the peak of the u-spectrum has moved to higher frequency, which agrees with a previous observation by Ogawa and Diosey (1980). The peaks in the u and -uw spectra are much closer together downstream than upstream. It is obvious from Figure 2(a) that upstream, some of the low-frequency content of the u-component does not contribute to momentum transport, although it does contribute substantially to the turbulent kinetic energy. Therefore, upstream, the Reynolds stress and turbulent kinetic energy may not be "carried by" the same "eddies" (Townsend, 1978).

This agrees with the notion that there is a considerable amount of "inactive" motion (Hogstrom, 1990) in the atmospheric surface layer. However in the downstream mixing region, the turbulent alongwind fluctuations are fully involved in momentum transport, resulting in the increased value of $-\overline{uw}/k$ seen in Table 1. In the atmospheric surface layer, spectra are greatly influenced by the unsteadiness of the advecting wind, in addition to the "phase scrambling" (Yule, 1980) of the eddies themselves; thus, no further attempt to infer the eddy structures has been based on spectral analysis.

The effective momentum transport seen in the long-time statistics and spectral characteristics shown above is presumably caused by increased organization and gustiness in the downstream flow. To reveal the coherent motion we hypothesize to exist, in the following sections, conditional sampling and statistical methods will be used to extract (any) coherent motion from the measured velocity time series, and to reveal its role in the momentum transport process. We will not be able to show the spatial characteristics of the coherent motion because of the very limited data available, but the temporal character will be obtained. Since run 4 and run 7 (Table 1) were measured when the wind conditions were relatively steady, they have been selected for analyzing upstream and downstream flows respectively.

2.2 Quadrant analysis

Quadrant analysis (Willmarth and Lu, 1974) is a method to sort momentum transport into sweep (u > 0, w < 0), ejection (u < 0, w > 0), inward interaction (u < 0, w < 0) and outward interaction (u > 0, w > 0) events. By doing so, and progressively filtering out smaller events (|uw| < threshold value), one may identify large intermittent events that make a strong contribution to the momentum transport. Readers are referred to Appendix A for a brief description of Quadrant analysis. Here Quadrant analysis is used to study the structure of the Reynolds stress -uw, from the instantaneous u and w signals measured in run 4 of our experiments.

Upstream and downstream structures of the Reynolds stress obtained using the quadrant analysis are shown in Figures 3. Upstream, the transport process is relatively symmetric, i.e., sweeps and ejections contribute equally and positively to the Reynolds stress, and inward and outward interactions contribute equally and negatively to the Reynolds stress. But downstream, the Reynolds stress is clearly dominated by sweeps. At large values of the hole size, H_0, when one selects lower frequency events with large Reynolds stress, this dominance becomes dramatic. For example, at H_0 = 10 the Reynolds stress is essentially produced by the sweep event alone, and represents about 37% of the total Reynolds stress. Furthermore, that 37% of the total Reynolds stress was found to be produced in less than 5% of the total sample time! The strong sweep motions transfer momentum excess, produced by the strong wind shear above the fence, from upper levels to lower levels, and result in the large negative skewness of the vertical velocity seen in Table 1. The pattern of the downstream Reynolds

stress structure changes little with atmospheric stability conditions. This agrees with Seginer (1974), who found that atmospheric stability has a minimal effect in the near-fence region, where, in our view, the windbreak induced large-scale motions dominate the thermal effect.

2.3 Conditional sampling

To investigate the velocity structures that dominate the Reynolds stress in the downstream flow, the VITA (Variable – Interval Time Averaging) technique (Blackwelder and Kaplan, 1976) will be used to identify "events". The VITA technique supposes that peaks in the short-time variance signal correspond to dramatic events. The short-time variance is defined as

$$VAR(t,T) = \frac{1}{T}\int_{t-T/2}^{t+T/2} x^2(s)ds - \left\{\frac{1}{T}\int_{t-T/2}^{t+T/2} x(s)ds\right\}^2 , \tag{1}$$

where x is a signal fluctuation with its long-term mean subtracted out. When T becomes large the second term on the right-hand side of (1) tends to zero, and the long-time variance, σ_x^2, is obtained. There is a close relation between the integration time T and the time scale of x contributing to the short-time variance. For example, Schols (1984) found that Equation (1) works roughly as a low-pass filter, accepting frequencies below 1/T . On the basis of a visual inspection of the measured velocity time series, it is found that the violent coherent motions usually last between 3 to 5 s. Since we are interested in the velocity structure of the violent sweep motions selected with the quadrant analysis in Section 2.2, which have relatively long time scale, T = 5 s was chosen for the present study.

Instead of using the u velocity component as the event selector (as was the case in most previous applications), the momentum flux, -uw, was used as the controlling VITA variable. This is because, in a laboratory study of a turbulent mixing layer, Bradshaw (1966) found that maximum instantaneous momentum flux occurs during the large eddy pairing process; so events selected by VITA using -uw triggering should correlate well with the large-scale motions.

The events (velocities in a time domain centered at the instant when the maximum of the short-time variance occurs) are selected when VITA exceeds the long-time averaged variance of -uw. The time domain was chosen to be six seconds so that it will cover a complete period of most of the selected events. One hundred events were selected for each upstream and downstream location. The selected events contributed about 70% of the momentum flux in about 50% of the total time, for both upstream and downstream locations.

The major difference between previous applications of the VITA technique and the present study is in the stage of ensemble averaging. It is important to remember that the selected events may contain contributions from a number of scales. Most previous authors formed an arithmetical average of the selected events. But in the atmospheric surface layer, owing to the unsteadiness of the wind, the ensemble-averaged events could be a blurred superposition of the embedded structures, and show no order (Narasimha and Kailas, 1987).

To examine the VITA-selected turbulent events, we have used the method of Proper Orthogonal Decomposition (Lumley, 1967,1981), which is a statistical method widely used to sort from a large set of experimental observations a subset of linear combinations of coherent

patterns contributing maximally to the observed variance. It has been successfully applied in this context to identify coherent motions in turbulent jets (Glauser et al., 1985) and in the wall region of the turbulent boundary layer (Aubry et al., 1988). Here, because of the limited data available, only a simple version of this theory is applied: only the temporal variation of the data will be considered. Details of this theory can be found in Appendix B and the references listed therein, but a very brief description follows.

2.4 Proper orthogonal decomposition

Suppose $f_1(t)$, $f_2(t)$, ..., $f_N(t)$ are N realizations (or events) of a fluctuating signal, each of which can be either a single variable or a composite of variables, sampled periodically at time interval, $\Delta t = (T_2 - T_1)/M$, within the closed domain $[T_1, T_2]$. By requiring a function $\phi(t)$, defined on the domain $[T_1, T_2]$, to resemble in a statistical sense the dominant structure embedded in these realizations, one obtains (Appendix B) for $\phi(t)$ the prescription

$$\sum_{m=0}^{M} R(t_m, t_k)\phi(t_m) = \lambda\phi(t_k) \quad , \qquad (2)$$

where $R(t_m, t_k)$ is the two-time covariance function formed from the N realizations f, which is a (M+1)x(M+1) matrix, and λ is the eigenvalue.

Equation (2) is the well-known problem of determining eigenvalues and eigenvectors of a matrix $R(t_m, t_k)$. Solving this eigenvalue problem (IMSL, 1989), one finds a set of eigenvalues (λ_1, ..., λ_N), ordered such that $\lambda_1 > \lambda_2 > ... > \lambda_N > 0$, and a set of corresponding orthogonal functions ($\phi_1(t)$, ..., $\phi_N(t)$).

Each event can then be reconstructed from the orthogonal functions

$$f_i(t) = \sum_{n=1}^{N} \alpha_{in}\phi_n(t) \qquad (3a)$$

where

$$\alpha_{in} = \sum_{m=0}^{M} f_i(t_m)\phi_n(t_m) \qquad (3b)$$

with different coefficients, α_{in}, for each different event.

For flows having a high degree of organization, this decomposition has been found very effective in the sense that the first few orthogonal functions will retain most of the information in the velocity covariance of the selected events.

To implement the Proper Orthogonal Decomposition to obtain the orthogonal functions, the selected events were block-averaged every 0.1 s, i.e., low-pass filtered, and used to calculate the two-time covariance function

$$R(t_m,t_k) = \frac{1}{N} \sum_{i=1}^{N} F^T_i\ F_i \qquad (3c)$$

where (^{T}) denotes a transpose and F_i is a 1 x 120 matrix: $[u_i(t_1)$, $w_i(t_1)$, ..., $u_i(t_{60})$, $w_i(t_{60})]$, so the covariance, $R(t_m,t_k)$, contains the variances of u and w components, as well as the covariance of u and w.

To be consistent with the objective of investigating the velocity structures that dominate the Reynolds stress, we weighted the selected events with their respective values of the Reynolds stress $W_{uw}(i)$ averaged over the domain $[T_1, T_2]$, when calculating $R(t_m,t_k)$

$$R(t_m,t_k) = \frac{1}{N} \sum_{i=1}^{N} W_{uw}(i)\ F^T_i\ F_i\ . \qquad (3d)$$

Thus, the resulting eigenvectors calculated from (2) emphasize the velocity events not only effectively retaining information in velocity covariance but also making the largest contributions to -uw. Such weighted orthogonal functions have been calculated and used by Mahrt and Frank (1988) in an investigation of the intermittent turbulence at the top of a strongly stratified surface inversion layer.

Figure 4 shows the five most important orthogonal functions extracted from events contributing strongly to the Reynolds stress, for the upstream and downstream turbulence. These five velocity structures contribute more than 50% of the velocity variance of the selected 100 (N) events, and represent, in a decreasing order, the largest scale motions. Upstream, the vertical velocity components are not well correlated with the alongwind components, and have a small amplitude, implying that most momentum transport happens when there is a strong alongwind fluctuation and a weak downdraft. This is expected in the undisturbed atmospheric surface layer, where the horizontal motions dominate. But downstream, u and w have about the same amplitude, and are better correlated within the selected events, implying an effective momentum transport mechanism in the downstream turbulence.

The analysis so far suggests that there ARE strong coherent motions in the mixing region of a windbreak flow. However, our data are too limited to discuss further the coherent motions, their spatial structure, and their role in determining the evolution of a windbreak flow. For this, we will rely on earlier windbreak experiments. In addition, it is noted that the strongly coherent downstream u and w events resemble the velocity measurements from the laboratory turbulent mixing layer, where the primary structures are the transverse vortices

that have strong vertical motions (Latigo, 1979). Thus, if a resemblance (both mean flow and turbulence) between windbreak flow and the turbulent mixing layer can be established, the well known properties of the turbulent mixing layer will shed light on what we may expect to ultimately be revealed as the vortical nature of windbreak flow.

3. A resemblance between windbreak flow and the turbulent mixing layer

A turbulent mixing layer is formed by the sudden interaction of two parallel streams having initially (i.e., at the point of conjunction) distinct and uniform velocities U_1 and U_2. Although the simplest statistical theory of the turbulent mixing layer based on an eddy viscosity is well known (Schlichting, 1968), study of the coherent structures in the turbulent mixing layer has been an active academic problem (Latigo, 1979; Liu, 1989), and has played an important role in research aimed at better understanding of turbulent shear flow. The essential feature of a turbulent mixing layer is the presence of spanwise coherent large-scale vortices, which are believed to be a manifestation of hydrodynamic instability (Ho and Huerre, 1984). Following this primary instability, secondary instabilities introduce three dimensionality into the flow. Roshko (1980) concluded "development of a mixing layer is largely determined by the primary spanwise vortices and the streamwise counter rotating vortex pairs. The Reynolds stress and the growth of the layer are controlled mainly by the primary vortices while the secondary set provides internal mixing and possibly modifies the stress."

For a solid fence, Plate (1971) has demonstrated that the flow near the separation streamline (i.e., a line passing close to the tip of the fence, and dividing the downstream flow into "high" and "low" velocity regions) can be well described by the simplest theory of the turbulent mixing layer, which involves the assumption of an eddy viscosity, k_v, varying linearly with downstream distance x:

$$k_v = \frac{x}{4\sigma^2} (U_1 - U_2). \tag{4}$$

Here U_1 and U_2 are the flow velocities above and below the windbreak, and σ is an empirical constant.

In the case of a porous fence, we would expect that the upper part of the flow field (z > H), which is distorted (relative to the upstream flow) owing to the drag on the fence, would have characteristics similar to the upper layer flow of a solid fence, but with less severe distortion. Theoretical and wind tunnel studies reviewed by Laws and Livesey (1978) have shown that a uniform screen blocking a confined flow always tends to make the downstream wind more uniform. By varying the resistant coefficient k_r the downstream mean velocity profile can be controlled. In addition, with increasing porosity, the mean flow recirculation zone right behind a windbreak becomes weak (Baltaxe, 1967) and the flow in the mixing region will not be affected by the presence of the ground as strongly as in the case of a solid fence. Thus, it is reasonable to assume that in the mixing region of a porous windbreak, the flow has the characteristics of the flow that results if an upper flow with initially uniform velocity, U_1, is joined to a lower flow of velocity U_2.

Experiments (Finnigan and Bradley, 1985) show that there is a small downward curvature in the mean streamline downstream of the windbreak, which is caused by the pressure gradient between ground and the upper layer free stream, i.e., "Coanda" effect (Plate, 1971). Plate pointed out that the Coanda effect is in part responsible for the recovery of the wind profile to the upstream equilibrium condition in solid windbreak flows, but suggested that this effect is probably small for a porous fence. We thus neglect the effect in the following discussions.

To test the hypothesized resemblance of windbreak flow to the turbulent mixing layer flow, we have used the experimental data of Bradley and Mulhearn (1983), who designed a windbreak experiment in the atmospheric surface layer to verify a theory for the wake behind a fence in a boundary layer proposed by Counihan et al. (1974). The fence was 1.2 m in height, with a porosity of 50% and a resistance coefficient $k_r = 2$. Using drag plates, and cup and sonic anemometers, velocity and shear stress profiles were measured at various locations downstream of the fence, under near neutral stability conditions. The patterns of velocity and shear stress downstream were found independent of the upstream wind velocity over the range 5-10 m/s. Figure 5 shows the mean profiles upstream and downstream of the windbreak, reproduced from Bradley and Mulhearn. Immediately behind the windbreak (x/H = 0.8), the wind profile is relatively uniform below windbreak height. The wind profiles in the mixing region (x/H = 8.3, 12.5, 16.7) have been plotted in Figure 6 using the mixing layer scaling. The solid line in Figure 6 is the solution for the velocity profile in a turbulent mixing layer, namely

$$U = \frac{U_1 + U_2}{2} \left\{ 1 + \frac{U_1 - U_2}{U_1 + U_2} \, \mathrm{erf}(\eta) \right\} , \qquad (5)$$

where $\eta = \sigma z/x$ is the similarity variable for the mixing layer. The empirical constant σ was specified as 14.5, as suggested by Plate (1971) for both solid and porous fences; erf is the error function. For our purposes, the speeds U_1 and U_2 have been normalized by the velocity at 4 m. Then $U_1 = 1.0$ while from the wind profile at $x/H = 0.8$, $U_2 = 0.4$. From Eq. (5) the momentum flux τ is calculated as

$$\tau = \rho \, k_v \, \frac{\partial U}{\partial Z} , \qquad (6)$$

which is presented in Fig. 7 along with Bradley and Mulhearn's experimental data at two locations downstream of the windbreak.

Since the data were averaged over many different runs, scatter around the theoretical curves could be partly due to the variation of the atmospheric stability conditions and the incoming wind directions. Qualitative agreement between the experimental data and the theoretical calculations in Figures 6 and 7 indicates that in the mixing region of the windbreak flow, both mean flow and second-order statistics follow (qualitatively) the turbulent mixing layer scaling.

Further evidence of the resemblance between windbreak flow and the turbulent mixing layer can be extracted from Mulhearn and Bradley's (1977) experiment, in which the authors examined the sensitivity of windbreak flow to the incident wind direction in a wind tunnel. Mulhearn and Bradley found that with a decrease of incidence angle in the approaching wind direction (i.e., when the upstream wind is more nearly perpendicular to the fence), the downstream mean wind profiles tend to decrease mostly near and below the windbreak height (i.e, the

velocity difference $U_1 - U_2$ becomes larger), whereas the momentum fluxes tend to increase strongly, especially at heights greater than half of a fence-height. That is, the larger the difference between velocities at upper and lower levels of a windbreak, the stronger the downstream momentum transport will be. This phenomenon is also found in the turbulent mixing layer. From Equations (5) and (6), we obtain

$$\tau = \frac{1}{2} \rho K_v (U_1 - U_2) \frac{\partial}{\partial z} \, erf(\eta) \tag{7}$$

Thus, a mixing layer with a larger velocity difference, $U_1 - U_2$, will transport momentum more effectively.

It seems plausible, from the above comparisons, that the dominant flow structure in the mixing region of a windbreak is similar to a classical turbulent mixing layer. Having established this connection, we will try to explain some of the interesting phenomena of windbreak flows.

4. Discussion and Conclusion

Why do turbulence models, such as the eddy viscosity closure and the second-order closure, which do not explicitly account for the occurrence of coherent motions, lead to fairly reasonable prediction of the mean flow (Wilson, 1985) in what we now know to be an organized windbreak flow ? To address this question, let us recall some experimental evidence on the turbulent mixing layer. Following extensive turbulence measurements in a plane mixing layer, Wygnanski and Fiedler (1970) claimed that "in spite of the complexity of the flow the simple concepts of eddy viscosity and eddy diffusivity appear to be

valid within the turbulent zone." Shih (1984) successfully simulated a turbulent mixing layer using a second-order model. His success, as Lumley (1985) points out, is partly because, in a self-similar flow, all scales of the turbulence respond quickly to the changes in the mean flow field, so the coherent motions transport momentum in much the same way as the "fine grain" turbulence does, and can be described by the gradient transport theory. The self-similar properties of a turbulent mixing layer have been demonstrated by Spencer and Jones (1971) in a wind tunnel experiment where the fluctuating velocities were found to closely follow the mean velocity in attaining similar distribution. In view of the resemblance between windbreak flows and the turbulent mixing layer, the successful numerical simulation of the windbreak flow by Wilson (1985) based on the Reynolds equations is not surprising.

From laboratory experiments we know that the thickness of a turbulent mixing layer at any given x is linearly proportional to the normalized velocity difference, $(U_1 - U_2)/(U_1 + U_2)$ (Browand and Troutt, 1985). On the other hand, from the aerodynamic point of view, the normalized velocity difference between upper and lower levels of a windbreak flow (immediately behind the fence) is determined by parameters such as porosity, incident wind direction, etc. Observations (Raine and Stevenson, 1977) showed that the higher the porosity of the fence, the slower the rate of recovery to the upstream condition in the far wake. Since the mean wind profile downstream is shaped by the momentum transport, in light of what we have shown we can assert that the slow recovery is caused by the fact that with increasing porosity, the normalized velocity difference behind the fence decreases, and the large-scale coherent motions become less

effective and need a longer distance to transport the alongwind momentum required to restore the wind profile to the equilibrium upstream condition. For the same reason, when the incident wind is oblique to the fence, the normalized velocity difference behind the fence is decreased, leading to the reduced momentum transport observed in a windbreak flow (Mulhearn and Bradley, 1977).

Finnigan and Bradley (1983) found that immediately behind a fence, the zone of enhanced turbulent kinetic energy (relative to upstream) covered a deeper vertical region than the zone of enhanced shear stress. Similar differences (although of lesser degree) can be seen in a turbulent mixing layer (Wygnanski and Fiedler, 1970). The narrow zone of the enhanced stress may correspond to the pairing process of the coherent motions, that happens in the region of large velocity gradient. The deeper zone of enhancement of turbulent kinetic energy could be due to the very large eddy (larger than the scale considered here) induced swirling "inactive" motions which are particularly intense in a boundary layer with adverse pressure gradient (dp/dx > 0) (Townsend, 1976), such as in the lee of a windbreak (Plate, 1971). "Inactive" motions contribute little to the Reynolds stress, but comprise a significant part of the turbulent kinetic energy.

Since the drag coefficient of a windbreak, C_d, varies little with atmospheric stability, we do not expect the normalized velocity difference, and consequently the structure of momentum transport in the near wake of a windbreak, to change with atmospheric stability. This has been confirmed by our quadrant analysis, and by the observation of Seginer (1974). The changes in flow pattern in the far wake of a

windbreak flow are however influenced by the local thermal structure, and cannot be easily predicted.

In conclusion, we have shown that coherent motions DO occur in a porous windbreak flow, and argued that they resemble the vortices seen in the laboratory turbulent mixing layer. By virtue of their strong u-w correlation, the coherent motions are largely responsible for the momentum transport that reaccelerates the leeward flow. However, from the modelling point of view, the coherent motions in a windbreak flow, do not pose great difficulties, because of the self-similar properties of the flow in the mixing region.

Acknowledgements

Table 1. Long time statistics of windbreak flow in the Ellerslie experiments.

(a) Upstream measurements (X/H = -15 Z/H = 0.7)

Run (duration)	σ_u^2	Sk_u	$Kurt_u$	σ_w^2	Sk_w	$Kurt_w$	$\overline{-uv}$	$\overline{-uv}/k$	$U_{5.5}$	σ_w/u_*	$\beta°(\sigma_\beta)$ (°)	L (m)
1 (30 min)	1.1	0.3	3.2	0.2	0.1	3.6	0.16	0.14	6.2	1.12	26(12)	102
2 (30 min)	0.42	0.18	2.5	0.06	0.05	4.12	0.04	0.1	3.1	1.22	17(15)	-1
3 (10 min)	0.84	0.45	2.16	0.21	0.19	3.8	0.16	0.17	5.5	1.15	20(16)	166
4 (20 min)	0.47		3.37	0.16	0.87	5.0	0.08	0.14	4.2	1.41	16(11)	-2
5 (15 min)	0.34	0.24	3.51	0.12	0.14	4.41	0.05	0.13	3.1	1.55	?	-42
6 (30 min)	0.38	0.1	2.95	0.08	0.25	4.45	0.06	0.17	3.2	1.15	1(20)	-1
Ave.		0.27	3.11		0.27	4.23		0.14		1.27		

β is the incident angle, which is zero when the wind is perpendicular to the fence.

(b) Downstream measurements (mixing and/or wall regions[*])

Run (duration)	σ_u^2	Sk_u	$Kurt_u$	σ_w^2	Sk_w	$Kurt_w$	$\overline{-uv}$	$\overline{-uv}/k$	$U_{5.5}$	Location	L (m)
1*(30 min)	0.21	0.13	3.40	0.11	-0.34	5.3	-0.02	<0	6.2	X/H=-2.1 Z/H=0.7	102
2*(30 min)	0.06	0.18	3.24	0.04	-0.41	4.7	-0.06	<0	3.1	X/H=-2.1 Z/H=0.7	-1
4 (20 min)	0.2	0.34	3.89	0.15	-0.84	4.6	0.06	0.24	4.2	X/H=-4.2 Z/H=0.7	-2
5 (15 min)	0.25	0.34	3.19	0.07	-0.13	3.70	0.04	0.18	3.1	X/H=-4.2 Z/H=0.7	-42
6 (30 min)	0.18	0.8	3.70	0.11	-0.84	5.42	0.06	0.28	3.2	X/H=-4.2 Z/H=0.7	-1
7*(30 min)	0.89	0.83	3.98	0.47	-0.51	3.60	0.31	0.31	5.6	X/H=-4.2 Z/H=-1.1	44
7*(30 min)	0.22	0.10	4.20	0.10	-0.57	6.30	0.13	0.13	5.6	X/H=-4.2 Z/H=-.36	44

[*] Observations in the wall region, which is bounded by ground and a line extending from the top of the fence to the point x = 15 H. The turbulence in the wall region is assumed to be equilibrium, i.e., turbulent energy production locally balances dissipation.

§ The incident angle and its standard deviation for run 7 are 3° and 10°, respectively.
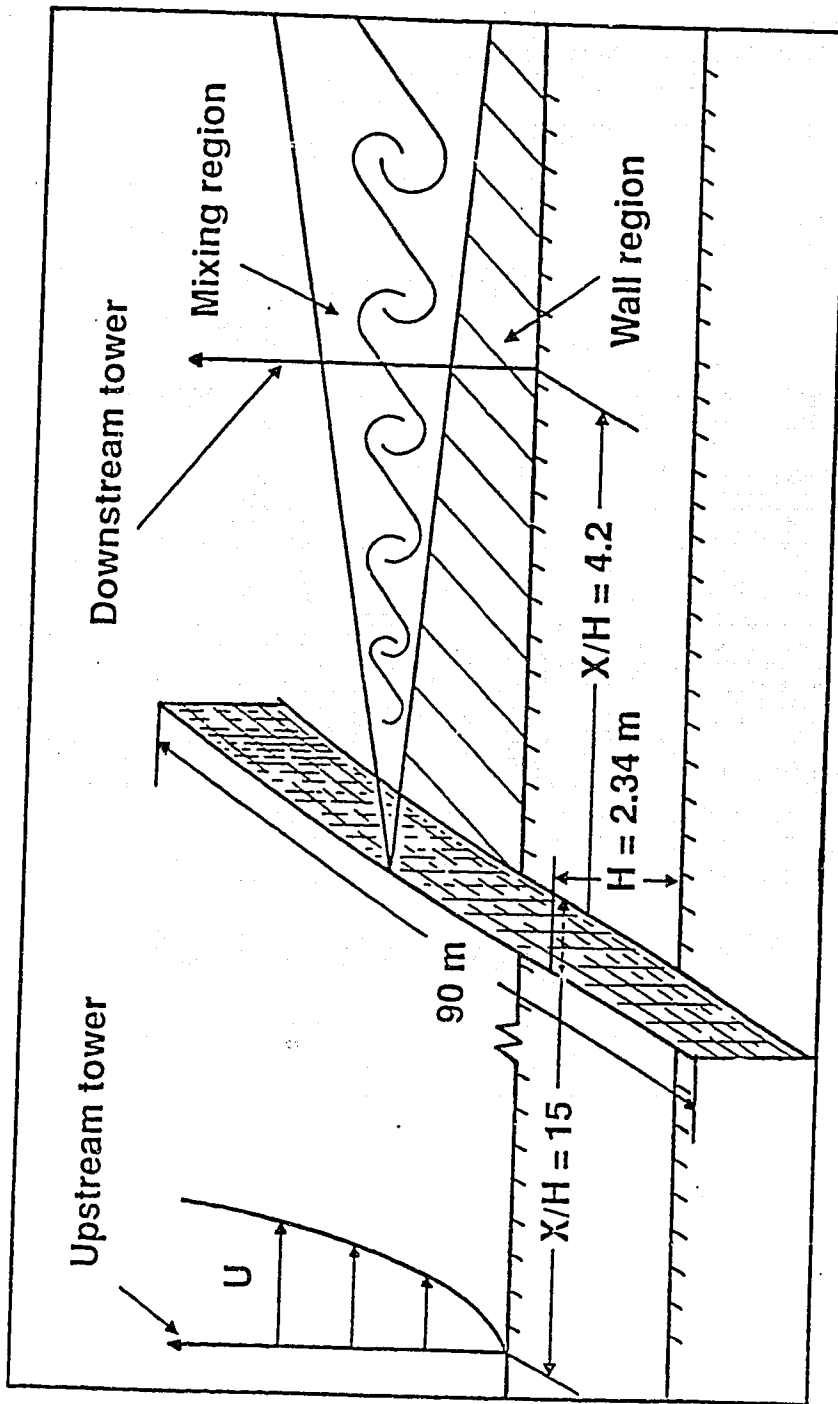
Figure 1 A schematic picture of a typical experiment set up at
Ellerslie. The wall region is bounded by ground and a
line extending from the top of the fence to the
downstream point x = 15H.
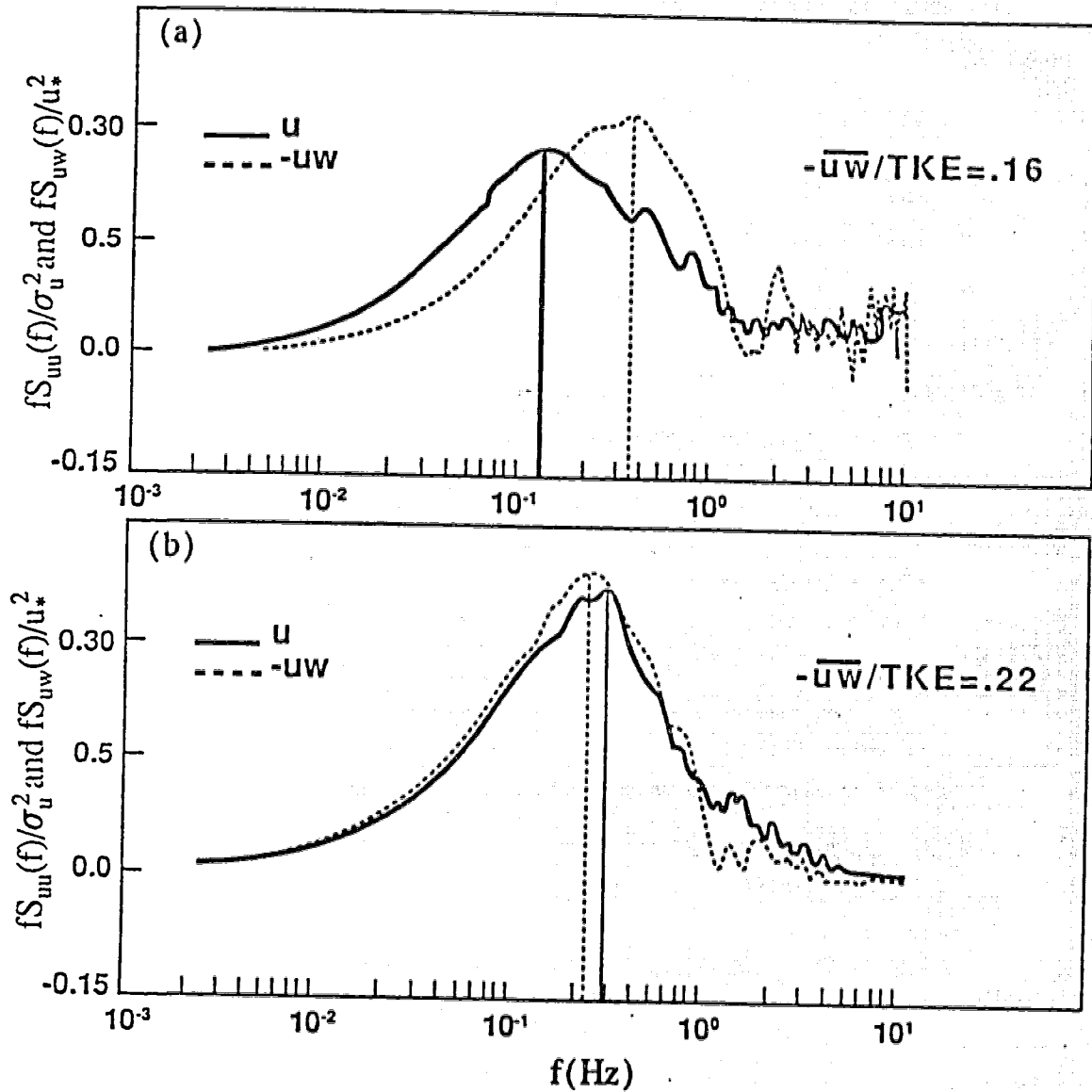
Figure 2   Alongwind velocity and Reynolds stress spectra of the windbreak flow at (a) upstream and (b) downstream mixing region, respectively. The data were measured at height (z/H = 0.71) during run 4. The mean wind speed at the upstream measurement height was 2.44 m·s⁻¹.
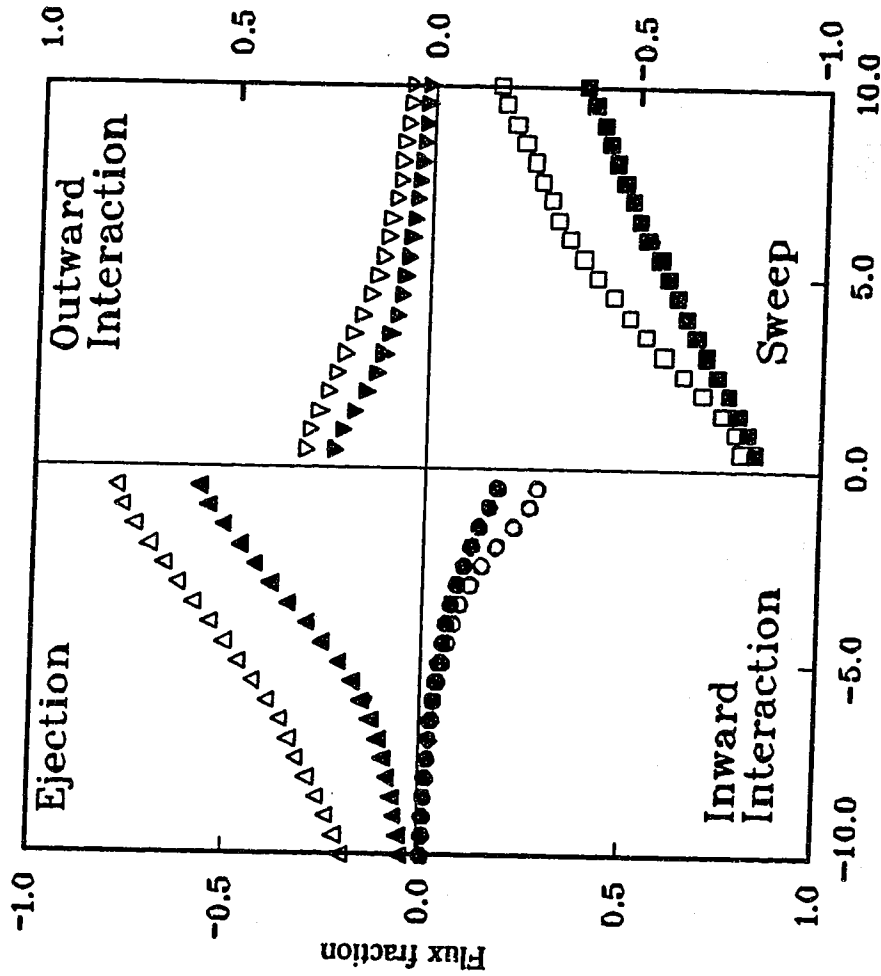
Figure 3 Conditionally sampled structure of the Reynolds stress. Stress fraction in each quadrant versus hole size H_0 in upstream and downstream mixing region (shaded symbols). At $H_0 = 0$, i.e., all scales contribute to the Reynolds stress, the stress fractions add to -1. As H_0 increases, the "small" scale turbulence has been filtered out to the hole region.
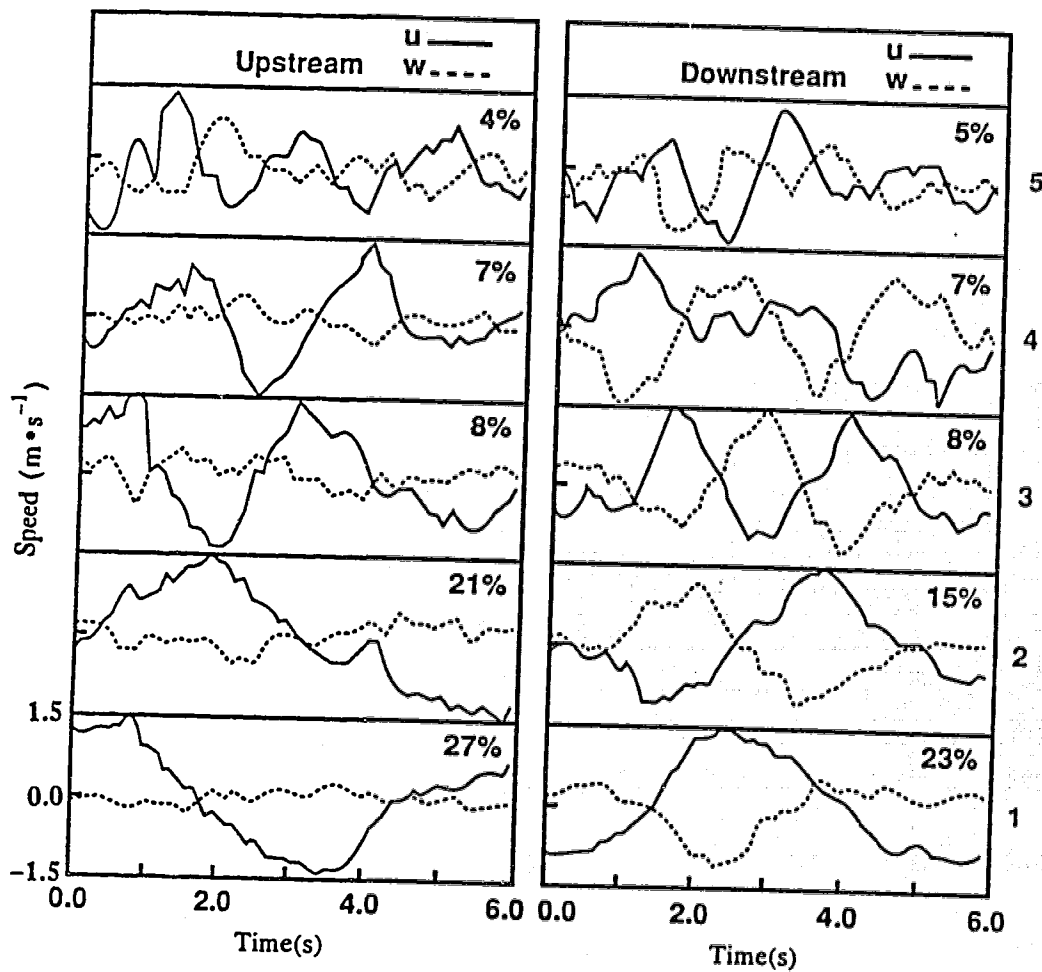
Figure 4 First five orthogonal functions obtained by P.O.D. of velocity time series observed upstream and downstream of a fence. The % are the fraction each velocity structure contributes to the total variance of the VITA-selected events. The scale for velocity applies to all five structures.
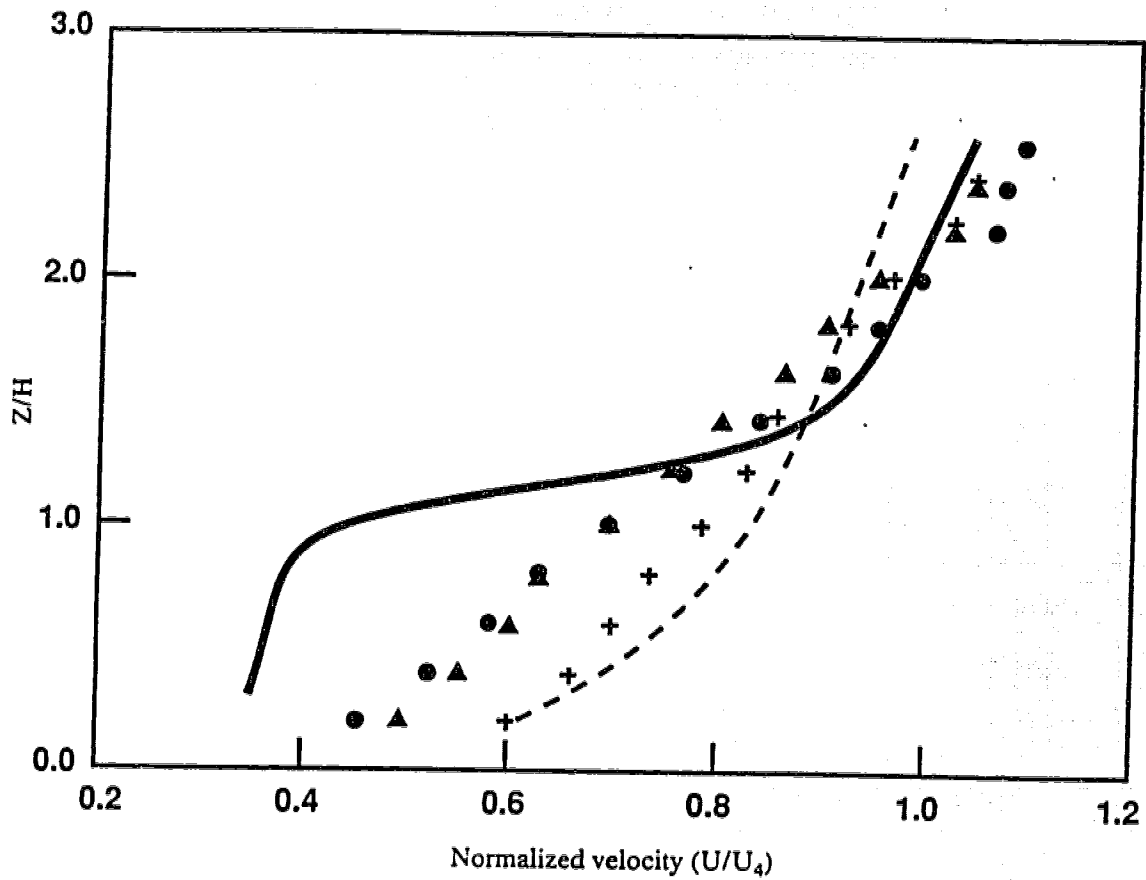
Figure 5 Mean wind profiles measured under near neutral conditions, reproduced from Bradley and Mulhearn's (1983) experiment. The wind profiles are normalized by the velocity at 4 m. The dash line denotes the upstream wind profile; ———— X/H = 0.8; ● X/H = 8.3; ▲ X/H = 15.5; + X/H = 16.1
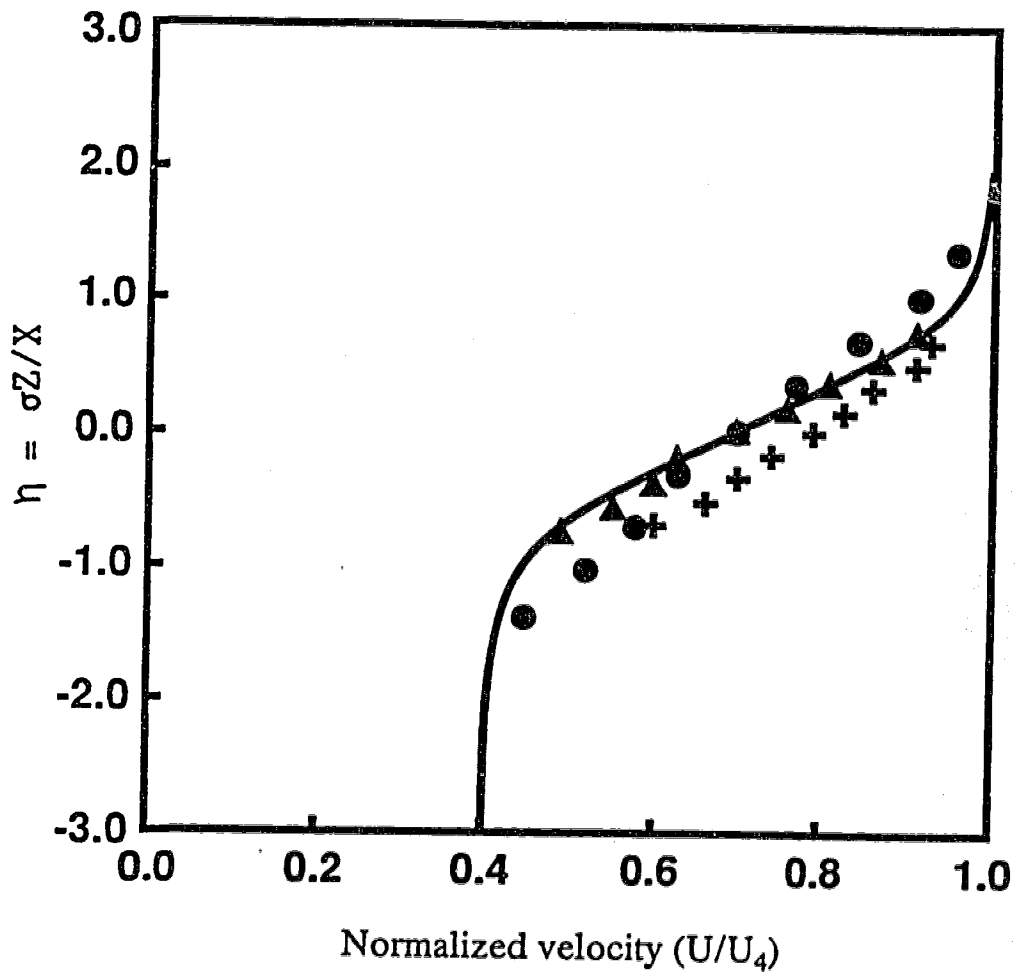
Figure 6 Theoretical and experimental mean wind profiles in the mixing
region of the windbreak, expressed in mixing layer scaling.
————— Eq. (5); Experiment (Bradley and Mulhearn, 1983): ● X/H
= 8.3; ▲ X/H = 12.5; + X/H = 16.7.
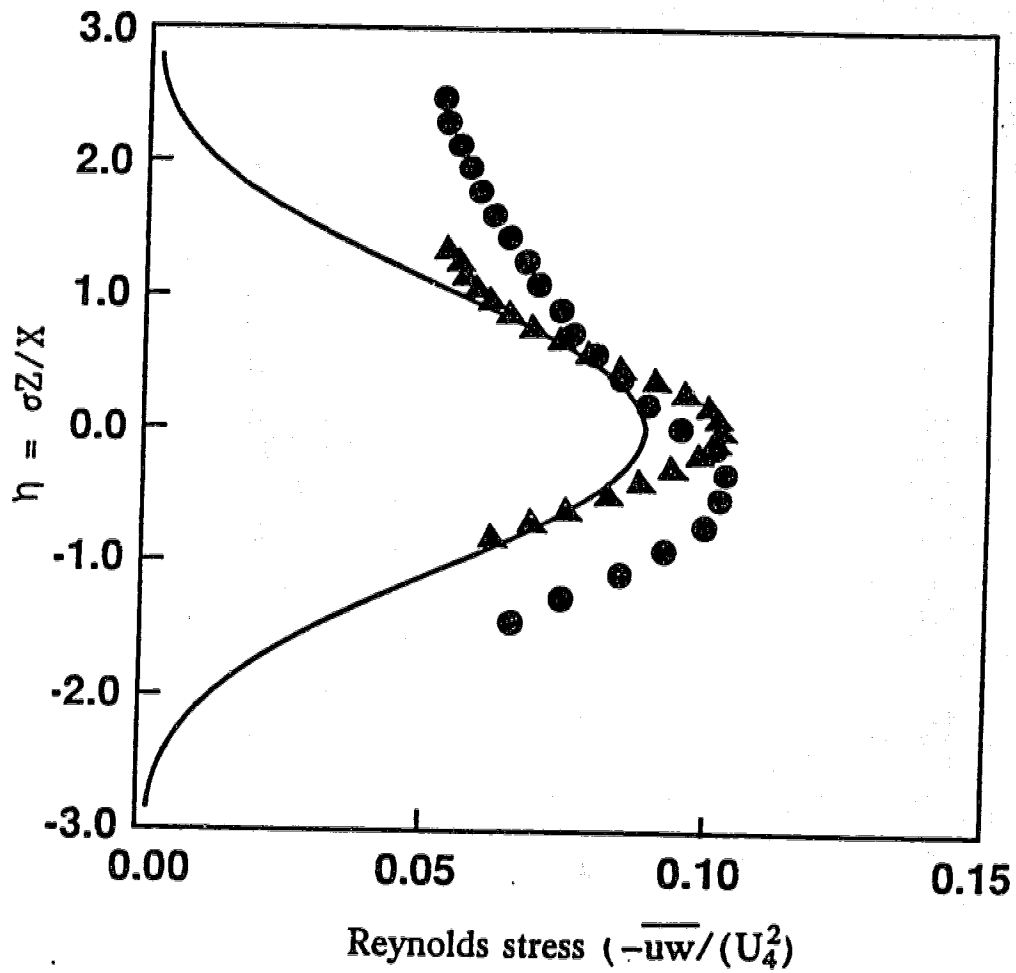
Figure 7 Theoretical and experimental Reynolds stress profiles in the mixing region of the windbreak, expressed in mixing layer scaling. ——— Eq. (6); Experiment (Bradley and Mulhearn, 1983): ● X/H = 8.3; ▲ X/H = 15.3.

References

Antonia, R.A.,: 1981,'Conditional Sampling in Turbulence Measurement', Annu. Rev. Fluid Mech. 13,131–56.

Aubry, N., P. Holmes, J.L. Lumley, and E. Stone,: 1988,'The Dynamics of Coherent Structures in the Wall Region of A Turbulent Boundary Layer', J. Fluid Mech. 192, 115–173.

Baltaxe, R.,: 1967:'Air Flow Patterns in the Lee of Model Windbreaks', Archivfur Meteorologie, Geophysik und Bioklimatologie, Series B: Allgemeine und biologische Klimatologie, Band 15, Heft 3, 26 pp.

Blackwelder, R.F., and R.E. Kaplan,: 1976,'On the Wall Structure of Turbulent Boundary Layer', J. Fluid Mech. 76, 89–112.

Bradley, L.F., and P.J. Mulhearn,: 1983,'Development of Velocity and Shear Stress Distributions in the Wake of A Porous Shelter Fence', J. Wind Eng. Ind. Aerodyn. 15, 145–156.

Bradshaw, P.,: 1966,'The Effect of Initial Conditions on the Development of a Free Shear Layer', J. Fluid Mech. 26, 225–236.

Browand, F.K., and T.R. Troutt,: 1985,'The Turbulent Mixing Layer: Geometry of Large Vortices', J. Fluid Mech. 158, 489–509.

Brown L.G., and A. Roshko,: 1974,'On the Density Effects and Large Structure in Turbulent Mixing Layer', J. Fluid Mech. 64, 775–816.

Counihan, J., J.C.R. Hunt and P.S. Jackson,: 1974,'Wakes Behind Two-Dimensional Surface Obstacles in Turbulent Boundary Layers', J. Fluid Mech. 64, 529–563.

Courant, R., and Hilbert, D.,: 1953, Mathods of Mathematical Physics, Vol 1, Interscience, 561 pp.

Dyer, A.J.,: 1974, A review of flux-profile relations, Boundary-Layer Meteorology, 1, 363–372.

Finnigan, J.J., and B.F. Bradley,: 1983,'The Turbulent Kinetic Energy Budget Behind A Porous Barrier: A Analysis in Streamline Coordinates. J. Wind Eng. Ind. Aerodyn. 15, 157–168.

Ho, C-M, and P. Huerre,: 1984,'Perturbed Free Shear Layers', Annu. Rev. Fluid Mech. 16, 365–424.

Hogstrom, Ulf,: 1990,'Analysis of Turbulence Structure in the Surface layer with A Modified Similarity Formulation for Near Neutral Conditions', J. Atmos. Sci. 47, 1949–1972.

Hunt, J.C.R., J.C. Kaimal and J.E. Gaynor: 1988, 'Eddy Structure in the Convective Boundary Layer – New Measurements and New Concepts', Q. J. R. Meteorol., Soc. 114, 827–858.

IMSL, 1989: IMSL- Fortran Subroutines for Mathematical Applications, MALB-USM-PERFCT-EN8901-1.1.

Kaimal, J.C., J.C. Wyngaard, Y. Izumi and O.R. Cote: 1972, 'Spectral characteristics of surface layer turbulence', Quart. J. Roy. Meteor. Soc. 98, 563-589.

Latigo, Ben O.,: 1979,'Large-Scale Structure Interactions in A Two-Dimensional Turbulent Mixing Layer', Ph.D Thesis, Dept. Aero-Space Engng., Univ. S. Calif., Los Angeles.

Laws, E.M. and J. L. Livesey,: 1978,'Flow Through Screens', Ann. Rev. Fluid mech. 10, 247-266.

Liu, J.T.C.,: 1989,'Coherent Structures in Transitional and Turbulent Shear Flows', Annu. Rev. Fluid Mech. 21, 283-315.

Loeve, M.,: 1955, 'Probability Theory', Van Nostrand, N.Y.

Lumley, J.L.,: 1967,'The Structure of Inhomogeneous Turbulent Flows', in A.M. Yaglom and V.I. Tatarsky, eds. Atmospheric Turbulence and Radio Wave Propagation, 166-178.

Lumley, J.L.,: 1981,'Coherent Structure in Turbulence', in R.E. Meyer, ed., Transition and Turbulence, 215-242. Academic Press, N.Y.

Mahrt, L., and Frank, H.,: 1988,'Eigen Structure of Eddy Microfronts', Tellus, 40A, 107-119.

Mulhearn, P.J., and E.F. Bradley,: 1977,'Secondary Flows in the Lee of Porous Shelterbelts', Boundary-Layer Meteorol., 12, 75-92.

Narasimha, R., and S.V. Kailas,: 1987, Energy Events in the Atmospheric Boundary Layer', in Meier, H.U. and P. Bradshaw eds., Perspectives in Turbulence Studies, Springer-Verlag, 188-222.

Ogawa,Y., and P.G. Diosey,: 1980,'Surface Roughness and Thermal Stratification Effects on the Flow Behind A Two-Dimensional Fence II: A Wind Tunnel Study and Similarity Considerations', Atmos. Environ. 14, 1309-1320.

Plate, Erich J.,: 1971,'The Aerodynamics of Shelter Belts', Agriculture Meteorol. 8, 203-222.

Raine, J.K. and D.C. Stevenson,: 1977,'Wind Protection By Model Fences in A Simulated Atmospheric Boundary Layer', J. Ind. Aerodyn. 2, 159-180.

Roshko, A.,: 1980,'The plane mixing layer, flow visualization results and three-dimensional effects" In The Role of Coherent Structures in Modelling TUrbulence and Mixing (ed. J. Jimenez). Lecture notes in Physics, Vol 136, pp. 206-217, Springer.

Schlichting, H.,: 1968, Boundary-Layer Theory. McGraw Hill.

Schols, J.L.J.,: 1984,'The Detection and Measurement of Turbulent Structures in the Atmospheric Surface Layer', Bound.-Layer Meteorol., 29, 39-58.

Seginer, Ido,: 1974,'Atmospheric-Stability Effect on Windbreak Shelter and Drag', Boundary-Layer Meteol. **8**, 383-400.

Seginer, Ido,: 1975,'Flow Around A Windbreak in Oblique Wind', Boundary-Layer Meteorol. **9**, 133-141.

Shil, T.-H.,: 1984,'Second Order Modelling of Scalar Turbulent Flow', ph.D thesis. Cornell University, Ithaca, N.Y.

Spencer, B.W. and B.G. Jones,: 1971,'Statistical Investigation of pressure and velocity fields in the turbulent two-stream mixing layer', AIAA Paper, No.71-613

Townsend, A.A.,: 1976,'The Structure of Turbulent Shear Flow', Cambridge University Press, 429 pp, 2nd ed.

Townsend, A.A.,: 1978,'Flow Patterns of Large Eddies in A Wake and in A Boundary Layer',J. Fluid Mech., **95**, 515-537.

Wilson, J.D.,: 1985,'Numerical Studies of Flow Through A Windbreak', J. Wind Eng. and Indust. aerodynmics. **21**, 119-154.

Wygnanski, I., and H.E. Fiedler,: 1970,'The Two-Dimensional Mixing Region', J. Fluid Mech. **41**, 327-361.

Yule, A.J.,: 1980,'Phase Scrambling Effects and Turbulence Data Analysis' in L.J.S. Bradbury et al Eds. Turbulent Shear Flow II. Springer-Verlaf Berlin. pp. 263-281.

CHAPTER III

EXTRACTION OF COHERENT STRUCTURES IN THE ATMOSPHERIC SURFACE LAYER

USING THE SHOT-EFFECT METHOD

1. Introduction

Most previous studies of coherent motion in the atmospheric
surface layer have used conditional sampling methods to select an
ensemble of coherent events (in the velocity or temperature signals),
and then discussed the dynamics of the averaged structures. The
quantitative properties (momentum and heat transport, translation
velocity, lifetime etc.) of the coherent structures vary among
different studies (Phong-Anant et al., 1980; Wilczak, 1984; Schols and
Wartena, 1986), reflecting not only the variation of the turbulence in
the atmospheric surface layer, but also the different methodologies
used. Conditionally averaged structures can be influenced by factors
such as the sampling criteria, and the prejudices of the researcher.
It is felt that a statistical description of coherent motion should be
more objective. In this study, the Shot-Effect method (Lumley 1981) is
described and applied to extract "statistical" coherent structures
under unstable and neutral conditions in the atmospheric surface layer.
The transport characteristics of the "statistical" coherent structures
agree qualitatively with the common perception of the transport
processes under unstable and neutral stratification.

2. Shot-Effect

Although coherent structures, such as gusts and ramps, are frequently observed in the atmospheric surface layer, the turbulence can be considered statistically stationary. In other words, we assume that the time series obtained at a fixed location in a field experiment consists of a series of coherent structures, occurring with different strengths at random times, and, in the intervening intervals, random fluctuations on smaller spatial and temporal scales, showing lesser degree of organization. For such a (stochastic) stationary time series with embedded structures, the Shot-Effect method, originally developed to study the flow of electrons from cathode to anode in a vacuum tube (Rice, 1944), can be used to extract the coherent structures. Here, a brief introduction to the concept of the Shot-Effect method, as used in turbulence studies is given (for a fuller discussion see Lumley, 1981).

A stationary stochastic time series of velocity (or temperature) with embedded structures, at a height z_m in the atmospheric surface layer, may be represented as a convolution integral

$$u_i(z_m,t) = \int_{T_1}^{T_2} f_i(z_m,t-t')\xi(t')\, dt' \quad , \tag{1}$$

where $i = (u, w, \theta)$, $f_i(z_m,t-t')$ is a deterministic function (the coherent structure) for the ith variable defined on the domain $[T_1, T_2]$, and $\xi(t')$ is a white noise function, i.e., $\overline{\xi(t)\xi(t')} = \delta(t-t')$, the overbar denoting an ensemble average. It can be shown (Rice, 1944) that the auto-covariance of $u_i(z_m,t)$ can be expressed approximately as

$$R_{ii}(z_m,\tau) = \overline{u_i(z_m,t)u_i(z_m,t+\tau)} = \int_{T_1}^{T_2} f_i(z_m,t)f_i(z_m,t+\tau)dt, \qquad (2)$$

provided the domain $[T_1, T_2]$ is large enough that

$$\frac{1}{(T_2-T_1)}\int_{T_1}^{T_2} u_i \, dt \simeq 0 \qquad .$$

After taking the Fourier Transform of Eq. (2) with respect to τ, one obtains

$$\overset{\Lambda}{R}_{ii}(z_m,\omega) = \overset{\Lambda}{f}_i(z_m,\omega)\cdot\overset{\Lambda}{f}_i{}^{*}(z_m,\omega) \quad , \qquad (3)$$

where (Λ) denotes the Fourier Transform, ω is the angular frequency and $(^{*})$ indicates a complex conjugate. The Fourier Transform of f_i can be obtained from (3) within a phase angle, $\psi(\omega)$

$$\overset{\Lambda}{f}_i(z_m,\omega) = \overset{\Lambda}{R}_{ii}{}^{1/2}(z_m,\omega) \, e^{i\psi(\omega)} \quad . \qquad (4)$$

For now, let us just consider the magnitude of $\overset{\Lambda}{f}_i$, i.e., assume $\psi(\omega) = 0$; then it follows from (4) that

$$f_i(z_m,t) = (1/2\pi)^{1/2}\int_{-\omega_0}^{\omega_0} e^{-i\omega t} \, \overset{\Lambda}{R}_{ii}{}^{1/2}(z_m,\omega) \, d\omega \, , \qquad (5)$$

where $\omega_0 = 1/\Delta t$, Δt being the sampling interval. Thus, when the phase angle is neglected, the derived structure, $f_i(z_m,t)$, is completely determined by the auto-covariance of the signal. It should be mentioned that using variance and covariance to examine spatial or temporal structure of flows has been a common statistical tool in turbulence research (Townsend, 1976). This is because persistent and dynamically important coherent structures contribute significantly to the variance and covariance.

Although the phase angle does not affect the amplitude of f_i, it may influence the geometrical structure of the coherent motion, as Lumley (1981) indicated. For example, if the coherent structure is an even function with respect to time, then $\psi(\omega) = 0$; for an odd function, $\psi(\omega) = -90°$ when $\omega > 0$ and $\psi(\omega) = 90°$ when $\omega < 0$. In general, this phase angle is not readily available, although Lumley (1981) suggested a method to recover it from higher-order statistics.

In this study, the primary concern is the transport properties of coherent structures, i.e., the momentum and heat fluxes. In that case, it is not the geometrical structure of a _single_ variable that is important, but the cross-covariances of u, w and θ that must be preserved.

In order that the coherent structure f_i obtained from Eq. (5) correctly capture the turbulent transport processes, the cross-covariances must be imposed on R_{ii}. For this purpose, let us write the experimental data as an ensemble of composite time series $F_n(z,t)$ (n = 1, ..., N), where $F_n(z,t) = [u_n(z_1,t_1), w_n(z_1,t_1), \theta_n(z_1,t_1), ...,$ $u_n(z_p,t_q), w_n(z_p,t_q), \theta_n(z_p,t_q)]$ is the nth composite time series of u, w, and θ measured at heights from z_1 to z_p, from times t_1 to t_q. Let us assume $\phi(z,t)$, a composite function (structured as F_n), resembles the dominant structure embedded in the ensemble of $F_n(z,t)$, and define $\phi(z,\omega)$ as the Fourier Transform of $\phi(z,t)$. Then using the proper orthogonal decomposition (Appendix B), $\phi(z,\omega)$ can be obtained by solving the eigenvalue problem

$$\sum_{m=0}^{M} R(z_m, z_k, \omega) \Phi(z_m, \omega) = \lambda(\omega) \Phi(z_k, \omega) \ .$$ (6)

Here $R(z_m, z_k, \omega)$ is the Fourier Transform of the cross-covariance function $R(z_m, z_k, \tau)$ calculated as

$$R(z_m, z_k, \tau) = \frac{1}{N} \sum_{n=1}^{N} F_n^T(z_m, t) F_n(z_k, t+\tau) \ , \tag{7}$$

which contains information on the signal auto-covariance (R_{ii}), velocity cross-covariance and temperature-velocity cross-covariance $(R_{ij}, i \neq j)$ with respect to space and time.

Solving Eq. (6), one obtains a set of eigenvalues $\lambda_n(\omega)$ and eigenfunctions $\phi_n(z, \omega)$ which retain all the information on the auto-covariance and cross-covariance embedded in the raw data. Consequently, the auto-covariance can be reconstructed as (Appendix B, Eq. (5B))

$$R_{ii}(z_m, \omega) = \sum_{n=1}^{N} \lambda_n(\omega) \phi_n^i(z_m, \omega) \phi_n^i(z_m, \omega) \ , \tag{8}$$

where ϕ_n^i are the eigenfunctions for the ith variable, i.e., the ith component of the $\phi_n(z, \omega)$, on which the information on both auto-variance and cross-covariance is imposed.

In the following, the Shot-Effect method will be used to extract coherent structures from measured time histories of velocity and temperature in the atmospheric surface layer, where coherent motions have been found to dominate turbulent transport (see Wilczak, 1984). By necessity, the phase angle $\psi(\omega)$ is set to zero, i.e., the coherent structure is assumed to be an even function with respect to time, which will certainly affect the geometrical structure of the coherent motion, but will not affect the cross-covariances of u, w and θ, preserved by the Proper Orthogonal Decomposition, at different heights and different times. A similar assumption in using the Shot Effect method to extract

coherent motions has been made by Moin (1984) in a fully developed turbulent channel flow and by Glauser et al. (1985) in a turbulent jet mixing layer, although the preservation of covariances by the Proper Orthogonal Decomposition was not discussed.

3. "Statistical" coherent structures extracted from tower data

The data examined here are velocity and temperature fluctuations sampled by the three-dimensional sonic anemometers from the Boulder Atmospheric Observatory (BAO) 300-m tower (see Appendix C for a brief description of the site, instrumentation and data sampling of this facility). Two sets of data were selected: the first was measured on 17 July 1986, 1100 to 1130 MST; the second on 6 August 1986, 1800 to 1830 MST (Table 1). These data were selected because the wind conditions were relatively steady during the measurements, and the data represent respectively typical unstable (i.e., light wind and strong surface heating) and neutral (i.e., strong wind and no surface heating) atmospheric surface layers, as characterized by the given value of the Monin-Obukhov length scale, L.

The data, sampled at 10 Hz, were first block-averaged over 0.8 seconds to filter out the high-frequency components. The resulting low-pass filtered half-hour records were divided evenly into 28 segments, each of 64 s duration. The measurements at the five levels (10, 22, 50, 100 and 150 m) were interpolated, using the cubic spline interpolating scheme, "CSINT" (IMSL, 1989), onto eight levels (10, 30, 50, 70, 90, 110, 130 and 150 m), with equal intervals between the levels, for the convenience of the following numerical calculation.

The velocity and temperature fluctuations, u, w and θ, in each of the segments, were used to calculate the ensemble-averaged cross-covariance function

$$R(z_m, z_k, \tau) = -\frac{1}{28} \sum_{n=1}^{28} F_n^T(z_m, t) F_n(z_k, t+\tau) \quad , \tag{9}$$

where F_n is a 1×1536 matrix, $[u_n(1, t_1), w_n(1, t_1), \theta_n(1, t_1), \ldots, u_n(8, t_{64}), w_n(8, t_{64}), \theta_n(8, t_{64})]$, and $(^T)$ denotes a transpose.

Taking the discrete Fourier Transform of $R(z_m, z_k, \tau)$ in Eq. (9) with respect to τ and then substituting into Eq. (6), the eigenvalue problem for each of the 64 frequencies was numerically solved to obtain a set of eigenvalues and eigenfunctions. Averaging over the 64 frequencies, the largest eigenfunctions were found to contribute respectively 41% and 32% of the total signal variances under unstable and neutral stratifications.

As in Moin (1984) and Glauser et al. (1985), here the coherent structure is defined as a function composed of the dominant mode for each frequency. Then the largest eigenvalue and the corresponding eigenfunction for each frequency are used to form the auto-variance in Eq. (6). Substituting Eq. (6) into Eq. (5), the coherent structure, $f_i(z_m, t)$ can be calculated for u, w and θ, respectively.

Since only the first (most energetic and organized) eigenfunction for each frequency is used to form the auto-variance in Eq. (8) and all motions with lesser degree of organization are excluded, the above method for extracting coherent motions is only meaningful in flows where coherent motions are seen experimentally to play a dominant role.

Figures 1 and 2 present the "statistical" coherent structures formed from $f_u(z_m, t)$, $f_w(z_m, t)$ and $f_\theta(z_m, t)$, and their momentum and

heat transport characteristics for an unstable and a neutral atmosphere, respectively. Comparing Figures 1 and 2, it is noted that flux patches under unstable conditions are relatively larger than those under neutral conditions. As expected, the temperature and vertical velocity are better correlated under unstable conditions than neutral conditions. This results in the effective heat transport by the coherent structures under unstable conditions (Figure 1(c)). Furthermore, there are two upward momentum transport centres in the upper layers (Figure 1(b)), as has been observed experimentally (Wilczak, 1984) under unstable conditions, whereas these are very weak under neutral conditions (Figure 2(b)).

The approximation in (2), the smoothing, and neglecting the phase angle of the Fourier Transform when implementing the Shot-Effect method, have introduced some subjectivity. However in principle, these assumptions should not affect the variance and covariance functions from which the coherent structures are extracted. Thus, the coherent structures in Figures 1 and 2 have retained objectively the cross-covariances of u, w, and θ that characterize turbulent transport at the largest scale. Since these f_α are "statistical" structures obtained by neglecting the phase angle $\psi(\omega)$, it may not be appropriate to compare them directly with a single flow visualization.

4. Conclusion

The Shot-Effect has been shown to be able to extract coherent structures from experimental data. It provides a flow "visualization" by a simple statistical analysis. The transport characteristics of the "statistical" coherent structures agree qualitatively with our perception of the transport processes under unstable and neutral stratifications.

The Shot-Effect method, like conditional sampling methods, is only a tool to extract the coherent structures from experimental data. It may be useful for an initial study of flows where not much is known about the dominant transport properties to intelligently carry out further study of the flows. To study the detailed dynamics of the coherent structures and their influence on transport in an evolving flow field, one needs to solve the governing equations. In subsequent Chapters, the governing equations, and more in depth discussions on dynamics and energetics of coherent motions in the atmospheric surface layer, will be presented.
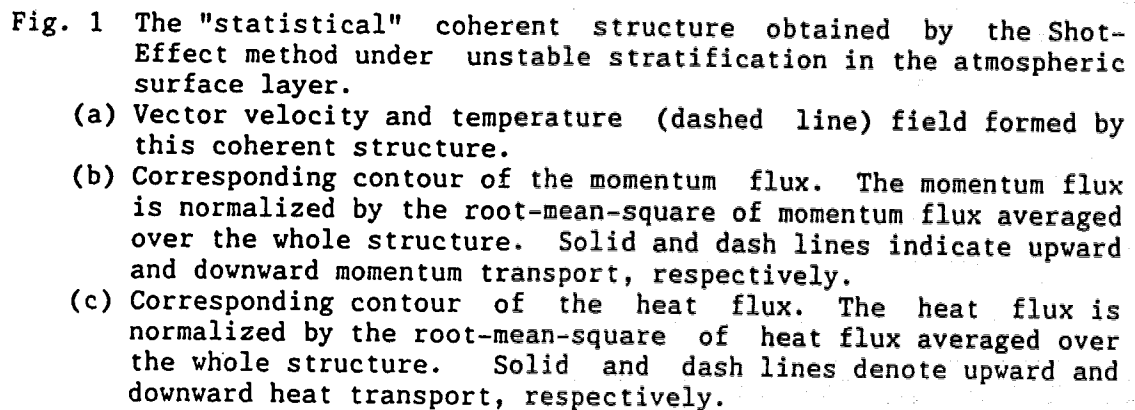
Table I

Long time average flow quantities of the typical unstable and neutral atmospheric turbulence obtained from the Boulder Atmospheric Observatory tower

Date	MST	M-O L(m)	z(m)	U(m/s)	σ_u(m/s)	σ_w(m/s)	$\overline{w\theta}$ (m℃·s)	$-\overline{uw}$ (m/s)²
17/7/86	1100–1130	-20 Unstable	10	3.19	1.40	0.55	0.28	0.16
			22	3.29	1.30	0.66	0.27	0.15
			50	3.60	1.21	0.83	0.30	0.15
			100	3.73	1.00	1.02	0.26	0.16
			150	3.85	0.94	1.04	0.21	0.17
6/8/86	1800–1830	545 Neutral	10	8.52	1.64	0.67	0.00	0.35
			22	10.64	1.67	9.67	0.00	0.28
			50	12.10	1.67	0.65	0.00	0.37
			100	13.60	1.48	0.70	0.00	0.32
			150	14.30	1.38	0.75	0.00	0.24

z   measurement height
U   mean wind speed
σ_u, σ_w standard deviations of u, and w

$-\overline{uw}$ momentum flux

$\overline{w\theta}$ heat flux

Fig. 1 The "statistical" coherent structure obtained by the Shot-
        Effect method under unstable stratification in the atmospheric
        surface layer.
  (a) Vector velocity and temperature (dashed line) field formed by
      this coherent structure.
  (b) Corresponding contour of the momentum flux. The momentum flux
      is normalized by the root-mean-square of momentum flux averaged
      over the whole structure. Solid and dash lines indicate upward
      and downward momentum transport, respectively.
  (c) Corresponding contour of the heat flux. The heat flux is
      normalized by the root-mean-square of heat flux averaged over
      the whole structure. Solid and dash lines denote upward and
      downward heat transport, respectively.

(a)

(b) Momentum Flux

(c) Heat flux

Time (sec)
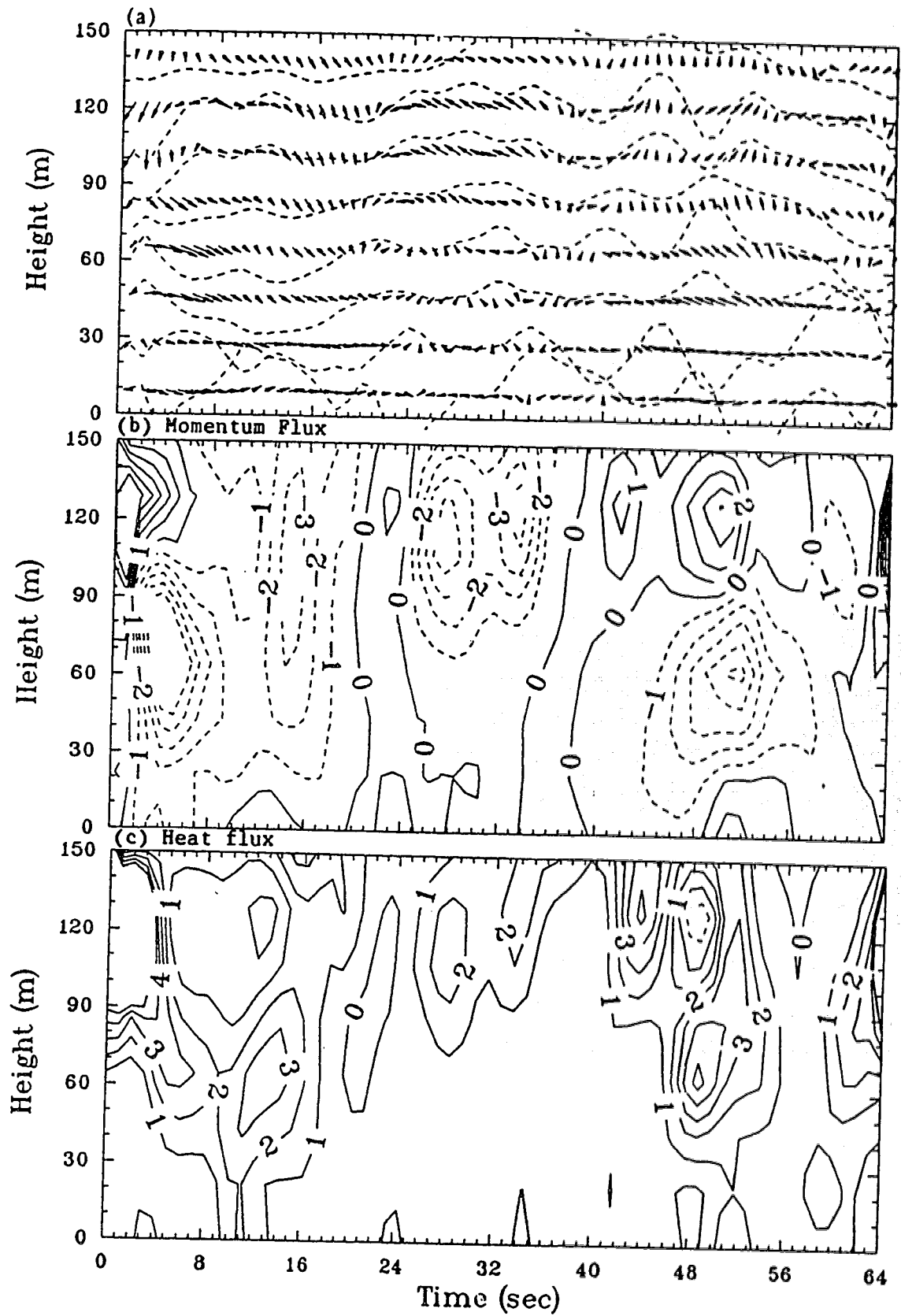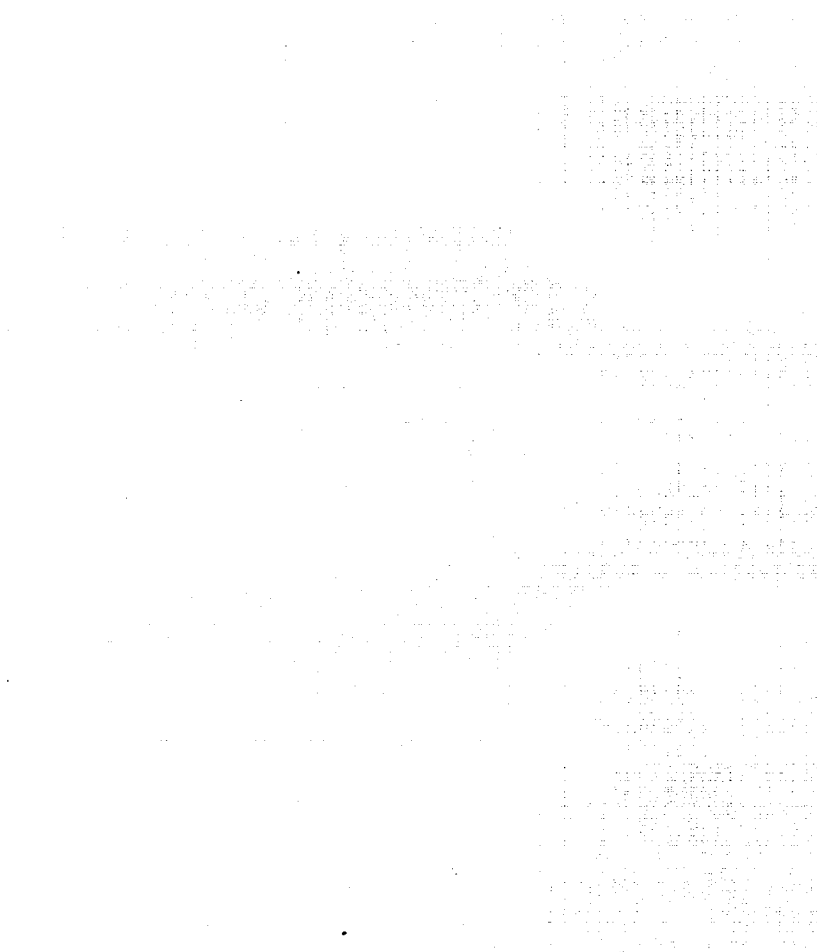
Fig. 2 As in Fig. 1 but for neutral stratification. Note that
        although the heat flux under neutral conditions is very small,
        the contours are plotted to compare their pattern with those
        under unstable conditions.

(a)

(b) Momentum Flux

(c) Heat flux
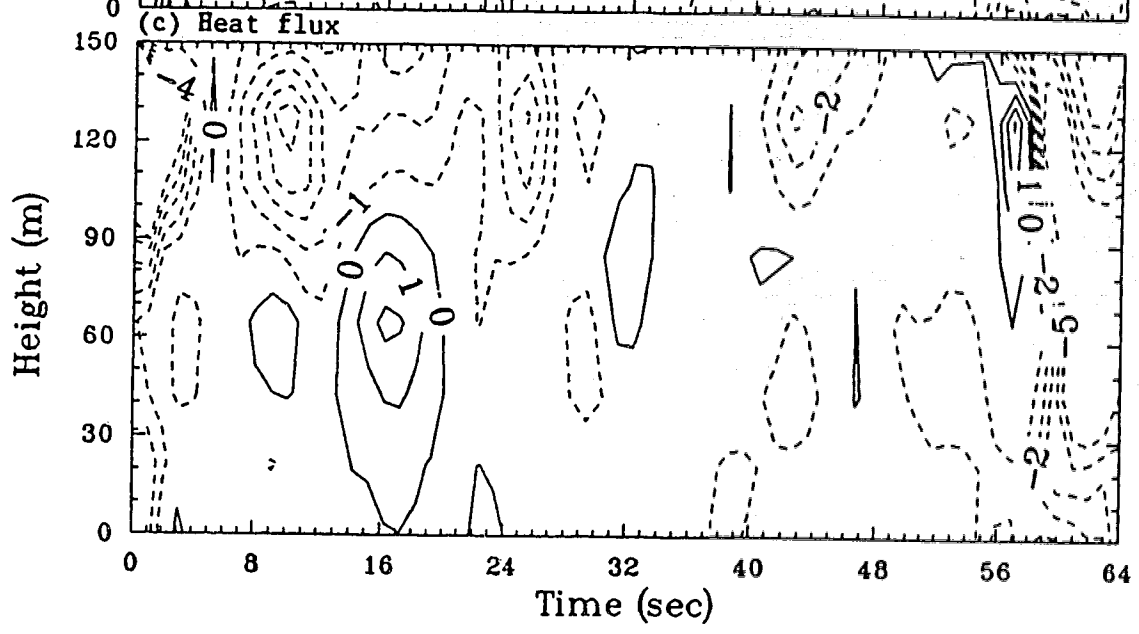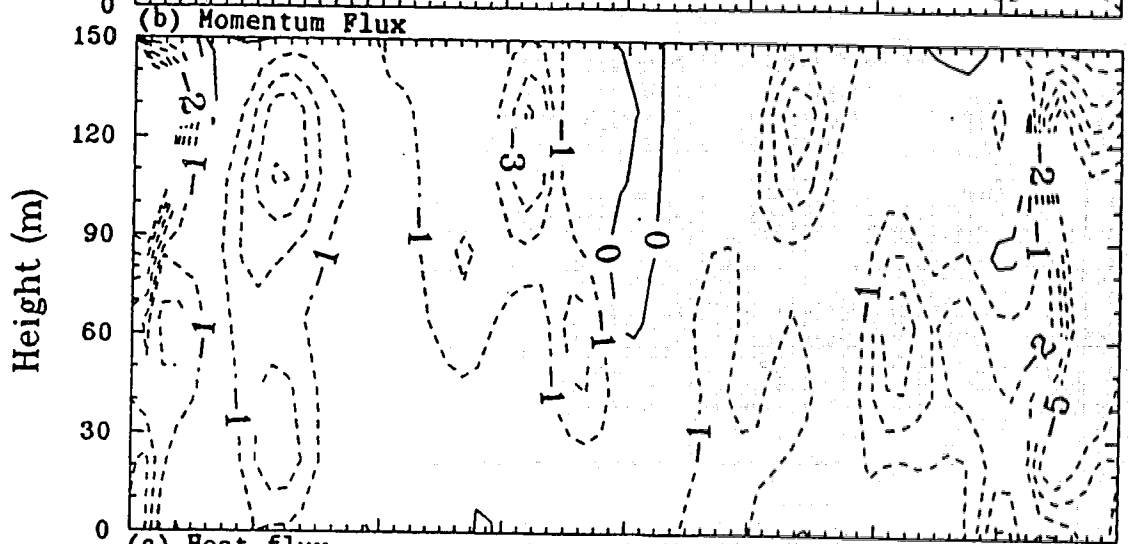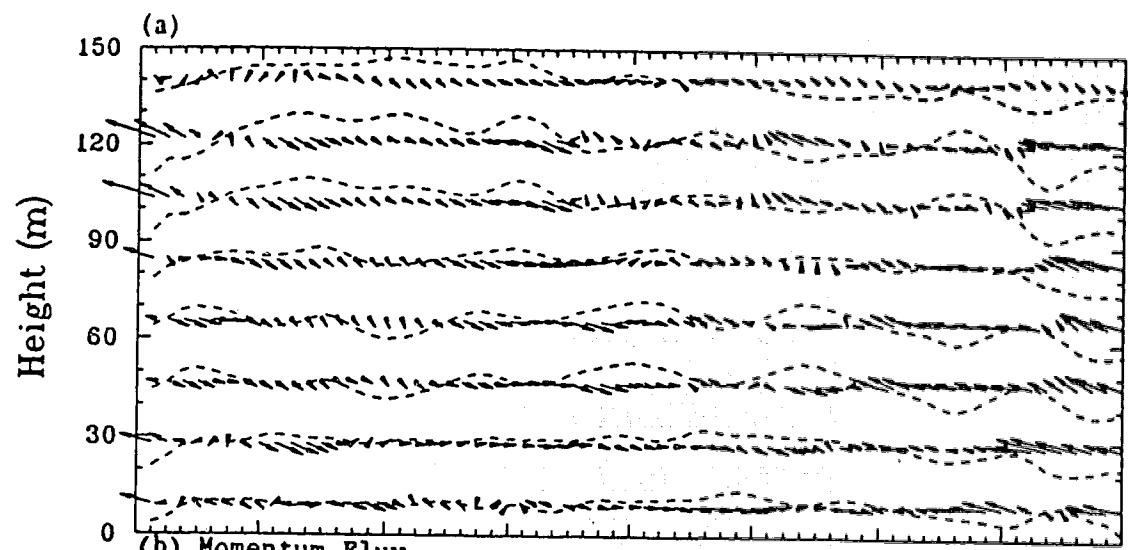
References

Glauser, M.N., Stewart, J. Leib, and William, K. G.: 1985, 'Coherent Structures in the Axisymmetric Turbulent Jet Mixing Layer', Turbulent Shear Flows Vol. 5, 134-145, Springer-Verlag.

IMSL, 1989: IMSL- Fortran Subroutines for Mathematical Applications, MALB-USM-PERFCT-EN8901-1.1.

Kaimal, J.C. and Businger, J.A.: 1970, 'Case Studies of a Convective Plume and a Dust Devil', J. Appl. Meteorol. 9, 612-620.

Kaimal, J.C. and Gaynor, J.E.: 1983, 'The Boulder Atmospheric Observatory', J. Appl. Meteorol. 22, 863-880.

Lumley, J.L.: 1967, 'The Structure of Inhomogeneous Turbulent Flows', Atmospheric Turbulence and Radio Wave Propagation, A.M. Yaglom and V.I. Tatarski, eds., Moscow, Nauka, 166-178.

Lumley, J.L.: 1981, 'Coherent Structures in Turbulence', Transition and Turbulence, R.E. Meyer, ed., Academic Press, N.Y., 215-241.

Moin, P.: 1984, 'Probing Turbulence Via Large Eddy Simulation', AIAA paper No. 84-0174.

Phong-Anant, D, Antonia, R.A., Chambers, A.J., and Rajagopalan, S.: 1980, 'Features of the Organized Motion in the Atmospheric Surface Layer', J. Geophys. Res. 85, 424-432.

Rice, S.O.: 1944, 'Mathematical Analysis of Random Noise', Bell System Tech. J. 23, 282-332.

Schols, J.L. and Wartena, L.: 1986, 'A Dynamical Description of Turbulent Structures in the Near Neutral Atmospheric Surface Layer: the Role of Static Pressure Fluctuations', Boundary-Layer Meteorol. 34, 1-15.

Townsend, A.A.: 1976, The structure of Turbulent Shear Flow. Cambridge University Press, 2nd edition.

Wilczak, J.W.: 1984, 'Large-Scale Eddies in the Unstable Stratified Atmospheric Surface Layer. Part I: Velocity and Temperature Structure', J. Atmos. Sci. 41, 3537-3550.

CHAPTER IV

A LOW-ORDER STUDY OF LARGE-SCALE COHERENT STRUCTURES

IN THE CONVECTIVE ATMOSPHERIC SURFACE LAYER: MODEL DEVELOPMENT

1. Introduction

A typical convective plume or coherent structure (hereafter, CS) in the atmospheric surface layer is associated with ramps in the scalar (temperature, humidity, tracer contaminant) signals, and corresponds to gust-ejection cycles in the velocity fluctuations (Wilczak 1984). These CS's are three-dimensional, but distinctly elongated in the alongwind direction, except under very unstable conditions when they are found to decrease in alongwind extent, and to increase in crosswind extent (Wilczak and Tillman 1980; Williams and Hacker 1992). The vertical extent of the CS's varies with atmospheric stability, and from structure to structure. Some CS's can extend through the whole atmospheric boundary layer. Observations show that the lifetimes of the CS's are at least as long as the time required for them to propagate for a distance several times their alongwind length (Wilczak and Tillman 1980). The time fraction when the coherent motions are observed was found to be about 42% in the unstable atmosphere (Antonia et al. 1983).

Because of their frequent occurrence and persistent nature, the CS's have been found to be largely responsible for the momentum and heat transport, and to contribute significantly to the budget of turbulent kinetic energy and some third-order turbulent statistics (e.g., $\overline{w^3}$) observed in the convective atmospheric surface layer

(Wilczak 1984; Hunt et al. 1988). The occurrence of the CS's has not been explicitly taken into account in the usual ensemble-average turbulence models, and is believed to be one of the causes of the necessary adjustments of model constants (especially those related to modelling of pressure covariances) in order to bring into alignment predictions and observations in the convective atmosphere (Lewellen and Teske 1973; Wyngaard 1980).

In view of their decisive influence on turbulent transport in the convective atmosphere, it is natural to speculate that, among other factors (low-frequency changes in wind speeds and directions, etc.), the CS's and their variation (in number and nature) with atmospheric stratification may be partially responsible for the variability of the mean concentration fields observed under apparently identical "mean" meteorological conditions (e.g., mixed-layer depth, surface heating and mean wind profile etc.) in air quality experiments (Wyngaard 1988). In addition, CS's will certainly cause some short-term random fluctuations in pollutant concentrations, which can be as important as the average concentration. Therefore, an air-quality model should consider this intermittent nature, as well as the average flow properties (Wyngaard 1988).

Most previous work on turbulence structures in the atmospheric surface layer has used conditional sampling or other statistical methods (Young 1988; Mahrt 1991; Williams and Hacker 1992; Turner and Leclerc 1992) to extract CS's. The transport properties and dynamics of the CS's were then discussed with reference to the "averaged" or "statistical" structures. A problem with these studies is that the subjective selection of the coherent events, and the averaging and

smoothing procedures, when applied to an unsteady atmospheric turbulence, may mask the structure of the coherent motions. In addition, time-dependent behaviour of the CS's has not been discussed in these studies.

There have been attempts to model the CS's in the convective atmospheric surface layer. Telford (1970) developed a model to predict the bulk properties (radius, upward velocity, turbulence intensity, etc.) of an isolated plume in a convective field, assuming that it has a statistically uniform interior and a sharp boundary. Although interesting, and comparing quite favourably with field observations, Telford's model was derived empirically (i.e., the Navier-Stokes equations were not used), and neglected the environmental wind shear which, as will be shown in Chapter V, is important for the evolution of a plume.

More recently, Large Eddy Simulation, in which large-scale structures are explicitly calculated and the unresolved (or subgrid) scales are modelled, has become an alternative tool for studying CS's in atmospheric turbulence (Schmidt and Schumann 1989; Schumann and Moeng 1991). In order to study CS's, Schmidt and Schumann sorted out the CS's in the flow fields by conditional sampling, from the huge amount of numerically generated data. Using the results from large eddy simulation, Schumann and Moeng were able to study the budgets of momentum and turbulent kinetic energy within large-scale mixed layer thermals in more detail than could be provided by experimental study (Young 1988). These studies have also revealed some detailed three-dimensional flow structures of the mixed layer thermals, e.g., the spoke pattern found in Schmidt and Schumann's study, that would have

been difficult or impossible to obtain experimentally. Notwithstanding these studies, it is felt that coherent flow dynamics in the atmospheric surface layer are to some extent unknown. Besides, Large Eddy Simulation is still very expensive. Thus, seeking a way to study CS's with clear physics and without excessive computation is desirable.

The concept of Large Eddy Simulation implies that some of the degrees of freedom (i.e., those related to small-scale fluctuations) in turbulent flows can be removed, by modelling the small-scale turbulence. In other words, considering the correlation between small and large-scale turbulence (e.g., using eddy viscosity closure) greatly reduces overall computational effort. The rationale for such a simplification in calculating turbulent flows may be supported by recent applications of the dynamical systems theory to turbulence (Sreenivasan 1985; Newell et al. 1988). These studies have shown that the transport properties of turbulent flows, especially those that are dominated by CS's, may be governed by relatively low-dimensional strange attractors in phase space (to be introduced in Section 2). To model a strongly organized flow, it has been suggested that a natural decomposition is to divide the flow into CS's represented deterministically by the dominant orbits in phase space, and superposed stochastic fluctuations. By definition, within a CS the flow field is temporally and spatially correlated, so it is reasonable to think that further simplification to computing large-scale turbulence can be made when the correlations within a CS are considered.

Lorenz (1972), decomposed the Navier-stokes equations in two dimensions with an infinite system of time-dependent ordinary differential equations. By sorting the equations into sets of

statistically similar behaviours, and retaining only a few of them within each set, a low-order model (28 ordinary differential equations) was constructed. When compared with a more-complete numerical simulation, the solutions of the low-order model exhibit many of the important properties of two-dimensional turbulence, although not all of them. Recently, Aubry et al. (1988) studied theoretically a low-order system of ten ordinary differential equations for the near-wall boundary layer flow, from the dynamical systems point of view. They showed that the repetitive intermittency found by solving the low-order equations in phase space corresponds to the burst phenomenon commonly observed in the wall region of the turbulent boundary layer. This indicates that the basic dynamics of the burst phenomenon can be modelled adequately using only a few low-order modes.

In view of the abundant experimental evidence of CS's and their simple and repeatable patterns in the convective atmospheric surface layer, in this study, the possibility of describing deterministically the CS's was explored through experimental data analysis and theoretical reasoning. A low-order model (15 ordinary differential equations) based on empirical basis functions and the Navier-Stokes equations will be derived. This new framework can describe not only the coherent dynamics of the "averaged" or "statistical" CS's, but also their (short-term) time-dependent behaviour, not emphasised in previous studies.

2. A Dynamical Systems View of Turbulence in the Atmospheric Surface Layer

The atmospheric surface layer occupies roughly the lowest 10% of the atmospheric boundary layer, where the mean turbulent vertical fluxes of momentum, heat and moisture can be regarded as approximately height-independent. It is characterized by strong vertical wind shear, and turbulent motions (including intermittent CS's) that are affected by the proximity of the ground. In this section, experimental data will be analysed, taking the dynamical systems points of view, to examine the possibility of a low-order study of CS's in a stationary, horizontally-uniform convective atmospheric surface layer, where both vertical wind shear and buoyancy force operate as turbulence energy sources.

The atmospheric surface layer can be considered a dynamical system, since its evolution from a known initial state can be described by a set of rules, the Navier-Stokes equations. Theoretically, partial differential equations such as the Navier-Stokes equations can be transformed into a set of N truncated, coupled, ordinary differential equations by expressing the spatial variability with a set of N orthogonal functions, as commonly practiced in spectral fluid dynamics (Qanuto et al. 1988). For example, if $A_i(t)$ are expansion coefficients, then a flow variable f (velocity or temperature) can be represented as

$$f(x,t) = \sum_{i=1}^{N} A_i(t)\phi_i{}^f(x) , \tag{1}$$

where $\phi_i{}^f$ are orthogonal basis functions for the variable f. Substituting Eq. (1) into the Navier-Stokes equations and using the

Galerkin projection (to be introduced in Section 3), one obtains a set of N coupled, time-dependent ordinary differential equations:

$$\dot{A}_i(t) = F_i(A_1, A_2, \cdots, A_N), \quad i = 1, 2, \cdots, N , \tag{2}$$

where F_i are determined by the orthogonal functions and their spatial derivatives. The evolution of the flow can then be described by the time history of the N expansion coefficients $A_i(t)$, which serve as the generalized coordinates of the flow in a phase space wherein lie the solutions of (2). Each set of A_i (i = 1, 2, 3, ..., N) at time t forms a point in the phase space, and defines a flow realization at that instant in physical space. N is the number of the phase variables needed to describe the flow, and is also termed the number of degrees of freedom (Monin 1978). Depending on how complex the underlying system is, the number of degrees of freedom may vary from "a few" for a laminar flow to infinity for a truly random process. It is important to note that the number of degrees of freedom also depends on the choice of the orthogonal functions, i.e., an optimal set of orthogonal functions will minimize the required number of degrees of freedom.

In the N-dimensional phase space, a system trajectory, i.e., evolution of the physical flow, can be represented as a vector:

$$A(t) = (A_1(t), A_2(t), ..., A_N(t)) . \tag{3}$$

Portraits of the time evolution of A(t) may show a distinct pattern. A time-independent physical flow forms an unmoving point, while a periodic physical flow forms a close contour such as a circle or torus. These points and circles or tori are called "attractors", and are characterized by their integral number of dimensions in phase space. Traditionally turbulent flows, owing to their wide spectrum of scales of motion, have been described in phase space by a torus, or a quasi-

periodic attractor with very high dimension (Landau 1944). This view was challenged by Ruelle and Takens (1971), who proposed a model in which turbulent motion could be reached after a small number of bifurcations (the exchange from one to another stationary solution in a system, when one of the external parameters is varied). The attractor of this turbulence model has a small, but fractal (real number) dimension, and has been termed "strange attractor". The strange attractor is characterized by the property of extreme sensitivity to the initial condition, i.e., any two initially-close trajectories on the attractor eventually diverge from each other. Because of the sensitivity to the initial condition property of strange attractors, variables in a system where strange attractors play an important role are neither periodic nor quasi-periodic, and appear random even though they are actually deterministic. This implies that, in situations where the random experimental signals are caused mainly by an underlying low-dimensional attractor, a low-order description (i.e., small numbers of ordinary differential equations) of the system may be possible.

The turbulent flow in the atmospheric surface layer is a dissipative dynamical system, i.e., turbulent kinetic energy is continually being generated and damped. For such a system, in which turbulent kinetic energy generation and dissipation mechanisms compete for dominance, and the signals exhibit chaotic behaviour, there is often a strange attractor in the phase space (Berge et al. 1984). The simple and repeatable feature of CS's in the convective atmospheric surface layer (Schols 1984; Wilczak 1984) may indicate that the turbulent flow, and especially the CS's, are characterized by a certain

degree of order. Although there are variations (number and nature) of CS's among different studies, this may be understood as the temporal variation of the expansion coefficients in Eq. (2). It is thus suggested that a few orthogonal functions and relatively simple trajectories in phase space, i.e, a few ordinary differential equations, may be all that are needed to describe the dynamics of the CS's in the convective atmospheric surface layer. This conjecture may be confirmed by determining the correlation dimension of the phase space visited by this dynamical system. For this purpose, we need to define a phase space. A suitable phase space can be constructed from experimental data by the time-delayed method (Packard et al. 1980; Takens 1981).

a. Construction of the phase space

Equation (2) shows that the evolution of a physical flow can be described by a set of N ordinary differential equations. It can easily be shown that Eq. (2) can be reduced to a single ordinary differential equation for, say, A_1 if all other variables are eliminated by differentiation

$$A_1^{(N)}(t) = G\ (A_1(t),\ A_1^1(t),\ \dots\ ,A_1^{(N-1)}(t))\ ,\tag{4}$$

where G is a highly nonlinear (Nth order) function of A_1. Eq. (4) indicates that the system can be described by N phase variables $(A_1(t), A_1^1(t), \dots, A_1^{(N-1)}(t))$ involving a single variable A_1, without any loss of information. Physically this means that, provided it is sampled a sufficient number of times, any single variable will represent the characteristics of the underlying system.

In practice, experimental signals are prone to being contaminated by extraneous noise (e.g., noise arising in the electronics of the sensing or recording device) and derivatives are especially susceptible. Ruelle (1981) suggested that phase coordinates formed by a single phase variable $A(t)$ and its successive shifts, by a delay constant τ, $A(t + n\tau)$, should also describe the underlying system, provided n is big enough. Takens (1981) showed that if an underlying attractor has dimension N, then $(2N + 1)$ independent phase variables will faithfully represent the attractor.

The data used for phase construction in this study were turbulent fluctuations of the three velocity components (u, v, w) and the temperature (θ) measured at the 300 m tower of the Boulder Atmospheric Observatory (BAO), located near Boulder, Colorado (See Appendix C for a brief description of the site, instrumentation and data sampling of this facility). A total of 60-min of data (four signals digitized at 10 Hz to yield 36000 samples for each signal) were selected from the data available between 10:40 am to 11:40 am on July 25, 1986. The mean flow properties listed in Table 1 indicate that both wind shear and surface heating are important for the flow selected.

In constructing phase variables from experimental data, it has been suggested (Guckenheimer 1986) that, instead of using one experimental variable measured at a single point, one should use many time series measured at different locations in space, to include information on the spatial variability of the flow. Thus all the three velocity components and temperature fluctuations measured at the first five levels (10, 22, 50, 100, 150m), which are considered to be within the atmospheric surface layer, were used.

The data were first arithmetically averaged every 5 seconds to remove the high frequency components not of interest in this study, and then normalized by their respective standard deviations calculated over the 60-min period. From the normalized data $u_m(t_i)$, $v_m(t_i)$, $w_m(t_i)$ and $\theta_m(t_i)$ ($m = 1,...5$), the vector phase variables are constructed

$$X(t_i,M) = \{w_1^{(M)}(t_i), .., w_5^{(M)}(t_i), \theta_1^{(M)}(t_i), .., \theta_5^{(M)}(t_i), \\ u_1^{(M)}(t_i), .., u_5^{(M)}(t_i), v_1^{(M)}(t_i), .., v_5^{(M)}(t_i)\} \quad (5)$$

where M is the embedding dimension of the phase space, which varies from 5 (only vertical velocities are used) to 20 (all three velocities and temperatures are used). From Eq. (5) we can see that as the time index i increases, the trajectories of the vector phase variables will form a "cloud" of points in a phase space of dimension M.

In principle, the time interval, $\Delta t = t_{i+1}-t_i$, should be chosen such that the resulting M-dimensional phase variables will be independent. It is suggested that a time interval of about one fourth the period of the characteristic oscillation of the system works best (Guckenheimer 1986). Here, Δt is chosen as 5 s, which is of the same order of magnitude as the height-averaged Lagrangian time scale of the velocity fluctuations in the atmospheric surface layer (Hanna 1981). The relatively large time interval Δt used here implies that the phase-space analysis pertains to large-scale flow.

b. Determination of the correlation dimension

If a dynamical system is determined by a relatively low-dimensional attractor, we expect that there exist spatial correlations between the points in phase space. The correlation dimension is a measure of long-time spatial correlation between points in phase space, which can be obtained from the characteristic of the "cloud" formed by

the M-dimensional system trajectories. The correlation dimension of a dynamical system is obtained by computing the correlation integral

$$C(r) = \lim_{N_p \to \infty} \frac{1}{N_p^2} \sum_{i,j=1}^{N_p} H(r - |X(t_i,M) - X(t_j,M)|) \qquad (6)$$

Here $H(x)$ is the Heaviside function, $H(x) = 1$ for $x > 0$, $H(x) = 0$ for $x < 0$. The $X(t_i,M)$ are the M-dimensional phase space variables for this system, and N_p is the total number of $X(t_i,M)$ formed, which is the total number of system observations. $C(r)$ counts the average number of data points in phase space that lie within a hypersphere of radius r. If the underlying system has a low-dimensional attractor with a correlation dimension d, then it has been shown that $C(r) \propto r^d$ for a certain range of r, and this relation does not change with increasing embedding dimension M (Grassberger and Procaccia 1983). This can be simply understood as follows. If one puts points at random onto a d-dimensional object one expects the number of points in any hypersphere of radius r to behave as r^d. In practice, for very small r, the number of pairs of $X(t_i,M)$, $X(t_j,M)$ whose distance is less than r becomes small, and the statistic calculated from Eq. (6) is poor; on the other hand, at very large r, all pairs of $X(t_i, M)$, $X(t_j,M)$ lie within the span of the attractor, resulting in $C(r) = 1$. Thus, the relation $C(r) \propto r^d$ only holds for a certain range of small r. Note that for a completely random system, i.e., no attractor in phase space, d increases with increasing embedding dimension M; no saturated d can be obtained (Berge et al. 1984).

An estimate of the correlation dimension furnishes a lower bound for the dimension of the phase space needed to describe the system in

question, i.e., a lower bound on the number of ordinary differential equations that should be components of a model predicting the evolution of the system. Using 720 values of the vector $X(t_i, M)$, constructed with Eq. (5) from the 60-min data, the correlation $C(r)$ was calculated as a function of M and r. When the correlation $C(r)$ is plotted against r (Fig. 1), it is found that the slope becomes saturated roughly at $d = 5.7$ when M approaches 10 (i.e., only w and θ are used). Thus, this dimension estimate implies that the system can have as few as 6 (i.e., $N = 6$, the nearest integer greater than d) degrees of freedom and, in principle, the flow evolution may be confined to a 13 ($2 \times N + 1 = 13$) (Takens 1981) dimensional phase space.

It must be mentioned that, in general, this technique for implementing the correlation dimension estimate requires a large number of data points, so that a large number of $X(t_i, M)$ can be formed to cover detailed structure of the attractor. However, Lorenz (1991) demonstrated that the number of data points used to estimate the correlation dimension need not be very large, if the most relevant variables of the system are selected. The low-pass filtered velocity and temperature fluctuations chosen here are the essential variables to describe the large-scale turbulent motions in the atmospheric surface layer. In fact, when the same technique was applied to analyse another set of 60 min Boulder data observed under the convective condition (with different wind shear and surface heating), a similar correlation dimension (6.2) was obtained. Hence, the uncertainty in the dimension estimate using the rather small data set in this study may not be as large as one might think.

Since there is no theory that says given a finite correlation dimension, the associated system has a strange attractor (Tsonis 1993), the low correlation dimension obtained above only indicates the lower bound of the actual number of degrees of freedom of the system. However, the analysis above does provide some hope of a useful low-order description of the large-scale flow.

3. Derivation of A Low-Order Dynamic Model for CS's in the Atmospheric Surface Layer

The dimension estimate in Section 2 provides a lower bound for the number of ordinary differential equations necessary to model the dynamics of CS's in the convective atmospheric surface layer. However, the theory says nothing about construction of the model. The fact that a turbulent flow can be represented by a small number of degrees of freedom in phase space means that, mathematically, the flow field in physical space can be expanded on a small set of appropriate orthogonal functions (i.e., basis functions). Since the turbulent flow is governed by the Navier-Stokes equations, to obtain an M-dimensional set of dynamic equations, one may simply project the Navier-Stokes equations along a set of M orthogonal functions.

A common choice is to decompose the flow variables as Fourier series, leading to what is called spectral fluid dynamics. However, in the Fourier series representation, the wave numbers are evenly distributed over a given domain, so small-scale motions (i.e., large wave number) are represented by many Fourier modes, while large-scale motions have few modes. That is, given a spatial resolution within a

domain, the Fourier series representation is relatively ineffective in representing large-scale motions (Tennekes 1978). Furthermore, since large-scale CS's are sensitive to the geometry of the boundary, i.e., different flows have different CS's, it is inappropriate to use one set of orthogonal functions to characterize flow structures in general. Therefore, flow-dependent orthogonal functions should be used. In this study, such optimal orthogonal functions will be extracted from experimental data by the "Proper Orthogonal Decomposition" method proposed by Lumley (1967,1981). Readers are referred to Appendix B for a brief introduction to this method.

a. <u>Proper Orthogonal Decomposition of a turbulent flow</u>

It has been shown in Chapter II (Section 2.4) that when requiring resemblance to the embedded structure in an ensemble of flow realizations, $f_t(x)$ (t = 1, 2, 3, ..., N), defined on a domain $[X_1, X_2]$, the orthogonal functions ϕ can be obtained by solving the following eigenvalue problem

$$\sum_{p=0}^{P} R(x_p, x_k)\phi(x_p) = \lambda\phi(x_k) \quad , \tag{7}$$

where the sum is over the domain divided into P equal intervals with $x_0 = X_1$, $x_1 = X_1 + \Delta x$, ..., $x_p = X_2$, λ is the eigenvalue, and

$$R(x_p, x_k) = \frac{1}{N}\sum_{t=1}^{N} f_t(x_p)\,f_t(x_k)$$

is the two-point covariance function which is a (P+1)x(P+1) matrix formed from the N flow realizations. By solving this eigenvalue problem, one finds a set of N eigenvalues λ_m and eigenfunctions ϕ_m

(orthogonal functions). A single flow realization at an instant t can then be decomposed by the orthogonal functions

$$f_t(x) = \sum_{m=1}^{N} \alpha_m(t) \phi_m(x) \qquad (8)$$

where $\alpha_m(t)$ are the expansion coefficients, which can be considered as the weights of each orthogonal function in the observed flow realization.

This decomposition has been found to be very effective in the sense that the first few orthogonal functions converge optimally fast, i.e., for a given order of truncation, the orthogonal functions will ret....: more flow information than Fourier modes.

Because only second-order statistics, $R(x_p, x_k)$, are used here, no higher-order statistics are embedded in these orthogonal functions. However, Lumley (1981) showed that higher-order statistics of experimental data are carried by the coefficients $\alpha_m(t)$. Thus, the orthogonal functions and their coefficients together retain all statistical information of the raw data. Note that although the coefficients $\alpha_m(t)$, as seen in Eq. (8), are unpredictable from one flow realization to another, their variation is not random. For example, if we consider $f_t(x)$ to be velocity, $\alpha_m(t)$ will be constrained by the Navier-Stokes equations.

b. Experimental data selection

The data to which the Proper Orthogonal Decomposition was applied were the same as used in section 2 for the dimension estimate. Since the dynamics of individual CS's are of interest here, the orthogonal functions will be extracted from an ensemble of visually selected

organized turbulent time series, instead of from the whole time series. This makes the resulting orthogonal functions more relevant to the coherent motions in the atmospheric surface layer. Visually screening the 60 minutes of data, fifteen "events" were selected which are considered to be CS's, based on their temporal variation and the vertical correlation of the velocity and temperature fluctuations, i.e., gust-ejection cycles of the velocity vector and ramp structures in the temperature fluctuations. Although the selected CS's show similar patterns, i.e., a strong updraft confined to a narrow region accompanied by wider downdrafts, their spatial (in the vertical direction) and temporal scales are all different. These fifteen CS's occupied only 36% of the total sampling time, but contributed more than 50% of the total momentum flux.

Because the tower provides data on a vertical cross-section of the three-dimensional turbulent structure, these selected "CS's" are two-dimensional. This precludes our modelling the important turbulent transfer mechanism, vortex stretching. Although most CS's exhibit a well-defined two-dimensional pattern, their dynamics are in principle three-dimensional. Previous studies by Kaimal and Businger (1970) and Schols et al. (1985) showed that the crosswind velocity v is relatively "inactive", i.e., no specific pattern can be seen in the v signal, during the large coherent events. But a recent analysis of experimental data collected by an instrumented aircraft (Williams and Hacker 1992) showed a clear in-flow pattern of a coherent structure in the cross-wind direction that varies with distance from the centre of the structure, i.e., flow variables of a coherent structure varied considerably in the cross-wind direction. However, without detailed

data in the cross-wind direction, the present study treats CS's as two-dimensional, i.e., it is assumed that the flow variations in the alongwind and vertical directions dynamically dominate the development of the CS's, and the flow in the cross-wind direction is simply driven by the continuity requirement.

The selection criteria introduce subjectivity, however, the "events" will not be averaged as in previous studies (Wilczak 1984; Schols et al. 1985). Instead, we will extract as much statistical information as possible from these CS's.

The 15 selected raw CS's were first interpolated from the height-time plane to a height-distance plane, using Taylor's frozen turbulence hypothesis. Since the data were collected during fairly windy conditions (see Table 1), the turbulence intensity, $\sqrt{e}/U$, was about 0.2 at most levels, and since observed CS's can maintain their identity for several minutes (Wilczak and Tillman 1980), the frozen turbulence hypothesis may not result in large error for the large-scale motions. Note that since an observed CS moves as an entity at a constant translational velocity (Wilczak 1984), to interpolate the data from temporal to spatial variation, one should use the translational velocity of the CS (assumed to be 90% of the mean velocity at the top of the layer), instead of the local mean velocity at each level. Thus, the fluctuations of the interpolated data are relative to the coordinate moving with the translational velocity. All the CS's are interpolated onto a horizontal distance of 620 m, the average horizontal extent of the CS's observed. The horizontal axis is divided into 31 bins (32 grid points), each with a horizontal length of 20 m. High wave-number fluctuations were removed by a low-pass Gaussian

filter having a half-power length of 5 m (Holloway 1957). The data were then interpolated from the original five levels (10m, 22m, 50m, 100m, and 150m) measured to eight levels (10m, 30m, 50m, 70m, 90m, 110m, 130m, 150m), using a cubic spline interpolation scheme, CSINT (IMSL 1989). A typical sample and its final form, after the filtering and interpolation, are plotted in Fig. 2 and 3. They show that the vertical velocity and the temperature within the selected CS's are well correlated, and the alongwind velocity has an obvious phase shift with respect to the vertical velocity. The phase shift between u and v is consistent with the observation that some of the alongwind velocity fluctuations are "inactive" in terms of momentum transport in the convective atmospheric surface layer (Hogstrom 1990).

c. Extraction of the orthogonal functions

The 15 filtered CS's, corresponding to 15 flow realizations over the region 620 m x 140 m, are used to form the two-point covariance matrix

$$R(x-x',z-z') = \frac{1}{15} \sum_{t=1}^{15} F_t^{T}(x,z)F_t(x',z')$$ (9)

where F_t (Fig. 4) is a composite series of velocities and temperature and (^{T}) denotes a transpose. $R(x-x',z-z')$ is a 768 x 768 matrix and contains information on the signal variances, the velocity covariances and the temperature-velocity covariances.

Substituting $R(x-x',z-z')$ (note that now R is defined in a two-dimensional (x-z) plane) into Eq. (7), the orthogonal functions (in two-dimensions) are obtained by numerically solving the eigenvalue problem. Because 15 experimental realizations of the CS are used to

create the matrix $R(x-x', z-z')$, only 15 non-zero eigenvalues can be calculated. The resulting orthogonal functions are structured the same way as F_t. The first three orthogonal functions are plotted in Fig. 5. We see that u and w are in general negatively correlated, w and θ are positively correlated, and that there is a clear correlation across the height range, as in the raw data (Fig. 3). Thus, the cross-correlation information is effectively retained in the decomposition of the velocity and temperature fields.

Forming a 15 x 768 matrix F of the 15 events (i.e., the 15 F_t) and a 768 x 15 matrix E of the 15 eigenfunctions and performing the matrix multiplication

$$F \times E = B \quad , \tag{10}$$

give us a 15 x 15 matrix B(t) consisting of the coefficients $\alpha_m(t)$, from which the statistics of the 15 eigenvalues are calculated (Table 2). The first orthogonal function captures 38% of the total variance and represents statistically the most likely common structure of the raw CS's; the corresponding expansion coefficient has a mean significantly different from zero (i.e., the first eigenfunction contributes strongly to the velocity and temperature fluctuations of the 15 events). The standard deviation of the expansion coefficients in Table 2 can be considered to be the variability of the orthogonal function (or mode) among the selected raw CS's. Since the first orthogonal function has a small standard deviation, it is relatively stable among the 15 selected raw CS's, and makes a persistent contribution to the observed flow structures (Eq. (8)). The first six orthogonal functions capture 80% of the total variance. This effective data representation by the orthogonal functions minimizes the number of

degree of freedom (Section 2) needed to model the flow, and is essential for derivation of the low-order model.

It should be emphasized that the orthogonal functions derived here are flow dependent. In general, we expect these orthogonal functions to depend on atmospheric stability, the Reynolds number, and even the mean wind speed. However, it is assumed that they have embedded enough physics to model the CS's in the convective atmospheric surface layer. Using the Navier-Stokes equations, we will now determine the evolution of the coefficients $\alpha_m(t)$, so that the evolving CS's can be described in terms of $\alpha_m(t)$ and the orthogonal functions as in Eq. (8).

d. Simplification of the Navier-Stokes equations

The instantaneous Navier-Stokes equations, in two-dimensions, and neglecting Coriolis force and molecular fluxes, are (Businger 1982)

$$\frac{\partial}{\partial t}\overline{\rho u_i} + \frac{\partial}{\partial x_j}\overline{\rho u_i u_j} = -\frac{\partial \overline{p}}{\partial x_i} - \overline{\rho}g\delta_{i2} \quad . \tag{11a}$$

The mass and thermodynamic energy conservation equations are

$$\frac{\partial \overline{\rho}}{\partial t} + \frac{\partial}{\partial x_i}\overline{\rho u_i} = 0 \tag{11b}$$

$$\frac{\partial \tilde{T}}{\partial t} + \frac{\partial}{\partial x_i}\overline{\tilde{T}u_i} = 0 \quad . \tag{11c}$$

In Eq. (11), the subscript notation $i = (1, 2)$ indicates coordinate directions, x, z, and the corresponding velocity components are u, v; the summation convention applies for indices repeated within terms; and δ_{i2} is the Kronecker delta.

Eq. (11) generate in a turbulent flow a broad range of temporal and spatial scales, involving a large number of degrees of freedom. To solve these equations numerically, an extremely small time step and a very fine grid spacing must be used. However, the data whence we extracted the orthogonal functions were spatially filtered instantaneous quantities; thus, the number of degrees of freedom represented in the experimental data has been greatly reduced. We now derive a set of equations governing the variables that have been filtered in the same manner as the experimental data.

Since a CS has a steady translational velocity, U_t, the following discussion will be with reference to a coordinate system moving with U_t. Firstly, we decompose the instantaneous quantities in Eq. (11) into horizontal means, denoted by an overbar, and fluctuations, i.e.,

$$\tilde{u}_i = \bar{U}_i(z,t) + u_i(x,z,t), \tag{12a}$$

$$\tilde{p} = \bar{P}(z,t) + p(x,z,t) , \tag{12b}$$

$$\tilde{T} = \bar{T}(z,t) + \theta(x,z,t) \text{ and} \tag{12c}$$

$$\tilde{\rho} = \rho_0 + \rho(x,z,t) . \tag{12d}$$

Here horizontal homogeneity has been assumed for the mean velocity, temperature and pressure fields (i.e., time-average means do not vary with x). The synoptic scale pressure gradient, which is in actuality imposed on the atmospheric surface layer and is at least partly responsible for the motion, has been assumed to have no direct effect on the dynamics of a CS. A similar assumption was made in Wilczak's (1984) study of coherent motions in the atmospheric surface layer. It also has been assumed that the horizontal mean temperature, T, equals

the adiabatic reference temperature, and that $\rho = \rho_0$, is a constant air density.

The Boussinesq approximation, in which density fluctuations are neglected unless coupled with gravity, is adopted, and the density fluctuation is expressed in terms of the temperature fluctuation,

$$\frac{\rho}{\rho_0} = -\frac{\theta}{T} \qquad . \tag{12e}$$

The governing equations for fluctuation velocity (u_i) and temperature (θ) are obtained by the standard technique of substituting into the instantaneous equation (Eq. (11)) the decompositions (Eq (12)), and subtracting the horizontal average value of the resulting equations, i.e., subtracting the evolution equations for U_i and T. The resulting equations are

$$\frac{\partial u}{\partial t} + \overline{U}\frac{\partial u}{\partial x} + w\frac{\partial \overline{U}}{\partial z} + \frac{\partial u^2}{\partial x} + \frac{\partial uw}{\partial z} - \frac{\partial \overline{uw}}{\partial z} = -\frac{1}{\rho_0}\frac{\partial p}{\partial x} \tag{13a}$$

$$\frac{\partial w}{\partial t} + \overline{U}\frac{\partial w}{\partial x} + \frac{\partial uw}{\partial x} + \frac{\partial w^2}{\partial z} - \frac{\partial \overline{w^2}}{\partial z} = -\frac{1}{\rho_0}\frac{\partial p}{\partial z} + \frac{\theta}{T}g \tag{13b}$$

$$\frac{\partial u}{\partial x} + \frac{\partial w}{\partial z} = 0 \tag{13c}$$

$$\frac{\partial \theta}{\partial t} + \overline{U}\frac{\partial \theta}{\partial x} + w\frac{\partial \overline{T}}{\partial z} + \frac{\partial u\theta}{\partial x} + \frac{\partial w\theta}{\partial z} - \frac{\partial \overline{w\theta}}{\partial z} = 0 \quad . \tag{13d}$$

Note that in Eq. (13b), the mean vertical pressure gradient was not assumed to be hydrostatic because there is strong vertical advection in the convective atmosphere, resulting in a "mean" vertical pressure gradient $1/\rho_0 \partial \overline{p_t}/\partial z = -\partial \overline{w^2}/\partial z$ (Wilczak and Businger 1984; Schumann and Moeng 1991).

The equations for the mean velocity and temperature are

$$\frac{\partial \bar{U}}{\partial t} + \frac{\partial \overline{uw}}{\partial z} = 0 \tag{14a}$$

$$\frac{\partial \bar{T}}{\partial t} + \frac{\partial \overline{w\theta}}{\partial z} = 0. \tag{14b}$$

Next, the departures from the horizontal average are further split into small volume means and fluctuations, using Schumann's (1975) fixed volume average scheme, i.e.,

$$u = \{u\} + u' \quad \text{and} \quad \{uw\} = \{u\}\{w\} + \{u'w'\}, \tag{15a}$$

$$\theta = \{\theta\} + \theta', \tag{15b}$$

$$p = \{p\} + p'. \tag{15c}$$

The "volume" over which the spatial averages { } are formed is a 20m x 20m bin. Spectral analysis of the present data (See Chapter V later) indicates that the lower frequency limit of the inertial subrange for horizontal velocity is around 0.1 Hz, at a mean wind speed of 8 $m \cdot s^{-1}$. Thus, the grid spacing $\Delta x = \Delta z = 20$ m is within the inertial subrange of turbulence in the atmospheric surface layer, except perhaps (on the evidence of Fig 1d of Chapter IV) at the 10 m level. In other words, the spacing is sufficiently fine to resolve the full range of energy containing eddies.

Substituting Eq. (15) into Eq. (13), and Reynolds averaging in the normal manner, one obtains

$$\frac{\partial \{u\}}{\partial t} + \bar{U}\frac{\partial \{u\}}{\partial x} + \{w\}\frac{\partial \bar{U}}{\partial z} + \frac{\partial}{\partial x}\{u\}^2 + \frac{\partial}{\partial z}\{u\}\{w\} - \frac{\partial \overline{uw}}{\partial z} + \frac{\partial \tau_{12}}{\partial z} = -\frac{1}{\rho_0}\frac{\partial}{\partial x}\{p^*\} \tag{16a}$$

$$\frac{\partial \{w\}}{\partial t} + \bar{U}\frac{\partial \{w\}}{\partial x} + \frac{\partial}{\partial x}\{u\}\{w\} + \frac{\partial}{\partial z}\{w\}^2 - \frac{\partial \overline{w^2}}{\partial z} + \frac{\partial \tau_{21}}{\partial x} - \frac{\{\theta\}}{\bar{T}}g = -\frac{1}{\rho_0}\frac{\partial}{\partial z}\{p^*\} \tag{16b}$$

$$\frac{\partial \{\theta\}}{\partial t} + \bar{U}\frac{\partial \{\theta\}}{\partial x} + \frac{\partial}{\partial x}\{u\}\{\theta\} + \{w\}\frac{\partial \bar{T}}{\partial z} + \frac{\partial}{\partial z}\{w\}\{\theta\} - \frac{\partial \overline{w\theta}}{\partial z}$$

$$+ \frac{\partial}{\partial x}\{u'\theta'\} + \frac{\partial}{\partial z}\{w'\theta'\} = 0 \quad . \tag{16c}$$

Here $\overline{uw}$, $\overline{w^2}$ and $\overline{w\theta}$ are the horizontal mean fluxes, invariant upon application of the small-volume average. In Eq. (16) the modified pressure has been introduced

$$\{p^*\} = \{p\} + \frac{1}{2}\rho_0 \{u_k'u_k'\} \quad , \tag{17a}$$

and the Reynolds stress due to unresolved scales of motion is defined as

$$\tau_{ij} = \{u_i'u_j'\} - \frac{1}{2}\{u_k'u_k'\}\delta_{ij} \quad . \tag{17b}$$

An eddy viscosity/diffusivity hypothesis was used to model the Reynolds stress and heat flux

$$\tau_{ij} = -K_m(\frac{\partial \{u_i\}}{\partial x_j} + \frac{\partial \{u_j\}}{\partial x_i}) \tag{17c}$$

$$\{u_i'\theta'\} = - K_h\frac{\partial \{\theta\}}{\partial x_i} \quad . \tag{17d}$$

The eddy diffusivity K_m has been specified as

$$K_m = (c\Delta\eta)^2\left|\frac{\partial \{u_i\}}{\partial x_j} + \frac{\partial \{u_j\}}{\partial x_i}\right| \quad , \tag{17e}$$

i.e., the Smagorinsky model, where c is a model constant and $\Delta\eta$ is the grid spacing. The eddy diffusivity K_m varies in space and time, consistent with the fact that in a turbulent flow the small-large scale interactions vary considerably. Lilly (1967) has shown that this formulation of K_m is consistent with the Kolmogorov power spectrum if $\Delta\eta$

is within the inertial subrange, i.e., $l_k \ll \Delta\eta \ll L$, where l_k is the Kolmogorov length scale and L the integral length scale. The eddy diffusivity for heat K_h is

$$K_h = \frac{K_m}{P_r} \qquad (17f)$$

where P_r is the turbulent Prandlt number, here taken as 0.74 (Businger 1982). It was assumed in (17b) that the turbulent kinetic energy of the unresolved scales is given by

$$\frac{1}{2}\{u_k{}'u_k{}'\} = \frac{K_m^2}{(c_1\Delta\eta)^2}$$

where $c_1 = 0.094$ (Deardorff 1970). Numerical calculation shows that the unresolved turbulent kinetic energy is less than 10% of the resolved turbulent kinetic energy.

The sources of turbulent kinetic energy in this system are shear production and buoyant production, which are parameterized in terms of the mean gradients of velocity U and temperature T, respectively. The turbulent interactions in the resolved scales (but not including the vortex stretching) are inherently modelled by the interactions of the orthogonal functions. The sink of turbulent energy in this system is the subgrid energy cascade (from Eq. (16 a,b))

$$\{u\}\frac{\partial\tau_{12}}{\partial z} + \{w\}\frac{\partial\tau_{21}}{\partial x}, \qquad (18)$$

which, using Eq. (17c) can be written as

$$\frac{\partial(\{u\}\tau_{12})}{\partial z} + \frac{\partial(\{w\}\tau_{21})}{\partial x} - K_m\left(\frac{\partial\{u\}}{\partial z} + \frac{\partial\{w\}}{\partial x}\right)^2$$

Upon integration over the flow domain, the first two terms will be zero (assuming horizontal homogeneity), and the last term is always negative. Thus, although they may not model the instantaneous energy cascade processes correctly, on average, the subgrid terms always take energy from the structures, i.e., they act as a filter to prevent excessive turbulent kinetic energy in resolved scales. For a given resolved velocity field ({u}, {w}), the subgrid terms vary with the model parameter c.

The small-volume average applied in Eq. (16) not only filters out turbulence with scales smaller than our grid volume in the observations but also explicitly incorporates into the governing equations all the dynamic effects of the unresolved turbulence on the large-scale flow. That is, Eq. (16) are the modified Navier-Stokes equations that govern the resolved scales, and mimic the energy cascade processes from resolved scales to unresolved scales by the eddy diffusivity model. Quantities in Eq. (16) are now equivalent to the low-pass filtered data (Section 3b), from which the orthogonal functions were extracted. Eq. (16), when combined with the model (Eq. (17)) are the basis for deriving the low-order model (and could equally well serve as a Large-eddy-simulation in two dimensions).

e. The low-order model

From now on, the bracket { }, indicating the small-volume averaged quantities, will be dropped. Decomposing velocities and temperature into N orthogonal components as in Eq. (8)

$$u(x,z,t) = \sum_{m=1}^{N} \alpha_m(t) \ \phi_m^u(x,z) \tag{19a}$$

$$v(x,z,t) = \sum_{m=1}^{N} \alpha_m(t) \, \overset{v}{\phi}_m(x,z) \tag{19b}$$

$$\theta(x,z,t) = \sum_{m=1}^{N} \alpha_m(t) \, \overset{\theta}{\phi}_m(x,z) \ , \tag{19c}$$

For an incompressible flow, i.e. $\partial u/\partial x + \partial w/\partial z = 0$, it is easy to prove, from Eq. (19a,b), that

$$\frac{\partial \overset{u}{\phi}_m}{\partial x} + \frac{\partial \overset{w}{\phi}_m}{\partial z} = 0 \quad . \tag{20}$$

The low-order equations are obtained by substituting Eq. (19) into Eq. (16), then applying Galerkin projection, i.e., by taking the inner product

$$\iint E^i \cdot \overset{i}{\phi}_m \, dxdz = 0 \ , \tag{21}$$

where the integral extends over the flow domain (620 m x 140 m), and i = (u, w, θ). E^u, E^w, and E^θ represent, respectively the u, w momentum equations, and the thermodynamic energy equation. Using the orthogonal property of the orthogonal functions, i.e.,

$$\iint \overset{i}{\phi}_j \cdot \overset{i}{\phi}_m \, dxdz = \iint (\overset{u}{\phi}_j \overset{u}{\phi}_m + \overset{w}{\phi}_j \overset{w}{\phi}_m + \overset{\theta}{\phi}_j \overset{\theta}{\phi}_m) \, dxdz = \delta_{jm} \tag{22}$$

(no summation implied by the repeated superscripts)

in Eq. (16), one obtains a set of N ordinary differential equations

$$\frac{d\alpha_m}{dt} = \sum_{i,j=1}^{N} (^1c_{ij}^m + {}^2c_{ij}^m)\alpha_i\alpha_j + \sum_{i,j,k=1}^{N} c_{ijk}^m \alpha_i \alpha_j \alpha_k$$

$$+ \iint (-\frac{1}{o} \nabla p^* \cdot \overset{v}{\phi}_m) \, dxdz \tag{23}$$

m = 1, . . ., N.

The coefficients ($^1c_{ij}^m$, $^2c_{ij}^m$, and c_{ijk}^m) in Eq. (23) are determined by the

spatial variability of the orthogonal functions, the temporal variability of the mean quantities ($\bar{U}$, $\partial\bar{U}/\partial z$, $\bar{T}$ and $\partial\bar{T}/\partial z$), and the subgrid terms. The quadratic terms are of two kinds: the first ($^1c_{ij}^m$) results from the nonlinear interactions among the orthogonal functions, the second ($^2c_{ij}^m$) is due to the subgrid modelling. The cubic terms c_{ijk}^m come from the mean-fluctuation interactions. The last term in Eq. (23) is the pressure forcing term which will be discussed later. A detailed expression of Eq. (23) is given in Appendix D.

When substituting Eq. (19) into the governing Eq. (16), it has been assumed that the turbulent fluctuations in the model system are solely caused by the interactions among the N orthogonal functions and their interaction with the mean velocity and temperature fields. The more orthogonal functions included, the closer the simulation should model the reality. Therefore all 15 orthogonal functions have been used in the velocity decomposition (Eq. (19)). As mentioned earlier the 15 CS's contributed more than 50% of the total Reynolds stress over the 60 min, indicating that they probably are capable of modelling the most important dynamics of the two-dimensional CS's.

In reality, a CS in the atmospheric surface layer involves interactions of many different scales. This implies that the parameterization of the unresolved scales (Eq. (17)) must model the contributions from both subgrid turbulence and the large-scale turbulence that is not explicitly included in this study. This conflicts with the basic assumption that the eddy diffusivity formulation models only the small-scale turbulence. No attempt was made to account for the effect this approximation (Eq. (17)) may have on the simulations in this study.

4. Numerical Integration of the Low-Order Dynamic Equations

In this section, the calculation of the coefficients $^1c_{ij}^m$, $^2c_{ij}^m$, c_{ijk}^m and the pressure forcing term are discussed, as they are important in determining the general properties of the low-order dynamic equations. This is followed by a brief discussion of the initial conditions and the numerical simulation.

a. Calculation of the coefficients and pressure forcing term of the low-order model

All of the coefficients in Eq. (23) involve derivatives of the orthogonal functions. But, except for the first few, the experimentally determined orthogonal functions are not smooth, and using a finite difference scheme to calculate their derivatives would likely result in a large error. A better method for calculating the derivatives of a non-smooth function is the Fourier transform method, often used in spectral fluid dynamics (Moeng 1984; Qanuto et al. 1988). For example, to obtain df/dx, f is Fourier transformed first

$$F(k_m,z) = \frac{1}{N} \sum_{n=1}^{N} f(x_n,z)\exp(-ik_m x_n) \quad , \tag{24}$$

where N is the number of grid points in x direction, $k_m = 2\pi m/N\Delta x$ (m = -N/2+1, ..., N/2) is the wave number and $x_n = n\Delta x$. Applying the derivative operator in the Fourier space, i.e., multiply $F(k_m,z)$ by ik_m, and taking the inverse Fourier transform of $ik_m F(k_m,z)$, one obtains the derivative in physical space

$$\left(\frac{\partial f}{\partial x}\right)_n = - \sum_{m=-N/2+1}^{N/2} ik_m F(k_m,z)\exp(ik_m x_n) \quad . \tag{25}$$

The quadratic term $^{1}c_{ij}^{m}$ is easily calculated in this way from the orthogonal functions and their derivatives. The other quadratic terms, $^{2}c_{ij}^{m}$ and the cubic terms c_{ijk}^{m}, need to be evaluated at each time step, because of the required calculation of the absolute value of the strain rate in the subgrid stress terms (Eq. (17e)), and the mean flow quantities.

The pressure forcing term appearing in Eq. (23) is

$$\Pi = -\frac{1}{\rho_0} \iint \left[\frac{\partial p^*}{\partial x} \phi_m^u + \frac{\partial p^*}{\partial z} \phi_m^w \right] dx dz \quad . \tag{26}$$

For our two-dimensional study, the velocity divergence ($\partial u/\partial x + \partial w/\partial z$) of the experimental data is in general non-zero. Nevertheless, in order to determine the pressure, the simulated flow field was forced to satisfy $\partial u/\partial x + \partial w/\partial z = 0$. This constraint changes the values of the coefficients α_m in Eq. (23), as if they satisfied the two-dimensional continuity equation $\partial u/\partial x + \partial w/\partial z = 0$. The implication of this constraint will be discussed later.

Incompressiblity in two dimensions $\partial u/\partial x + \partial w/\partial z = 0$ means that pressure is determined diagnostically at each time step by a two-dimensional Poisson equation

$$\frac{\partial^2 p^*}{\partial x^2} + \frac{\partial^2 p^*}{\partial z^2} =$$

$$-\rho_0 \left(2\frac{\partial \bar{U}}{\partial z}\frac{\partial w}{\partial z} + \frac{\partial^2 u^2}{\partial x^2} + 2\frac{\partial^2 uw}{\partial x \partial z} + \frac{\partial^2 w^2}{\partial z^2} - \frac{\partial^2 \overline{w^2}}{\partial z^2} + 2\frac{\partial^2 \tau_{12}}{\partial x \partial z} - \frac{g}{T}\frac{\partial \theta}{\partial z} \right). \tag{27}$$

After taking the Fourier transform of Eq. (27) in the x direction and using finite differences in the z direction, the resulting tridiagonal matrix was inverted using the Thomas algorithm (Von Rosenberg 1969) to obtain p* in Fourier space, with Neumann boundary conditions derived

from Eq. (16b). The p* in Fourier space was then inverse transformed to get the pressure at each grid point. The newly calculated pressure is used to evaluate the pressure term (Eq. (26)) which appears in the evolution equation (Eq. (23)) for $\alpha_m(t)$. Note that the non-divergence property of the orthogonal functions (Eq. (20)) is particularly useful to simplify the calculation of the pressure term. For example, using Eq. (20), Eq. (26) can be written as

$$\Pi = -\frac{1}{\rho_0} \iint \left[\frac{\partial}{\partial x}(p^* \phi_m^u + \frac{\partial}{\partial z}(p^* \phi_m^w) \right] dxdz \quad . \tag{28}$$

After carrying out the integration, one can easily show that only the pressure fluctuations (obtained from the Eq. (27)) at the domain boundary influence the evolution of the coefficients, and thus are used.

b. Initial condition

Because of the nonlinearity of the governing equations, evolution of a flow is very sensitive to the initial conditions for the large-scale structures (Rogallo and Moin 1984). The optimum initial condition for the present short-term simulation is that set of coefficients $\alpha_m(t)$ which represents a "snapshot" of the flow. This can be easily obtained by rewriting the simple relationship of Eq. (10)

$$F \times E = B \quad . \tag{29}$$

The resulting 15 x 15 matrix B(t) consists of 15 sets of coefficients $\alpha_m(t)$ (m = 1, 2, ..., 15), each corresponding to a snapshot of the flow realization.

Given a set of $\alpha_m(t)$ obtained from Eq. (29) as an initial condition, the system Eq. (23) determines the time histories of the coefficients, from which the evolution of the CS in a coordinate system moving with the translational velocity, U_t, is obtained. The initial

velocity and temperature profiles are also taken directly from the measured values. The temporal variation of mean velocity and temperature are calculated using horizontally averaged equations, i.e., Eq. (14), which states that the local temporal changes in mean velocity and temperature are due to the convergence of vertical momentum flux and heat flux, respectively.

Eq. (23) are advanced using the second order Runge-Kutta scheme (Qanuto et al. 1988). The simulations showed no sensitivity to time step when the time step Δt was less than two seconds. The present simulations use a $\Delta t = 1$ s, which is much smaller than the time step required for linear computational stability $\Delta t \leq \Delta x/\overline{U}$. At each time step the current values of $\alpha_m(t)$ can be used to form the current velocity and temperature fields by Eq. (19)[1] . Since the velocity and temperature fluctuations can be reconstructed easily and the pressure can be calculated from Eq. (27), only the coefficients $\alpha_m(t)$ are stored at each time step during the simulations. This allows a fast numerical simulation. One minute of real time requires about 20 seconds CPU time on a Vax station 3100 (model 30, 2.8 VUPF). Appendix E provides a flow chart for solution of the low-order equations.

It has been assumed that the orthogonal functions have embedded not only the internal dynamics of the CS's, but also all the external effects, such as the surface heating, on the CS's. With the time history of the coefficients $\alpha_m(t)$ obtained from the simulations,

---

1. Note that since the basis functions have non-zero divergence, $\partial\phi^u/\partial x +\partial\phi^w/\partial z \neq 0$, using Eq. (19) to form the velocity field conflicts with the assumption of two-dimensionality used to obtain the pressure. However, if $\partial v/\partial y$ is small for these CS's, as indicated in previous studies, one expects that this would not result in large error in a short-time numerical simulation.

Eq. (19) will give the fluctuating velocities, u, w, and temperature, θ, at each grid point (including the boundary) of the calculation domain. Thus, there is no need to specify boundary conditions, and we are simulating a flow field within a moving domain (620 m x 140 m). What we observe is expected to be much like watching the atmosphere from a window moving at a speed U_t.

The nonlinear dynamics of turbulence in the atmospheric surface layer imposes a limit on long-term prediction. Even though the low-order model has been constructed from first principles, the predicted flow evolution will differ from reality beyond the time of predictibility, due to errors in the initial conditions, and in the model for the unresolved motions (Section 3). This is an inherent problem for turbulence modelling (Herring 1979). Furthermore, the two-dimensional assumption imposes another potential error in flow evolution at large time. Therefore, provided the initial condition is correct, a short numerical simulation is preferred.

5. Discussion of the Low-Order Model

There are certain aspects of this low-order model that need to be improved in any future study. An obvious limitation of the model is the assumption of two-dimensionality of the CS's, which are in fact three-dimensional. This not only restricts the numerical simulation to a very short period of time, but also may inherently modify the simulated flow structures. Deardorff and Willis (1965) have discussed the tendency of two-dimensionality to prevent small-scale irregular turbulence arising, due to lack of the normal three-dimensional energy

cascade. It is not possible, at present, to sample simultaneously atmospheric turbulence at points covering a large three-dimensional space, as would have been required for this kind of study.

Another problem is the modelling of unresolved motion. It may be adequate to model the effect of the subgrid-scales on the large-scales by the eddy diffusivity concept. But our closure model (with its constant, c) accounts not only for the effect of small-scale turbulence, but also the neglected large-scale turbulence. There may be a need to model these two effects separately, especially for a long-time simulation, so that the variation of simulations with model constants can be studied with clear physical interpretation.

The model is flow specific, i.e., it applies only to coherent motion in the convective atmospheric surface layer. Under neutral and stable conditions, the orthogonal functions which determine the properties of the model will be different, and the model cannot be applied.

In view of these limitations, and since only fifteen orthogonal functions have been used as the basis functions to simulate the flow, one cannot expect the model to accomplish tasks other than an approximate representation of coherent motions within a short period of time. Nevertheless, comparing with previous studies, it is felt that the present model is more rational because it directly incorporates experimental information to form a mathematical framework, avoiding subjectivity.

Finally, the dynamical systems theory has been used here only to provide guidelines for building a low-order model. Apart from implicitly suggesting their "existence", no attempt was made to study

he underlying attractors. Further study should focus on the quantitative behaviour of the underlying attractor, such as the Lyapunov Exponents (Berge 1984) which measure the sensitivity of the phase trajectories to small changes in initial conditions, i.e., the predictability.

6. Summary

Based on experimental evidence and a simple application of the dynamical systems theory, a low-order model, i.e., a set of 15 ordinary differential equations derived from the highly truncated Navier-Stokes equations, and the mass and energy conservation equations, has been developed to study coherent motions in the convective atmospheric surface layer. The model incorporates experimental information (the empirical basis functions) into a mathematical framework, and treats the initial and boundary conditions objectively. Therefore, the model provides a means to study instantaneous coherent dynamics. In Chapter V, the model simulations will be used to study the dynamics and energetics of convective plumes in the atmospheric surface layer.

Acknowledgements

Table 1
Boulder Atmospheric Observatory data summary
25 July 1986 10:20 – 11:20 am

Height (m)	Mean speed ($m \cdot s^{-1}$)	Momentum flux ($m \cdot s^{-1}$)^2	Heat flux ($W\ m^{-2}$)	M-O length (m)	Turbulence intensity*
150	8.06	-0.12	217	-17	20%
100	7.96	-0.23	289	-35	20%
50	7.62	-0.36	313	-62	21%
22	7.25	-0.20	265	-31	21%
10	6.07	-0.21	229	-39	26%

* defined as $\sqrt{e}/U$, where $e = 1/2(u^2+v^2+w^2)$ is the turbulent kinetic energy.

Table 2
Expansion statistics for the eigenfunctions obtained by Proper
Orthogonal Decomposition of the 15 visually selected CS's.

Eigenfunction number	Expansion coefficient		Eigen-value	Accumulated variance explained %
	Mean	Std (σ)		
1	-0.90	0.41	0.96	38
2	0.08	0.61	0.36	52
3	-0.03	0.49	0.22	61
4	0.01	0.43	0.18	68
5	0.0	0.43	0.17	74
6	0.0	0.40	0.15	80
7	0.0	0.32	0.09	84
8	0.05	0.30	0.08	87
9	0.0	0.27	0.07	90
10	-0.04	0.26	0.06	93
11	0.02	0.24	0.05	95
12	0.04	0.21	0.04	96
13	0.0	0.19	0.04	97
14	0.02	0.18	0.03	99
15	0.00	0.17	0.02	100

Note: since the data were normalized, the eigenvalues and
expansion coefficients listed in this Table have no units.
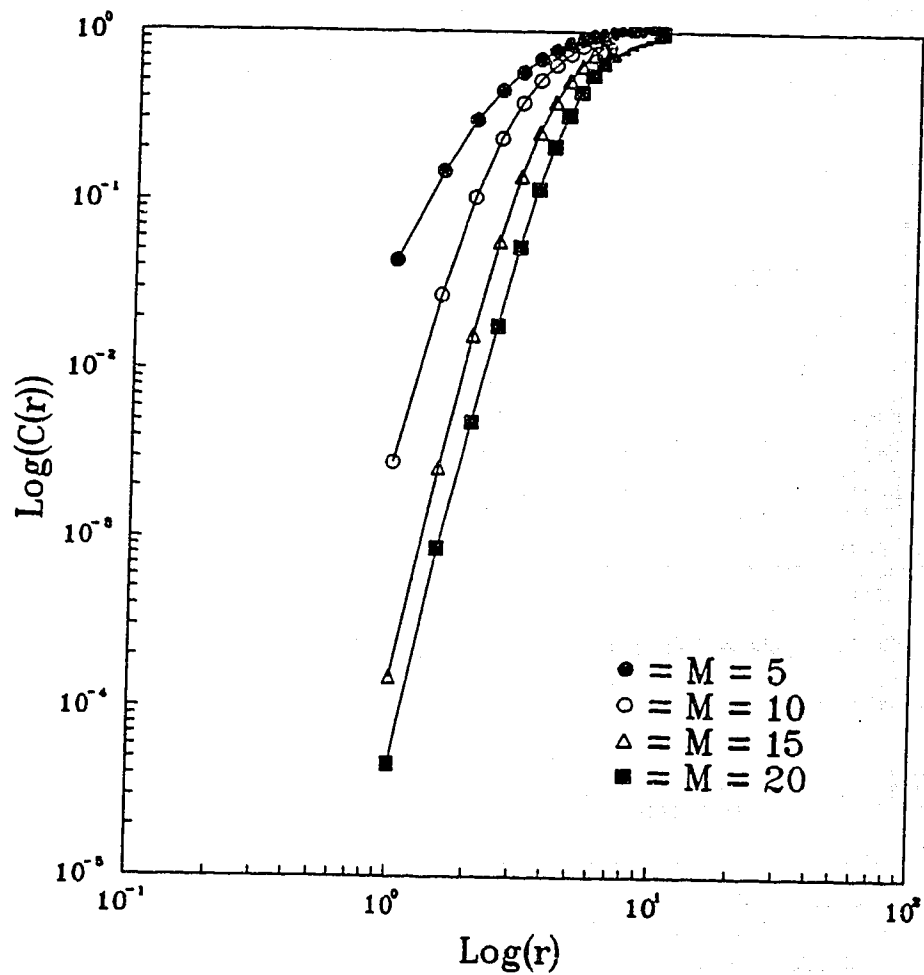
Fig. 1   Correlation integral calculated from Eq. (6) with the reconstructed phase space having embedding dimensions M ranging from 5 to 20 (i.e., from a single variable (w) to four variables (w, θ, u, v)).
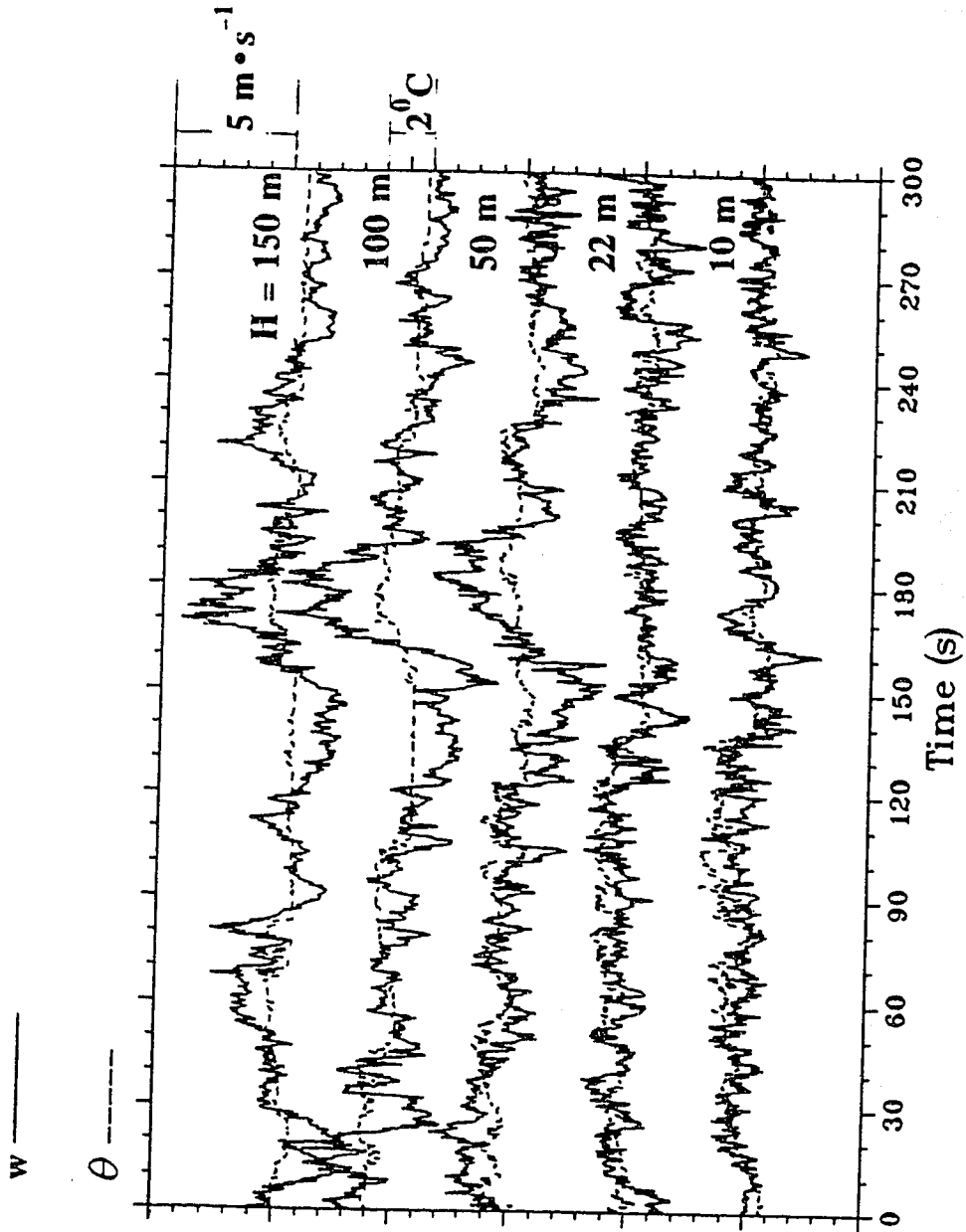
Fig. 2 Time series of velocities and temperature observed during the passage of a CS in the convective atmospheric surface layer.
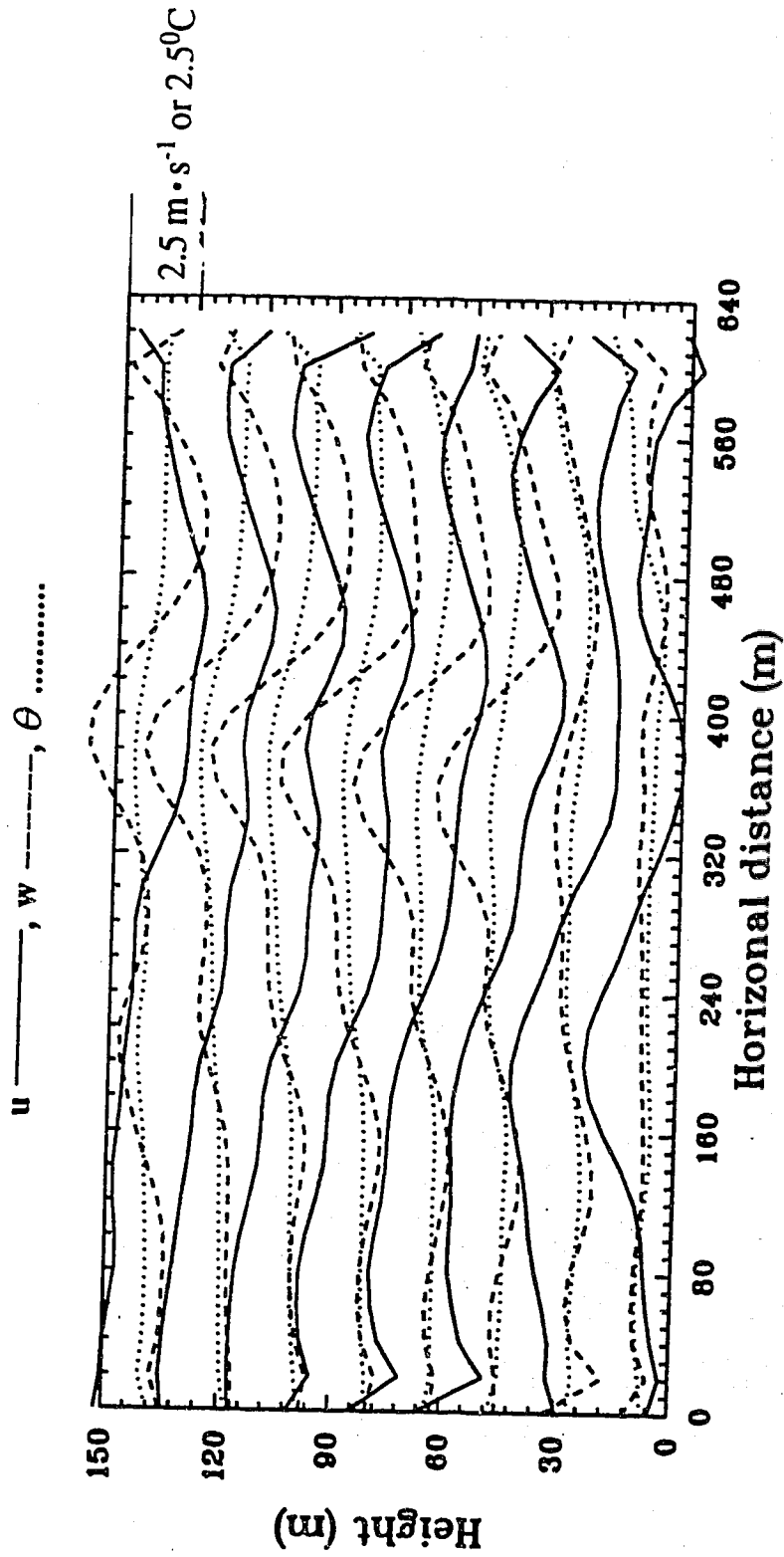
Fig. 3   Velocity (u, w) and temperature (θ) fluctuations of the CS in Fig. 2 after filtering and interpolating.

$F_t(x,z)$

| $u_t(1,1)$ | $v_t(1,1)$ | $\theta_t(1,1)$ | . . . | $u_t(32,8)$ | $v_t(32,8)$ | $\theta_t(32,8)$ |
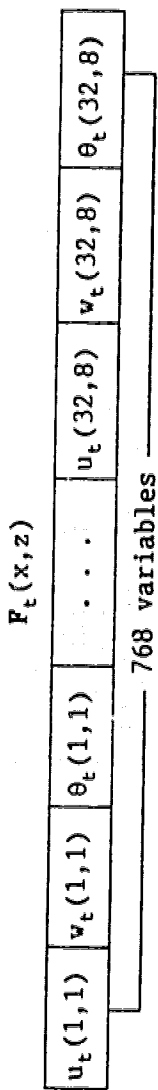
768 variables

Fig. 4 Stacking the flow variables of a selected coherent event as a vector for matrix calculation in Eq. (11). The 768 entries are fluctuations derived from: 32 (grids) x 8 (levels) x 3 (variables).
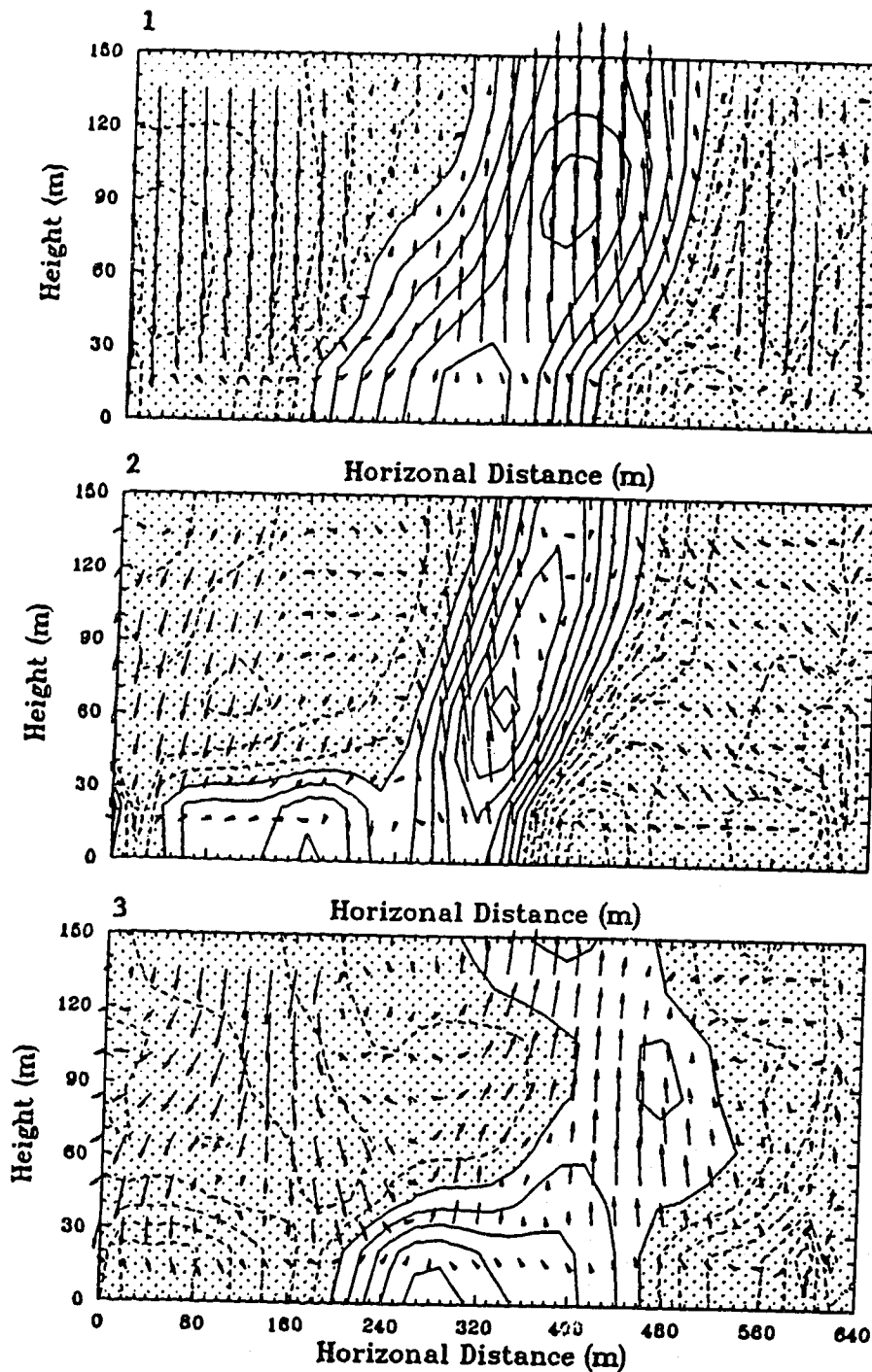
Fig. 5 First three orthogonal functions obtained from the Proper Orthogonal Decomposition of the ensemble observed CS's. The orthogonal functions have no unit. The variables are normalized by the root-mean-square of their respective values averaged over the whole domain. The contours (with arbitrary unit) depict temperature fluctuations, with negative values shaded.

REFERENCES

Antonia, R.A., S. Rajagopalan, and A.J. Chambers, 1983: Conditional sampling of turbulence in the atmospheric surface layer. J. Climate Appl. Meteor., 22, 69-78.

Aubry, N., P. Holmes, J. Lumley and E. Stone, 1988: The dynamics of coherent structures in the wall region of a turbulent boundary layer. J. Fluid Mech. 192, 115-173.

Berge, P., Y. Pomeau, and C. Vidal, 1984: Order within chaos. John Wiley & Sons. N.Y., 274 pp.

Businger, J.A., 1982: Equations and concepts. Atmospheric Turbulence and Air Pollution Modelling, F.T.M. Nieuwstadt and H. Van Dop, eds., Reidel Publishing Company, 1-36.

Deardroff, J.M., 1971: On the Magnitude of the Subgrid Scale Eddy Coefficient. J. Comput. Phys. 7, 120-133.

Deardroff, J.W., and G.E. Willis, 1965: The effect of two dimensionality on the suppression of thermal turbulence. J. Fluid Mech., 23, 337-353.

Grassberger, P., and I. Procaccia, 1983: Characterization of strange attractors. Physical Review Letter, 50, 346-349.

Guckenheimer, J., 1986: Strange attractors in fluids: another view. Ann. Rev. Fluid Mech., 18, 15-31.

Hanna, S.R., 1981: Lagrangian and Eulerian time scale relation in daytime boundary. J. Appl. Meteoro., 20, 242-249.

Hunt, J.C.R., J.C. Kaimal, and J.E. Gaynor, 1988: Eddy structure in the convective boundary layer-new measurements and new concepts. Q.J.R. Meteorol. Soc., 114, 827-858.

Herring, J.R.,1979: Subgrid scale modeling-an introduction and overview. Turbulent Shear flow I, F. Durst, B.E. Launder, F.W. Schmidt and J.H. Whitelaw, Eds., Springer-Verlag, 347-352.

Holloway, J.L. Jr., 1957: Smoothing and filtering of time series and space fields. Advances in Geophys. 4, Academic Press. N.Y.

Hogstrom, U., 1990: Analysis of turbulence structure in the surface layer with a modified similarity formulation for near neutral conditions. J. Atmos. Sci., 47 1949-1972.

IMSL, 1989: IMSL. Stlb-USM-Perfct-1.0.

Kaimal, J.C., and J.A. Businger, 1970: Case studies of a convective plume and a dust devil. J. Applied Meteoro., 9, 612-620.

Laudau, L.D., 1944: Dokl. Akad. Nauk SSSR, 44, 339.

Lewellen, W.S., and M. Teske, 1973: Prediction of the Monin-Obukhov similarity functions from an invariant model of turbulence. >J. Atmos. Sci. 30, 1340-1345.

Lily, D.K., 1967: The representation of small-scale turbulence in numerical simulation experiments. Proc. IBM Scientic Computing Symp. on environmental Science. IBM form No. 320-1951 195-210.

Lorenz, E. N., 1972: Low order models representing realizations of turbulence. J. Fluid Mech., 55, 545-563.

Lorenz, E. N., 1991: Dimension of Weather and Climate Attractors. Nature. 353, 241-244.

Lumley, J.L., 1967: The structure of inhomogeneous turbulent flows. Atmospheric turbulence and radio wave propagation. A.M. Yaglom, and V.I. Tatarski. eds., Moscow, Nauka., 166-178.

Lumley, J.L., 1981: Coherent structures in turbulence. Transition and turbulence. R.E. Meyer. ed., Academic press. 215-242.

Mahrt, L., 1991: Eddy Asymmtry in the sheared heated boundary layer. J. Atmos. Sci., 48, 472-492.

Moeng, C-H.,1984: A large-eddy simulation model for the study of planetary boundary-layer turbulence. J. Atmos. Sci., 41, 2052-2062.

Monin, A.S., 1978: On the nature of turbulence. Soc. Phys. Usp., 21(5), 429-442.

Newell, A.C, D.A. Rand, and D. Russell, 1988: Turbulent transport and the random occurrence of coherent events. Physica D33, 281-303.

Packpard, N.H., J.P. Crutchfield, J.D. Farmer, and R.S. Shaw, 1980: Geometry from a time series. Phys. Rev. Lett. 45, 712.

Qanuto, C., M.Y. Hussaini, A. Quarteroni, and T.A. Zang, 1988: Spectral Methods in Fluid Dynamics. Springer-Verlag. 557 pp.

Orszag, A.S., 1972: Comparison of pseudospectral and spectral approximations. Stud. Appl. Math., 51, 253-259.

Rogallo, R.S., and P. Moin, 1984: Numerical simulation of turbulent flow. Ann. Rev. Fluid Mech., 16, 99-137.

Ruelle, D., and F. Takens, 1972: On the nature of turbulence. Comm. Math. Phys., 82, 137-151.

Ruelle, D., 1981: Chemical kinetics and differentiable dynamical systems. Nonlinear phenomena in chemical dynamics. A. Pacault and C. Vidal, ed., Berlin, Springer-Verlag.

Schmidt, H., and U. Schumann, 1989: Coherent structure of convective boundary layer derived from Large-Eddy Simulation. J. Fluid Mech. 200, 511-562.

Schumann, U., 1975: Subgrid scale model for finite difference simulations of turbulent flows in plane channels and annuli. J. Comput. Phys., 18, 376-404.

Schumann, U., and C-H. Moeng, 1991: Plume budgets in clear and cloudy convective boundary layers. J. Atmos. Sci., 48, 1758-1770.

Schols, J.L.J., 1984: The detection and measurement of turbulent structures in the atmospheric surface layer. Bound.-Layer Meteor. 29, 39-58.

Schols, J.L.J., A.E. Jansen, and J.G. Krom, 1985: Characteristics of turbulent structures in the unstable atmospheric surface layer. Boundary-Layer Meteor., 33, 173-196.

Sreenivasan, K.R., 1985: Transition and turbulence in fluid flows and low-dimensional chaos. Frontier in Fluid Mechanics, Davis, S.H. and Lumley, J.L., eds, p 41-67.

Takens, F., 1981:Detecting strange attractors in turbulence. Dynamical systems and turbulence, Warwick, 1980. D.A. Rand and L.-S. Young, eds., 306-381.

Telford, J.W., 1970: Convective plumes in a convective field. J. Atmos. Sci. 27, 347-358.

Tennekes, H., 1978: Fourier-transform ambiguity in turbulence dynamics. J. Atmos. Sci., 33, 1660-1663.

Tsonis, A.A., and J.B. Elsner, 1989: Chaos, strange attractors and weather. Bull. Ameri. Meteor. Soc. 70, 14-23.

Tsonis, A.A., J.B. Elsner and K.P. Georgakakos, 1993: Estimating the Dimension of Weather and Climate Attractors: Important Issues about the Procedure and Interpretation. J. Atmos. Sci. 50,2549-2555.

Turner, B.J. and M.Y. Leclerc, 1992: Conditional sampling of structures in turbulence using the wavelet transform. 10th Symposium on Turbulence and Diffusion, 214-217.

von Rosenberg, D. U., 1969: Methods for the numerical solution of partial differential Equations. Elsevier, N.Y., 128pp.

Wilczak, J.M., and J.E. Tillman, 1980: The three-dimensional structure of convection in the atmospheric surface layer. J. Atmos. Sci., 37, 2424-2442.

Wilczak, J.M., 1984: Large-scale eddies in the unstably stratif₃ d atmospheric surface layer. part I: velocity and temperature structure. J. Atmos. Sci., 41, 3537-3550.

Wilczak, J.M., and J.A. Businger, 1984: Large-scale eddies in the unstably stratified atmospheric surface layer. part II: turbulent pressure fluctuations and the budgets of heat flux, stress and turbulent kinetic energy. J. Atmos. Sci., 41, 3551-3567.

Williams, A.G. and J.M. Hacker, 1992: The composite shape and structure of coherent eddies in the convective boundary layer. Bound. -Layer Meteorology. 61, 213-245.

Wyngaard, J.C., 1980: The atmospheric boundary layer modelling and measurements. In Turbulent Shear Flows 2, Bradbury, L.J.S., F. Durst, B.E. Launder, F.W. Schmidt and J.H. Whitelaw (eds), Springer-Verlag, New-York, 352-365.

Wyngaard, J.C., 1984: Large-eddy simulation: guidelines for its application to planetary boundary layer research. Final report for the U.S. Army Research Office. Contract No. 0804., 122pp.

Wyngaard, J.C., 1988: Structure of the PBL. Air pollution modeling. A. Venkatram, and J.C. Wyngaard, ed., 9-62.

Young, G.S., 1988: Turbulence structure of the convective boundary layer. Part III: the vertical velocity budgets of thermals and their environment. J. Atmos. Sci. 45, 2039-2049.

CHAPTER V

DYNAMICS AND ENERGETICS OF CONVECTIVE PLUMES IN

THE ATMOSPHERIC SURFACE LAYER

1. Introduction

A plume in the convective atmospheric surface layer is an isolated

volume of buoyant fluid with a highly anisotropic, coherent (i.e.,

spatially and temporally correlated) flow structure. The existence of

the plumes in the atmosphere has been attributed to both convection in

the presence of shear, and to hydrodynamic instability of the mean

velocity profile (Brown 1980). Coherent motions under forcing by the

curvature of the vertical profile of mean velocity align themselves in

the mean flow direction (Schols et al. 1985). Wilczak and Tillman

(1980) showed that most of the plumes observed in the atmospheric

surface layer first appear at ground and grow in height, suggesting

buoyancy may be a production mechanism. But Antonia et al. (1979),

comparing organized velocity and temperature fluctuations observed in

the atmospheric surface layer and in an adiabatic laboratory boundary

layer, suggested that the internal dynamics of atmospheric plume

structures and the laboratory ejection (or burst) events are closely

related. The study by Antonia et al. (1979) was conducted in the first

few meters of the atmosphere where, as has been shown (Zhuang and

Wilson 1992), the transport characteristics of plumes change little

with atmospheric stability. However, at higher levels, due to reduced

shear production of turbulent kinetic energy $-\overline{uw}\partial U/\partial z$ and roughly

height-independent buoyant production $\overline{w\theta}g/\overline{T}$, turbulent structures may

98

be significantly different from those in a laboratory boundary layer. An experimental study of turbulence structure in the convective atmospheric boundary layer by Hunt et al. (1988) stated "turbulence within the thermal undergoes distortion by large-scale eddies and cannot be regarded as locally independent motions driven simply by the shear on each thermal, but the nature of this interaction is poorly understood".

The dynamics of convective plumes in the atmospheric surface layer were investigated by Wilczak (1984) and Wilczak and Businger (1984). By forming two-dimensional (x-z) cross-sections of velocities and temperatures from an ensemble of conditionally sampled plumes, Wilczak showed that turbulent fluxes of momentum and heat, as well as third-order moments, can be interpreted in terms of the circulations associated with the plumes' velocity and temperature structures. By calculating the pressure field within the plumes, using the momentum equations, Wilczak and Businger showed that the convective plumes also make the dominant contribution to the pressure covariance terms in the budgets of vertical and horizontal heat fluxes, stress and turbulent kinetic energy. In Wilczak and Businger's study, the dynamics of the convective plumes were discussed in terms of their effects on the ensemble-averaged properties in the atmospheric surface layer. It is felt that an analysis of the detailed dynamics within the plumes themselves is needed.

The primary objective of this study is to examine further the dynamics (momentum budgets) and energetics (turbulent kinetic energy budgets) of the convective plumes, emphasizing aspects that are related to their persistence in the atmospheric surface layer. Turbulence

statistics resulting from the coherent motion are also calculated to show their influence on the routinely measured unconditional turbulent statistics. Implications of this study for atmospheric turbulence modelling will be briefly discussed.

The following discussion will be based on experimental observations of 15 convective plumes (Chapter IV), and on calculated pressure fluctuation fields and short-term flow evolutions obtained using the low-order model developed in Chapter IV.

2. Low-order Model Simulations

In Chapter IV, a low-order model (15 ordinary differential equations) for studying coherent dynamics was developed by performing a Galerkin projection of the Navier-Stokes equations onto a set of 15 orthogonal functions. These orthogonal functions were obtained by decomposing an ensemble of experimentally observed plumes with the Proper Orthogonal Decomposition method (Lumley 1981). It was assumed that the orthogonal functions are typical of large-scale turbulent velocity and temperature fluctuations in the convective atmospheric surface layer, and have embedded the most important aspects of the coherent motion. The model provides a means to study instantaneous coherent dynamics.

The only model parameter that needs to be fixed is c, an arbitrary constant in the Smagorinsky model, which accounts for the influence of the unresolved scales. The constant c was chosen by inspection of the simulated velocity spectra, which are very sensitive to the model of unresolved motions (Deardorff 1971). It was found in this simulation

that the velocity spectra are more sensitive to the model parameter at the lowest levels. Figure 1(a,b,c) shows the spectra of the vertical velocity calculated from the simulations using three different values of c. When c is too small, i.e., weak damping of the resolved scales, there is excessive energy at the high wave number end of the spectra, causing numerical instability of the simulations. On the other hand, within the range (0.1 < c < 0.5), an increase in c has little impact on the spectra, and gives a spectral roll-off at higher wave number, with a slope of about -2, which is similar to the spectrum calculated using the filtered experimental data (Fig 1(d)).

As discussed by Deardorff (1971) and Schmidt and Schumann (1989), grid-point values (in both experiments and numerical simulations) represent mean values over the grid interval. The spectra calculated here from such mean values have in effect been filtered. Thus, unless the grid is fine enough to truly resolve a significant portion of the inertial subrange, one should not expect to see a -5/3 slope (Kolmogorov's law) in the spectra, but rather, a steeper slope depending on the filter applied. Here c = 0.21, a value suggested by Deardorff (1971), was used for the reported simulations.

Note that theoretically a Lagrangian spectrum decays as k^{-2} (Tennekes and Lumley 1971) with wave number. However, this has no bearing on the -2 slope seen in Fig. 2(a), because the flow was simulated in a coordinate system moving with a constant translation velocity, and the individual fluid elements were not followed. This will be clear later in Section 5c, when the particle trajectories are presented.

It is obvious that our criterion for selecting the value of c is ad hoc. On the other hand, there is no "right" choice. Mason and Callan (1986) demonstrated that the length scale $l_0 = c\Delta\eta$ (where $\Delta\eta$ is the grid spacing) is the key parameter defining the separation into resolved and unresolved scales. Thus, the value of c not only relates to damping of the resolved turbulence, but also to the spatial resolution of the numerical simulation. We are not aware of any rigorous argument for the specification of c.

Here, fifteen experimentally observed plumes have been used as initial conditions for model simulations that advanced through three minutes of real time, i.e., fifteen three-minute flow realizations were constructed, which will be used in this study along with the experimental data.

3. Conditional Statistics of the Observed Plumes

Table 1 gives velocity and pressure statistics formed from the 15 experimentally observed plumes (the standard deviation of pressure fluctuation, σ_p, was calculated by the model). The statistics in Table 1 are <u>conditional</u> statistics, i.e., they are "in" the plumes, so they need not equal the usual unconditionally-averaged statistics. The model-calculated σ_p's are significantly larger (about a factor of 5) than those measured in a neutral atmospheric surface layer (Elliot 1972). This is consistent with the calculation by Wilczak and Businger (1984) who attributed the large pressure fluctuations to buoyancy contributions. The skewnesses of the vertical velocity and temperature at most levels are large and positive. The positive skewness of the

vertical velocity indicates an upward transport of vertical velocity variance by turbulent motion (Townsend 1976). This may be due to the fact that the turbulent kinetic energy production rate at the lower levels exceeds the local dissipation rate, and the excessive turbulent kinetic energy is driven upwards by the inertial force (Schmidt and Schumann 1989). The negative skewness of the horizontal velocity at the lower levels is believed to be caused by strong ejection motions (with $u < 0$ and $w > 0$). Notably, within the plumes the standard deviation of the cross-wind velocity, σ_v, is larger than that of alongwind wind velocity σ_u, except in the first two layers. This may correspond to the strong convergence in the cross-wind direction within plumes observed by Williams and Hacker (1992) from data obtained by an instrumented aircraft flying in the crosswind direction through the convective plumes. The correlation coefficients of the pressure and the alongwind velocity, $\overline{pu}/(\sigma_u \sigma_p)$ will be discussed in Section (5b) in terms of turbulent kinetic energy redistribution by the pressure fluctuations.

Table 1 may be compared with Table 2, where are listed statistics calculated (unconditionally) from the raw 1-hour experimental data. The statistics within the plumes follow qualitatively those calculated unconditionally, except that the large ratio of σ_v/σ_u at upper levels seen in Table 1 was "smeared" by the unconditional average. Values in Table 1 are smaller than those in Table 2, because of the filtering applied for the selected events (CHAPTER IV).

Figure 2(a) shows the conditional probability density function (PDF) P(w|In plume) of the vertical velocity, calculated using the observed plumes, at five levels. These PDF's are qualitatively similar

(at the same heights) to an unconditional PDF (Fig. 2(b)), calculated directly from experimental observations (Hunt et al. 1988). The skewed PDF means that updrafts are narrower than downdrafts. The shape of PDF in Fig. 2(a) implies that the unconditional PDF of vertical velocity is dominated by the influence of the large-scale plumes.

4. Momentum and Turbulent Kinetic Energy Budgets of the Plumes

Using aircraft measurements of velocity and temperature fluctuations at various heights within the atmospheric boundary layer, Lenschow and Stephens (1980) and Young (1988) evaluated many terms in the budget equations for the mean vertical velocity within conditionally sampled thermal updrafts and downdrafts. These studies demonstrated a quantitative difference between the force balances of updrafts and downdrafts. Acceleration in the updrafts was generally in phase with buoyant forcing, while the acceleration in downdrafts was generally out of phase with buoyant forcing. Therefore, it was suggested that the effects of pressure-gradients and mixing (which could not be separated in the analysis of experimental data) must be to provide the initial impetus to the downdrafts at higher levels. A similar study by Schumann and Moeng (1991), using Large Eddy Simulation, showed good agreement with the experimental study by Young (1988), and provided more detailed analysis of momentum budgets within the convective thermals. Schumann and Moeng also evaluated the turbulent kinetic energy budget for the thermals.

All these studies concerned primarily the force balance within the large-scale mixed layer thermals. Here, budgets of momentum and

turbulent kinetic energy within the atmospheric <u>surface layer plumes</u> are examined.

a. Momentum budgets

Following Young (1988), the momentum equations (CHAPTER IV, Eq. 16 (a,b)) can be averaged over updrafts and downdrafts, respectively. The resulting budget equations are

$$\frac{\partial [u]}{\partial t} = - [w]\frac{\partial \bar{\bar{U}}}{\partial z} - \frac{\partial [uw]}{\partial z} + \frac{\partial \overline{uw}}{\partial z} - \frac{1}{\rho_0}\frac{\partial [p']}{\partial x} + M_u \qquad (1a)$$

$$\frac{\partial [w]}{\partial t} = - \frac{\partial [w^2]}{\partial z} - \frac{1}{\rho_0}\frac{\partial \bar{p}_t}{\partial z} - \frac{1}{\rho_0}\frac{\partial [p']}{\partial z} + \frac{[\theta]}{\bar{T}}g + M_w \qquad (1b)$$

Here [ ] denotes an average over the updrafts or downdrafts, i.e.,

$$[q] = \frac{1}{XY}\int_{x-X/2}^{x+X/2}\int_{y-Y/2}^{y+Y/2} q(x,y)\ I(x,y)\ dxdy \ ,$$

where I is an indicator function

$$I = \begin{cases} 1 \text{ if point } (x,y) \text{ lies in updrafts (or downdrafts)} \\ 0 \text{ otherwise} \end{cases} .$$

Terms with the overbar are horizontally-averaged over both updrafts and downdrafts, and are invariant upon further averaging over updrafts or downdrafts; $\vec{p}_t$ is the "mean" pressure induced by the vertical advection in the convective atmosphere (Chapter IV); and p' is the pressure fluctuation, having vanishing mean when averaged over both updrafts and downdrafts. The mixing terms in the equation (M) are the sums of all the horizontal advection terms in the original momentum equations.

Note that, when moving the averaging operator inside the vertical derivatives, one has the relation (Leibnitz's rule) (Young 1988)

$$\left[\frac{\partial A}{\partial z}\right] = \frac{\partial [A]}{\partial z} + \frac{[A]}{\sigma}\frac{\partial \sigma}{\partial z} + \frac{[A]_B}{\sigma}\frac{\partial \sigma}{\partial z} , \qquad (2)$$

where σ is the number of gٰ points with $w > 0$ (or < 0) at height z, and $[\ ]_B$ denotes an average over lateral boundary of the updrafts or downdrafts. The last two terms account for the variation with height of the updrafts' or downdrafts' horizontal length, and are called size terms. Present calculation shows that σ changes very little with height for the surface layer plumes. Therefore the size terms have been neglected in Eq. (1). The subgrid terms were shown (through numerical calculations) to be at least a factor of five smaller than the rest of the terms in the equations, and have also been neglected.

Assuming a steady-state plume structure, i.e., $\partial [u]/\partial t \simeq 0$ and $\partial [w]/\partial t \simeq 0$, in a coordinate system moving with the translation velocity, the terms in these equations were evaluated using the fifteen experimentally-observed plumes (velocities and temperatures), and the corresponding model-calculated pressure fluctuations. The mixing terms were calculated as residuals. In order to compare this study with previous work, it was found convenient to normalize Eq. (1) by the convective scaling parameters: z_i, the mixed layer height[1] and $w_* = (z_i \overline{w\theta} g/\overline{T})^{1/3}$, the convective velocity scale.

Figure 3 presents the momentum budgets within updrafts (a,b) and downdrafts (c), respectively. The dominant feature of Fig. 3(a) is that within the updrafts, w-momentum generated by the "mean" pressure

---

1. Since z_i was not measured in the experiments, it was estimated indirectly to be 750 m, using the spectra of the vertical velocity suggested by Kaimal et al. (1982).

gradient forcing $\rho_0^{-1} \partial \bar{p}_t / \partial z$ and by buoyant forcing at the lower levels is advected upward by the mean vertical motion $(-\partial [w^2]/\partial z)$. This agrees with the study by Schumann and Moeng (1991). The buoyancy force and the fluctuating pressure gradient force are roughly in balance, and of secondary importance. As expected, the mixing for w momentum is small, since the w values on the interface between updrafts and downdrafts are small.

A study of pressure fluctuations by Moeng and Wyngaard (1986) based on Large Eddy Simulations found that about 40% of the variance of the pressure fluctuation in the convective atmosphere is contributed by buoyancy. In this study, it is difficult to separate the buoyancy contribution to the pressure fluctuations from other effects, such as mean shear, turbulence-turbulence interactions and subgrid motions (see Chapter IV, Eq. (27)), because all the effects are related. However, judging from the magnitude of σ_p (Table 1) and the balance between buoyancy and fluctuating pressure gradient in Fig. 3(a), one may suggest that the pressure fluctuations are primarily buoyancy generated. The sign of the fluctuating pressure gradient in Fig. 3(a) is opposite to that found by Schumann and Moeng (1991) in the lower levels of the mixed layer thermals. This discrepancy may be attributed to the stronger wind shear effect in the large-scale mixed layer thermals, which induces a negative vertical pressure gradient (shown later) supporting the vertical motion.

In the alongwind momentum budget (Fig 3(b)), consistent with previous studies (Wilczak and Businger 1984; Schols and Wartena 1986; Schumann and Moeng 1991), within the updrafts there is a favourable horizontal pressure gradient force $(\partial [p']/\partial x < 0)$. The term $-[w]\partial U/\partial z$,

representing upward advection of slow alongwind motion (or horizontal momentum deficit), is a significant loss of u momentum at low levels. By contrast, in the downdraft region (Fig 3(c)) $-[w]\partial\overline{U}/\partial z$ represents a downward transport of the horizontal momentum surplus, and is the largest source of the horizontal momentum, essentially balanced by a positive horizontal pressure gradient force. The flux divergence ($-\partial[uw]/\partial z$) works in the same direction in both updrafts and downdrafts to balance the horizontal-average mean flux divergence. The effect of mixing shown in Fig 3(b,c), resulting from large-scale circulations within the plumes, is to export horizontal momentum from downdrafts to updrafts to recover the u-momentum lost by the upward advection ($-[w]\partial\overline{U}/\partial z$). A similar mixing effect for u momentum in the bottom layers of mixed layer thermals has been found by Schumann and Moeng (1991).

The momentum budgets discussed above can be interpreted with the help of a conceptual model of a plume moving in a sheared atmosphere (Fig. 4). Figure 4 is similar to the model Newton (1966) used to describe thunderstorm dynamics. In this scheme, a plume moves at a constant translation velocity (U_t) which is faster than the air velocity ($U_e(z)$) at lower levels, but slower than the air velocity at upper levels. It can be considered as an obstacle immersed in the air flow. Then, because of the velocity difference between the plume and its environment, at upper levels a positive pressure perturbation is induced on the upwind side and a negative pressure on the downwind side; at low levels the reverse pressure distribution occurs. The net effect of these horizontal pressure gradients is to decelerate the moving structure (considered in bulk) at lower levels and accelerate it at upper levels: thus to "tip" the plume. However, because of the

vertical shear of the horizontal wind, vertical motion within the updraft continues to transfer air having lower alongwind momentum from lower levels to the upper levels ($-[w]\partial\overline{U}/\partial z$), and this mechanism opposes the tipping force due to the horizontal pressure gradients. Therefore, to maintain the plume there must be strong vertical motion supported by either a favourable vertical pressure gradient ("mean" + fluctuation) or/and buoyancy, as seen in Fig. 3(a). Since the translation velocity for our observed plumes is close to the mean velocity at the top level (150 m), only the lower half of the model in Fig. 4 seems to apply to our experimental observations. The force balances shown in Fig. 3 are consistent with the shape-preservation of the convective plumes.

b. Turbulent kinetic energy budget

For convective plumes to survive in a highly dissipative atmospheric turbulent flow, there must be a consistent and efficient energy supply mechanism. This may be seen by examining the budget of turbulent kinetic energy within the plumes.

In an analysis of turbulent kinetic energy budget within updrafts of large-scale mixed-layer thermals, Schumann and Moeng (1991) found that the essential sources for the total turbulent kinetic energy ($e = 1/2\sqrt{u^2+v^2+w^2}$) are buoyancy production and turbulent mixing from downdrafts into updrafts in the lower part of the mixed-layer thermal. But the pressure transport was found to be insignificant even in the atmospheric surface layer. This seems to contradict what has been seen of the role of pressure forcing in maintaining the plumes (Section 4a).

In this study, the budgets for individual components of the turbulent kinetic energy ($\overline{u^2}$, $\overline{v^2}$, $\overline{w^2}$) will be discussed, emphasizing the vertical component within updrafts. It is felt that turbulent kinetic energy interchange between different velocity components may also be of importance in describing the development of the plumes.

The ensemble-averaged turbulent kinetic energy budget for the vertical wind component within the updrafts can be written as

$$\frac{1}{2}\frac{\partial[w^2]}{\partial t} = -\frac{1}{2}\frac{\partial[ww^2]}{\partial z} - \frac{[w]}{\rho_0}\frac{\partial\overline{p}_t}{\partial z} + \frac{[w\theta]}{\overline{T}}g - \frac{1}{\rho_0}\frac{\partial[vp']}{\partial z} + \frac{1}{\rho_0}[p']\frac{\partial[w]}{\partial z} - \varepsilon_w + M_{\bullet w} \quad (3)$$

Here, as in the momentum budgets, the size and subgrid terms are small, and have been neglected. Note that the term $-\rho_0^{-1}[w]\partial\overline{p}_t/\partial z$ would be identically zero if the budget equation were to be averaged over both updrafts and downdrafts. This term was missing in Schumann and Moeng's (1991) study.

Terms in Eq. (3) were evaluated using the experimental data and the simulated pressure fluctuations, with the mixing term calculated as the residual. The dissipation rate ε_w has been suggested and observed to be larger within updrafts than in downdrafts because of the more vigorous turbulent motions (Mahrt 1991; Schumann and Moeng 1991). However, since the details of the energy cascade mechanism are not known, as a first approximation, ε_w was evaluated as $\varepsilon/3$, where ε is total dissipation rate estimated using velocity spectra (Fig. 5). We assumed valid the inertial subrange relationship

$$fS_{ww}(f) = \alpha_w \varepsilon^{2/3}(2\pi f/\overline{U})^{-2/3} \quad (4)$$

where S_{ww} is the spectrum of the vertical velocity, f is frequency and $\alpha_w = 0.67$.

Assuming steady state, i.e., $\partial[w^2]/\partial t = 0$, the rest of the terms in Eq. (3) are depicted in Fig. (6). The local energy sources (the buoyancy force and the vertical velocity-"mean" vertical pressure gradient interaction term) generate excessive turbulent kinetic energy in the vertical motions at low levels. However, the local dissipation is relatively small. This imbalance drives a great upward (probably overshot when the inertial force is great) turbulent transport ($-1/2\partial[w^3]/\partial z$), and the redistribution of a large amount of the vertical component of the turbulent kinetic energy by pressure fluctuations into the horizontal components ($1/\rho_0[p']\partial[w]/\partial z$). The pressure fluctuations also transport some overshot vertical component of the turbulent kinetic energy from upper levels back to lower levels to recover the lost energy. Thus, they are a source at the lower levels and a sink at upper levels. The mixing term (calculated as the imbalance Eq. (3)) in Fig. 6 may be subject to error due to the assumption of steady-state and the summation of errors of other terms. No satisfactory explanation has been found for the mixing term, which, nevertheless, is not essential for the following discussions.

Figure 7 presents the vertical profiles of the pressure velocity-gradient covariances, $[p]\partial[u]/\partial x$, $[p]\partial[v]/\partial y$, $[p]\partial[w]/\partial z$, which quantify the pressure redistribution of the alongwind, crosswind and vertical components of the turbulent kinetic energy, respectively. The crosswind pressure redistribution term $[p]\partial[v]/\partial y$ was inferred from $[p]\partial[u]/\partial x$ and $[p]\partial[w]/\partial z$ through the continuity equation. A positive value of the covariance means that the corresponding component of the turbulent kinetic energy gains energy from other components, while a negative covariance means that the corresponding component of turbulent

kinetic energy loses energy to other components, by pressure fluctuations. At lower levels, pressure fluctuations redistribute a large amount of vertical component of the turbulent kinetic energy into the cross-wind component, but they have no impact on the alongwind component. At upper levels, pressure fluctuations pass turbulent kinetic energy from the cross-wind component into the alongwind component, leaving the vertical component untouched. Thus, as far as pressure redistribution is concerned, it seems that the alongwind velocity [u] and vertical velocity [w] are essentially decoupled at all levels.

Since working by the pressure force transfer energy between the different velocity components of equal wave numbers (Batchelor 1970, p87), no energy is generated or destroyed during the pressure redistribution.

McBean and Elliott (1978) studied the transfer of turbulent kinetic energy by the pressure fluctuations, and showed that the most efficient energy transfer between velocity [u] and other velocity components takes place when [u] and [p] are 90° out of phase, while no transfer takes place when [u] and [p] are in phase. Hence based on Fig. 7, one may suggest that the horizontal velocity and the pressure fluctuations have small phase difference at lower levels within the updrafts, leading to weak conversion of turbulent kinetic energy from w to u. This is consistent with the small phase difference and large correlation between u and p at lower levels seen in Table 1.

It is noted that both momentum and turbulent kinetic energy budgets in this study differ quantitatively from the study by Schumann and Moeng (1991). The values in Fig. 3 and Fig. 6 are generally a

factor of two larger than corresponding values for the atmospheric surface layer calculated by Schumann and Moeng (1991). This may be due to the fact that Schumann and Moeng used data from a Large-Eddy Simulation where the flow had reached a steady state in equilibrium with a constant imposed surface heat flux, while the data in this study was collected between 10 to 11 am when the atmospheric boundary layer was in the stage of rapid development (deepening). In addition, pressure transport $(-1/\rho_0 \partial[p'w]/\partial z)$ is more important here than in Schumann and Moeng's study.

5 A Case Study of An Evolving Plume

Some insights into flow within a plume, such as the role of pressure distributions within the plume and the effect of the plume translation velocity on the evolution of the plume, can be developed more clearly in case studies, using the simulated flow realizations.

a. A snapshot of a convective plume

Figure 8 shows contour plots (a snapshot in time) of various flow variables, from one of the 15 experimentally observed plumes in the Boulder data. Figure 8 resembles the averaged large-scale plume of Wilczak (1984) in a convective atmospheric surface layer. The plume is inclined slightly away from the vertical, as can be seen from both velocity and temperature contours (Fig. 8(b) and (c)). The velocity field is characterized by a strong narrow updraft, with wider downdrafts on both sides (Fig. 8(a)). Probably still in its early development, the plume does not show a strong microfront on the upwind

side of the updraft, as has been seen in other experiments (e.g., Kaimal and Businger 1970; Wilczak 1984). The alongwind velocity fluctuation u (Fig. 8(d)) correlates well with the vertical velocity w in the updraft region, and has a large negative value in front of the updraft. The vertical velocity and temperature θ are strongly positively correlated essentially everywhere. The phase relation between u and w creates strong downward momentum transport within the updraft (which is in fact an upward transport of u momentum deficit), but upward momentum transport just in front of the updraft (Fig. 8(e)). This is similar to the uw distribution observed by Wilczak (1984), who concluded that this sort of plume is inherently ineffective in transferring streamwise momentum. Consistent down-gradient heat transport occurred throughout the plume (Fig. 8(f)), as a result of the good correlation between w and θ.

Unless otherwise stated, the following discussion will be based on the plume shown in its initial state in Fig. 8, and its evolution with time.

b. Pressure distributions within the plume

The pressure fluctuation field in Fig. 9, calculated using the observed velocities and temperature (Fig 8), shows negative values within the strong updraft (warm) region, and distinct alongwind and vertical gradients both upwind and downwind of the updraft.

The pressure fluctuations in this particular plume are produced mostly by the interaction between the updraft and the wind shear. This can be shown by a linear analysis of the Poisson equation (Chapter IV,

Eq. (28)) (Rotunno and Klemp 1982). Keeping only the wind shear term in the Poisson equation, one obtains

$$\frac{\partial^2 p}{\partial x^2} + \frac{\partial^2 p}{\partial^2 z} \simeq -2\rho_0 \frac{\partial U}{\partial z} \frac{\partial w}{\partial x} \tag{5}$$

Fig. 8(b) shows that in a gross sense w varies sinuoidally with x in the region on the downwind side, of the updraft. Note that for a function consisting of a narrow range of Fourier components, the Laplacian of the function is negatively proportional to itself. Neglecting the variation of p with z, and assuming $\partial U/\partial z$ does not change much in that region, the variation of p with x can therefore be approximated (very schematically) by

$$p \propto 2\rho_0 \frac{\partial U}{\partial z} \frac{\partial w}{\partial x} \tag{6}$$

in the neighbourhood of the downwind side of the updraft. Comparing Fig. 8(b) and Fig. 9, we can see that the sign of the pressure fluctuation varies roughly according to that of $\partial w/\partial x$, although the maximum magnitude of the pressure fluctuation occurs somewhat away from the location predicted by Eq. (6). Since the magnitude of $\partial w/\partial x$ increases with height to about 90 m, then decreases with height, in the downwind region, the wind shear induced vertical pressure gradient accelerates the updraft below 90 m, but decelerates it above, in the downwind region.

Figure 10 shows the model-calculated acceleration field, and the associated vertical pressure gradient ("mean" + fluctuation) and buoyancy fields of the plume. Comparing the patterns and the contour values in Fig. 10, it is obvious that the acceleration correlates well with the pressure gradient, and the buoyancy force influences strongly

the acceleration only at upper levels within the updraft. The contribution from the subgrid terms in the vertical momentum equation is apparently very small.

Largely due to the pressure gradient forcing, the air within the updraft experiences an upward acceleration at lower levels ($z < 90$ m), and a downward acceleration at the upper levels. When advected downstream, such a pressure field will continuously initiate the rising of hot fresh air from the surface into the updraft, to provide energy for the development of the plume. Thus, it seems reasonable to suggest that although buoyancy may be the primary force in initializing the plume, the vertical pressure gradient dominates the evolution of the established plume. The importance of the pressure distribution within a surface plume has been noted by Kaimal and Businger (1970) who, by calculating the vertical acceleration and buoyancy force from an experimental observation, concluded that the vertical pressure gradient must be larger than the hydrostatic pressure gradient, and must account for at least 40% of the vertical acceleration. Similarly, Schols and Wartena (1986) showed that the vertical pressure gradient force within coherent structures, observed in the first few meters above the ground, is sufficiently large to cause ejection of the low-speed flow from the bottom to the top of the structures.

c. The role of translation velocity in the development of the plume

In a sheared atmosphere, the plume experiences considerable mixing due to the relative motion between the plume and its environment. On the one hand, since the mixed air is cooler than the air in the updraft region of the plume (Fig. 8(a),(c)), an increase of U_t will bring more

cooler air into the updraft from the lateral boundaries of the updraft, reducing the upward motion; on the other hand, at a large U_t, there will be more hot air entering the updraft from the bottom of the plume per unit time. A theoretical model of plume mixing developed by Davison (1974) showed that in most cases, heat entering from the bottom of a plume exceeds that lost through its lateral boundaries. Thus a large U_t favours the vertical motion within the updraft.

However, for the horizontal motions, a larger U_t will increase the mixing of the negative alongwind momentum from the downwind side of the updraft. This can be seen by evaluating the horizontal momentum budget as in Fig. 3(b) but using a larger translation velocity. Figure 11 shows that, with a larger translation velocity $U_t = 1.1\ U_m$, the mixing effect changes from a positive production seen in Fig. 3(b) to a negative production for the horizontal momentum. Thus, unless there is a stronger vertical advection of the horizontal velocity, the increased ingestion of negative horizontal momentum will destroy the shape of the updraft. This is seen in Fig. 12 which shows two plume structures after one minute of evolution from the same initial condition (Fig. 8(a)), but using two different translation velocities. With a translation velocity $U_t = 0.9\ U_m$, little change (compared with Fig. 8(a)) was found in the plume's shape and strength after one minute, but when the plume is advected at a higher translation velocity $U_t = 1.1\ U_m$, the updraft becomes narrower and weaker. This shape-destroying mechanism due to a large U_t is consistent with the "tip" mechanism resulting from horizontal pressure gradient discussed earlier (section 4a).

Therefore, for a certain thermal stability condition, there is an optimal translation velocity which sustains a plume by balancing the horizontal and vertical motion. For the plume shown in Fig. 8(a), it was found that a U_t equal to 90% of the local velocity at 150 m can sustain it for the longest time (~ 3 min).

The translation velocity of a plume depends not only on the flow mean velocity, but also on the momentum mixing both horizontally and vertically within the plume, which varies with surface heating. This may lead to some reported variations in plume translation velocity in different studies (Kaimal and Businger 1970; Wilczak and Businger 1984; Schols et al. 1985).

In passing, it is noted that, in contrast to a plume in the convective atmosphere, under neutral and stable conditions, without surface heating (weak vertical motion), a coherent structure such as those observed by Schols (1986), can be destroyed readily by the horizontal pressure gradient induced by the relative motion between the coherent structure and its environment. In fact, when visually screening the Boulder data of neutral and stable conditions, no evidence of organized motion having persistent spatial (vertical) and temporal extent was found.

d. Trajectories of fluid elements within the plume

A plume moving at a constant translation velocity means that the flow structure (e.g., the pressure and velocity patterns) is advected at a constant velocity towards the downstream region. In this aspect, a plume is somewhat like a wave disturbance with U_t as the phase speed. During its development, a plume is maintained by continually injecting

fresh hot air into the updraft and getting rid of the relatively cold fluid elements (Davison 1974; Telford 1986). Therefore, not all air elements initially within the plume will stay with the plume during its lifetime. To visualize the motion within the convective plume, Fig. 13 presents ten particle trajectories viewed in the coordinate system moving at the constant translation velocity. The particle trajectories were calculated using the three-minute numerical simulation for the plume. Initially (t = 0), the ten fluid elements were distributed symmetrically with respect to the centre of the updraft. At each time step (Δt = 1 s), the simulated velocity field at the grid points (with interpolations when necessary) were used to advance the particles. After two minutes, all ten fluid elements have moved to new positions, and few stayed within the domain of the calculation. It is noted that the motion of the particles entering into the updraft is essentially deterministic rather than random.

6. Conclusion and discussion

A striking feature of the momentum and turbulent kinetic energy (w^2) budgets evaluated within the updrafts of the plumes is that, the local source (buoyancy) and sink (viscous dissipation) are relatively small compared with vertical advection and transport by turbulence and pressure. This implies that within a convective plume, most momentum and turbulent kinetic energy are not generated locally, rather they are transported from other parts of the flow. In other words, the local turbulent quantities bear little relation to the local mean flow properties. This is in contrast with turbulence under neutral

stratification where the flow structures are dominated by a close balance between shear production ($\mathcal{P}$) and viscous dissipation (ε).

As expected, the persistent and coherent pressure force has a significant influence on the dynamics and energetics of the convective plumes by redistributing turbulent kinetic energy among the velocity components. Although the pressure fluctuation has the tendency to redistribute turbulent kinetic energy among velocity components, it was demonstrated that due to the particular phase relationships between the velocities and pressure fluctuations within the convective plumes, the energy redistribution is very uneven, and it is especially ineffective in that respect for energy exchange between alongwind and vertical motions within a convective plume. This means the return-to-isotropy time scale, τ (time required for a velocity component to return to an isotropic state by nonlinear turbulence interactions), is large for a flow dominated by such plumes, and different for the different velocity components.

The decoupling between u and w results in ineffective alongwind momentum transport in a convective atmosphere, which explains previous experimental observations. McBean (1974) observed that although strong surface heating leads to large amounts of momentum transfer both upward and downward, the net transfer is usually very small. Greenhut and Khalsa (1982) showed that the large upward and downward momentum transfer under convective atmosphere is produced almost entirely by the plume-averaged mean flow circulations within updrafts and downdrafts, with only 5% coming from small-scale eddy correlations. Mahrt (1991) suggested that the ineffective momentum transport is a result of a phase shift between the alongwind and vertical velocities. The

stronger the updraft, the weaker the correlation between u and v will be. Consequently, the momentum transport $(-\overline{uw})$ decreases with increasing thermal instability. This systematic phase-lag between alongwind and vertical velocities in convective atmospheric turbulence was pointed out earlier by Tennekes and Lumley (1971).

The distinctive pressure distribution within a convective plume shown in the case study, and its role in transferring turbulent kinetic energy among velocity components, have important implications for modelling convective atmospheric turbulence. For example, it has been realized by atmospheric turbulence modellers that the second-order parameterization of pressure covariance terms using Rotta's (1951) model must be modified to include the contribution from convectively-induced pressure fluctuations (Wyngaard 1980; Zeman 1981; Moeng and Wyngaard, 1986). The variation of velocities and pressure distributions within the plumes with atmospheric stability conditions almost assures that ad hoc adjustments of second-order closures are necessary in modelling atmospheric turbulence (Wyngaard, 1982).

The occurrence of convective plumes and their transport properties pose a difficult problem for air quality modelling. The longevity of the highly anisotropic convective plumes makes it possible for a diffusing pollutant to travel a long distance upward without reversing downward, as seen in Fig. 13. This violates the principle of the K-theory of turbulence diffusion, in which diffusion is envisaged as a random walk process in which particles can travel large distances only after suffering many independent upward and downward displacements (Lamb 1982). Second-order closure models are also likely to yield erroneous predictions of pollutant concentrations in the convective

atmospheric surface layer, because of the difficulties in modelling the covariance of pressure gradient and scalar concentration, $1/\rho_0 \overline{c \partial p/\partial z}$ (Zeman 1981), to which the plumes make important contributions (Moeng and Wyngaard 1986). In situations where pollutants are released into a flow dominated by convective plumes, or in the case of a puff release, the transport properties of convective plumes can be most important. In such cases, recall that the covariance of pressure gradient and concentration is parameterized (in the budget equation for the vertical flux, $\overline{wc}$) as $\overline{wc}/\tau$ (Zeman 1981). Then because of the large return-to-isotropy time scale, τ, of the plumes, it will take a long time for a mass flux to be destroyed within the plumes. Thus, the concentration field would likely contain some extreme "events" and counter gradient fluxes may occur due to the existence of the plumes, and a large sampling variation can be expected in experimental data. These extreme "events" are one of the causes of the variability of observed concentration (mean and fluctuation) in air quality experiments.

So far, no practical dispersion model reported has explicitly incorporated convective plumes in calculating atmospheric dispersion, an essential step to understand and provide a practical solution for the inherent uncertainty in air quality modelling. Nevertheless, I feel that the present study has qualified some aspects of plumes in the convective atmospheric surface layer that are important for atmospheric dispersion. The more we understand the coherent dynamics, the easier it will be to incorporate them into a practical dispersion model. A future extension of this work would be to characterize plumes under different atmospheric stability conditions, so that uncertainty in air

quality modelling can be estimated using the extreme "events" resulting from plumes under different stability conditions.

Acknowledgements

Table 1 Conditional statistics (statistics "in" the raw ensemble plumes)

Height (m)	σ_u (m/s)	σ_v (m/s)	σ_w (m/s)	σ_p (Pa)	Sk_u	Sk_w	Sk_θ	$\dfrac{\overline{up}}{\sigma_u \sigma_p}$ *
150	0.84	1.11	0.86	3.52	0.06	0.32	0.61	0.11(84°)
130	0.84	1.09	0.89	3.31	0.28	0.22	0.51	0.12(83°)
110	0.94	1.13	0.92	3.16	0.25	0.21	0.47	0.12(83°)
90	0.95	1.08	0.87	3.06	0.20	0.22	0.47	0.19(79°)
70	0.93	1.08	0.81	2.96	0.15	0.27	0.43	0.28(74°)
50	0.98	1.16	0.75	2.84	-0.04	0.21	0.50	0.36(69°)
30	1.03	1.02	0.56	2.74	-0.30	0.11	0.51	0.51(59°)
10	1.20	0.98	0.30	2.68	-0.21	0.04	0.25	0.66(49°)
Ave	0.96	1.08	0.75	3.03	0.05	0.19	0.47	0.30(72°)

*The numbers in the bracket are phase difference θ, between u and p, which are calculated by

$$\theta = \cos^{-1}\left\{ \frac{1}{2\pi} \int_0^{2\pi} \frac{up}{\sigma_u \sigma_p} \, dx \right\},$$

assuming $p \propto \sin(x)$ and $u \propto \sin(x+\theta)$.

Table 2 Unconditional statistics calculated from the 1-hour experimental observation

Height (m)	σ_u (m/s)	σ_v (m/s)	σ_w (m/s)	Sk_u	Sk_w	Sk_θ	Monin-Obukhov length (m)
150	1.47	1.18	1.23	-0.03	0.51	0.69	-17
100	1.51	1.15	1.19	0.02	0.69	0.66	-35
50	1.63	1.13	1.05	-0.18	0.71	0.79	-62
22	1.75	1.13	0.78	-0.07	0.53	0.76	-31
10	1.84	1.20	0.60	-0.11	0.17	0.53	-39
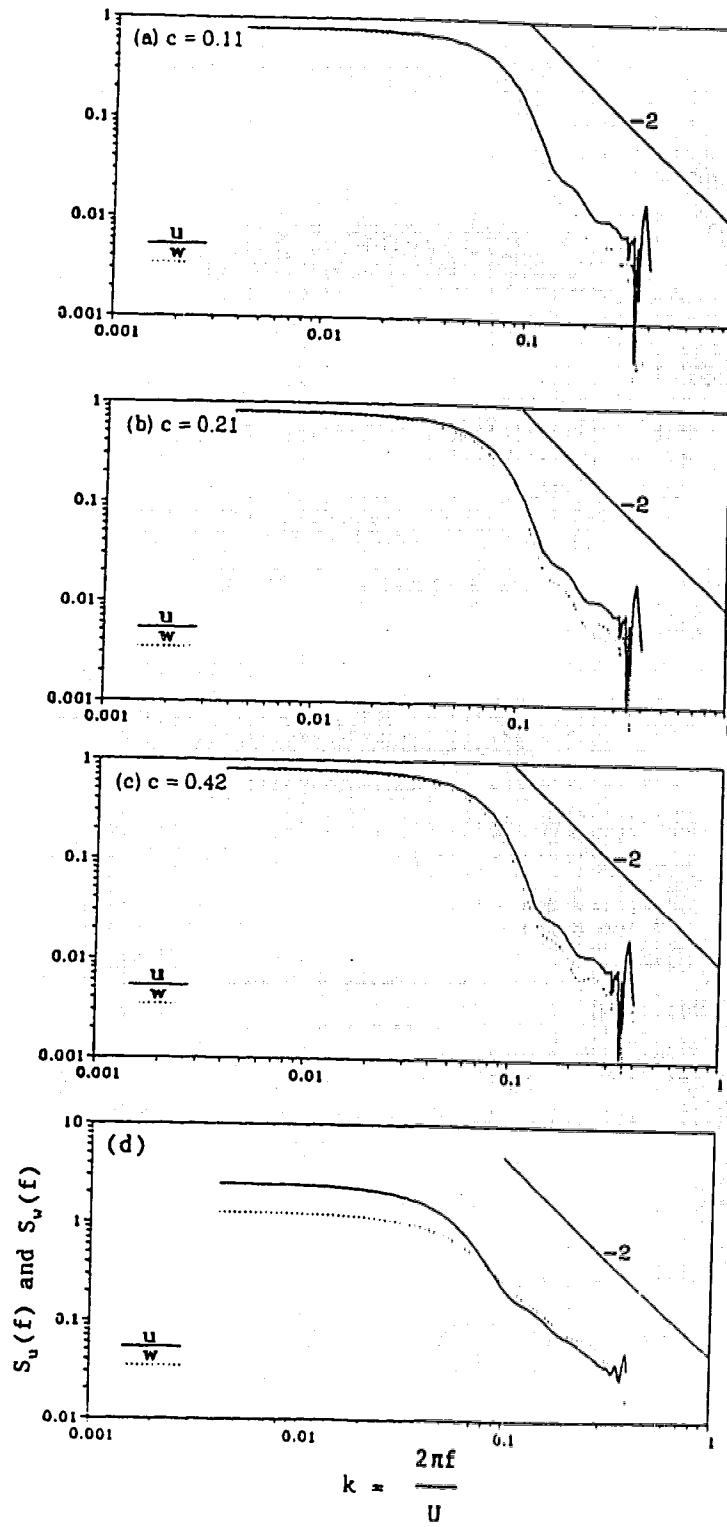
Fig. 1 Velocity spectra calculated (a,b,c) from the numerical simulations with different model parameters c, and (d) from the filtered experimental data, at a height of 30 m. Here f is frequency, k, wave number and U, the mean wind speed at 30 m.
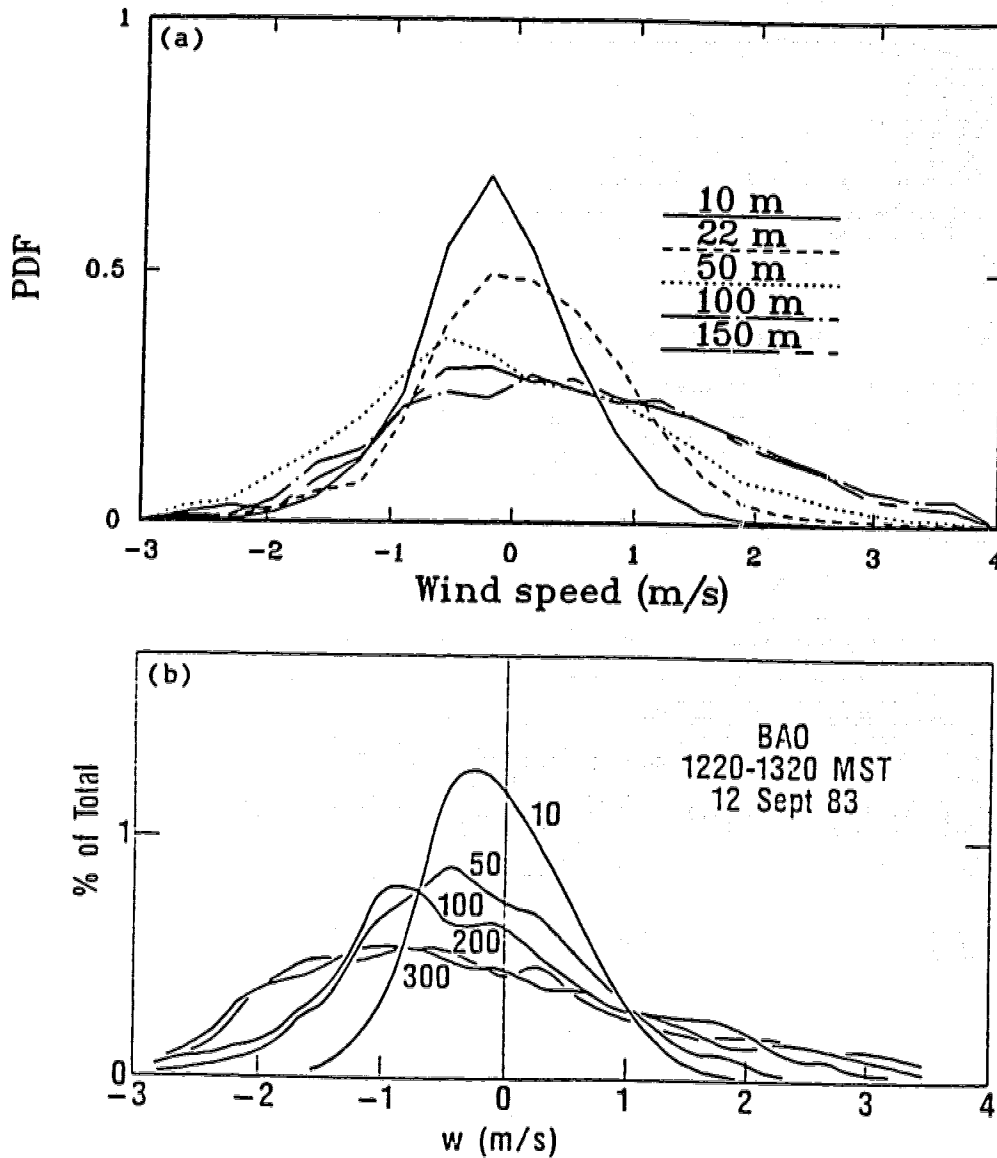
Fig. 2 Probability density functions calculated (a) using the conditional sampled convective plumes in this study, and (b) from raw experimental data by Hunt et al. (1988).
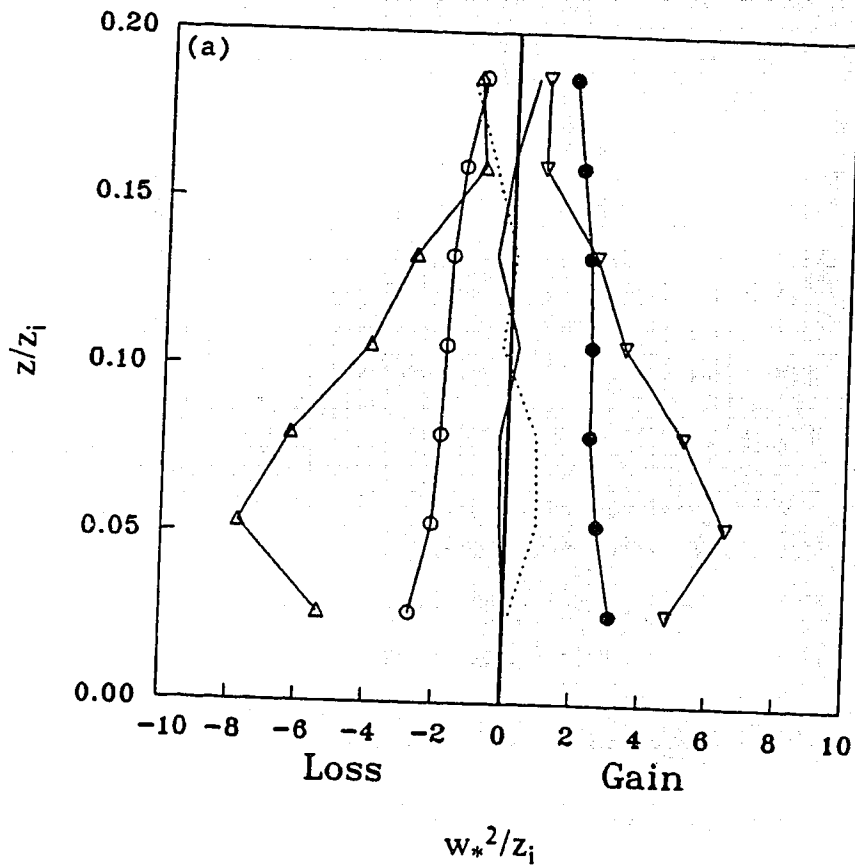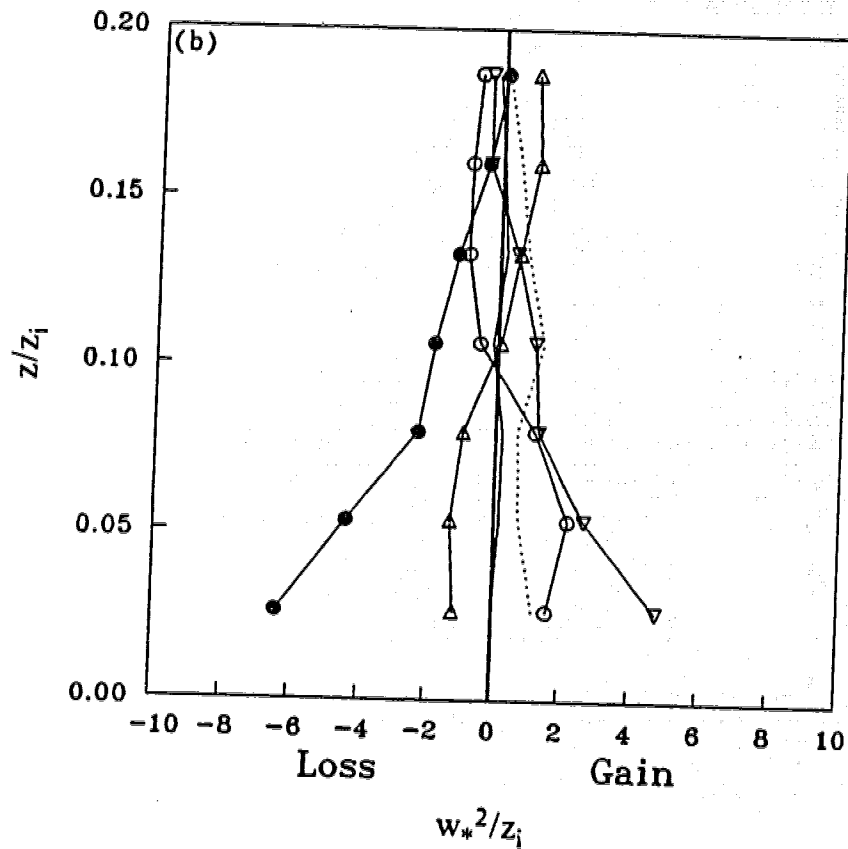
Fig. 3(a) Vertical momentum budget within the updrafts of the convective plumes observed experimentally. A translation velocity $U_t = 0.9 \, U_m$ was used in the calculation, where U_m is the local mean velocity at 150 m.

● $[\theta]g/T$, ○ $-1/\rho_0 \, \partial[p']/\partial z$, △ $-\partial[w^2]/\partial z$, ▽ $-1/\rho_0 \, \partial\bar{p}_t/\partial z$, —— size terms, ... mixing terms.

Fig. 3(b) Horizontal momentum budget within the updrafts of the convective plumes observed experimentally. A translation velocity $U_t = 0.9\ U_m$ was used in the calculation, where U_m is the local mean velocity at 150 m.

● $-[w]\partial U/\partial z$ o $-\partial[uw]/\partial z$, Δ $\partial\overline{uw}/\partial z$, ∇ $-\partial[p']/\partial x$,
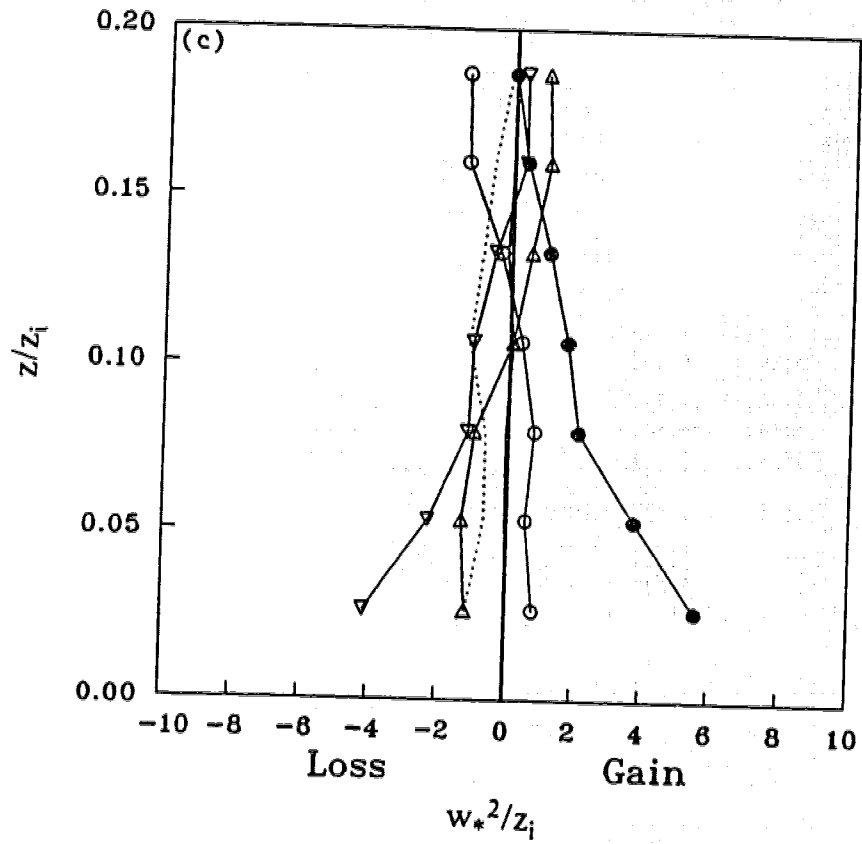
———— size terms, ... mixing terms.
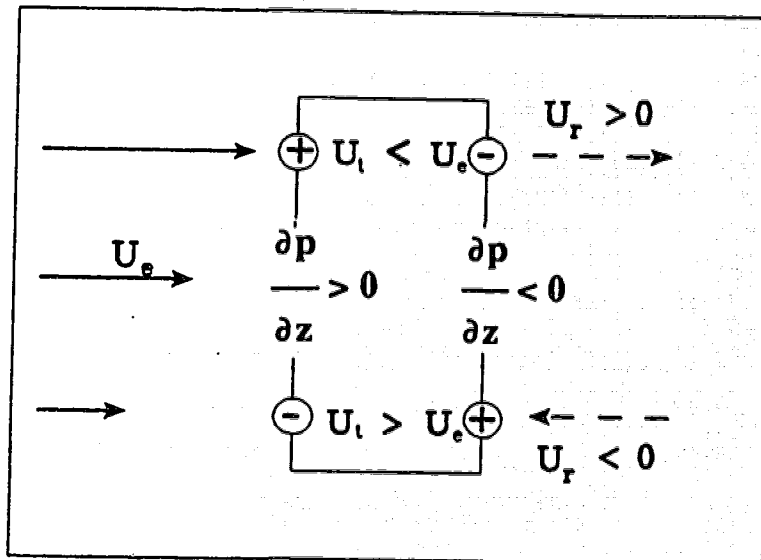
Fig. 3(c) As in Fig. 3(b), except for the downdrafts.

Fig. 4 Schematic representation of a convective plume as an obstacle in air flow with wind shear. $U_r = U_e - U_t$, where U_t is the translational velocity of the CS and $U_e(z)$ the wind velocity of the environment. The plus and minus signs denote the induced pressure, p, due to the relative motions.
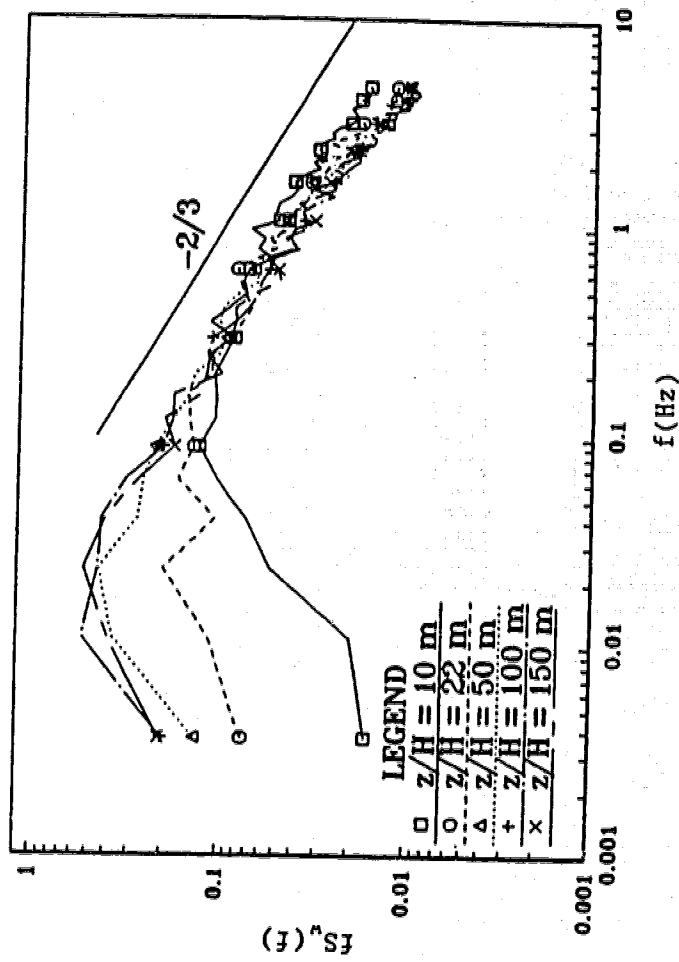
Fig. 5 Vertical velocity spectra at five heights calculated using the 1-hour raw experimental record.
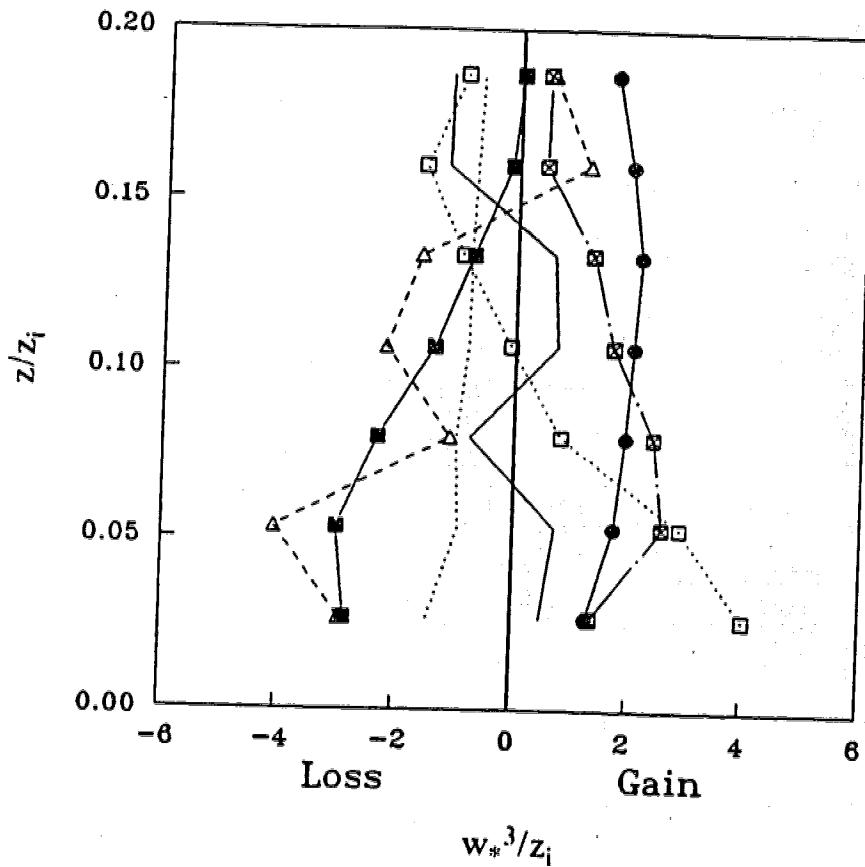
Fig. 6 Budget of vertical component of the turbulent kinetic energy within the updrafts of the convective plumes observed experimentally. A translation velocity $U_t = 0.9\, U_m$ was used in the calculation, where U_m is the local mean velocity at 150 m.
● $[w\theta]g/T$, ⊠ $-1/\rho_0[w]\partial p_t/\partial z$, ⊡ $-1/\rho_0\partial[wp']/\partial z$, △ $-\partial[ww^2]/\partial z$, ■ $1/\rho_0[p']\partial[w]/\partial z$, —— mixing terms, ... dissipation.
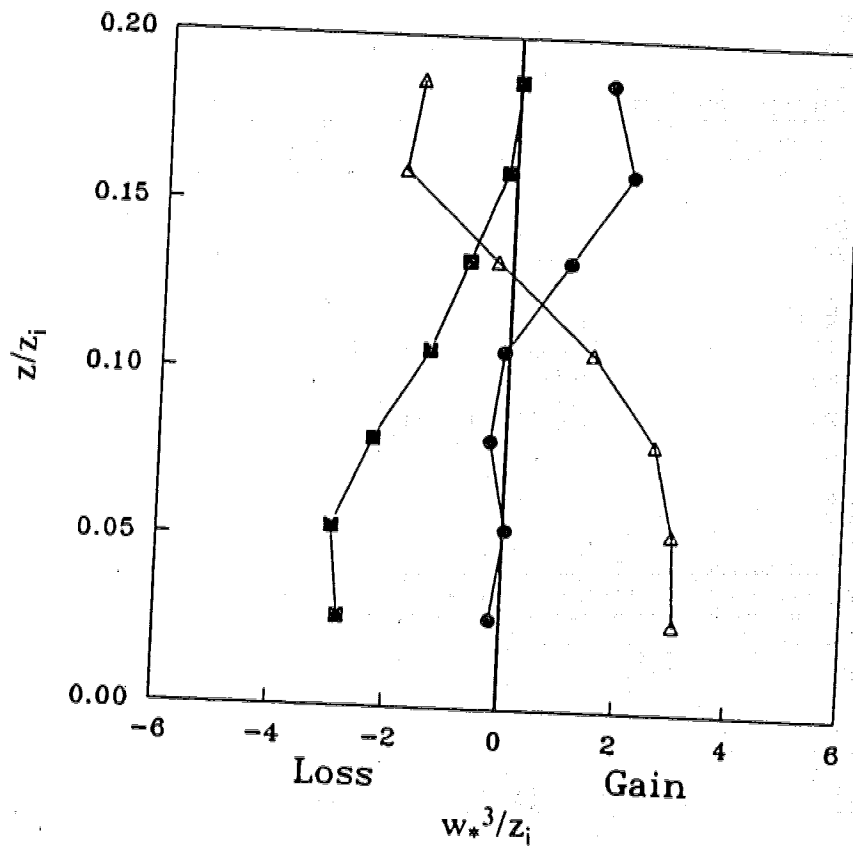
Fig. 7 Pressure redistribution of turbulent kinetic energy between velocity components.
● $1/\rho_0 [p] \partial [u]/\partial x$, △ $1/\rho_0 [p] \partial [v]/\partial y$, ■ $1/\rho_0 [p] \partial [w]/\partial z$.
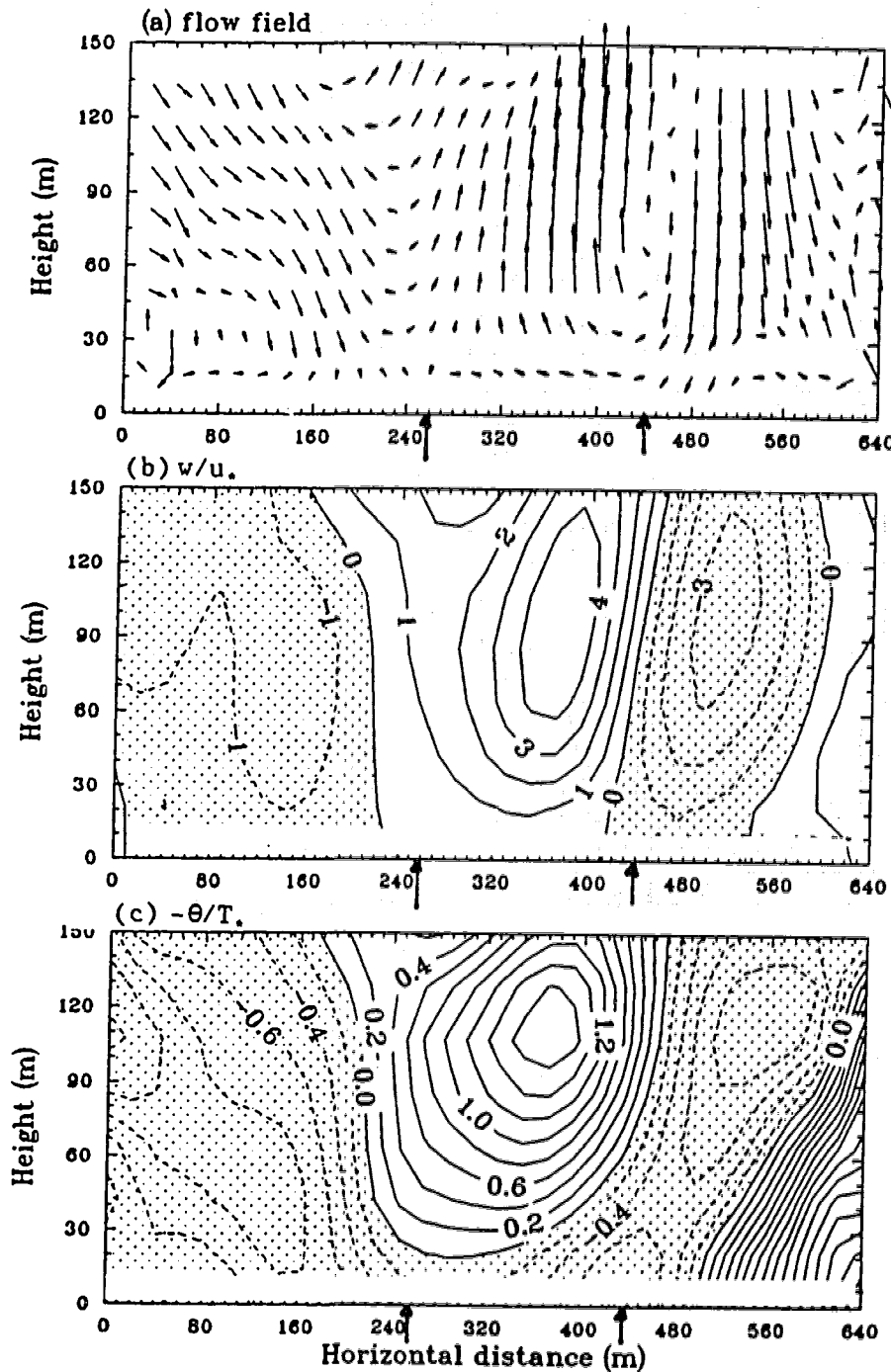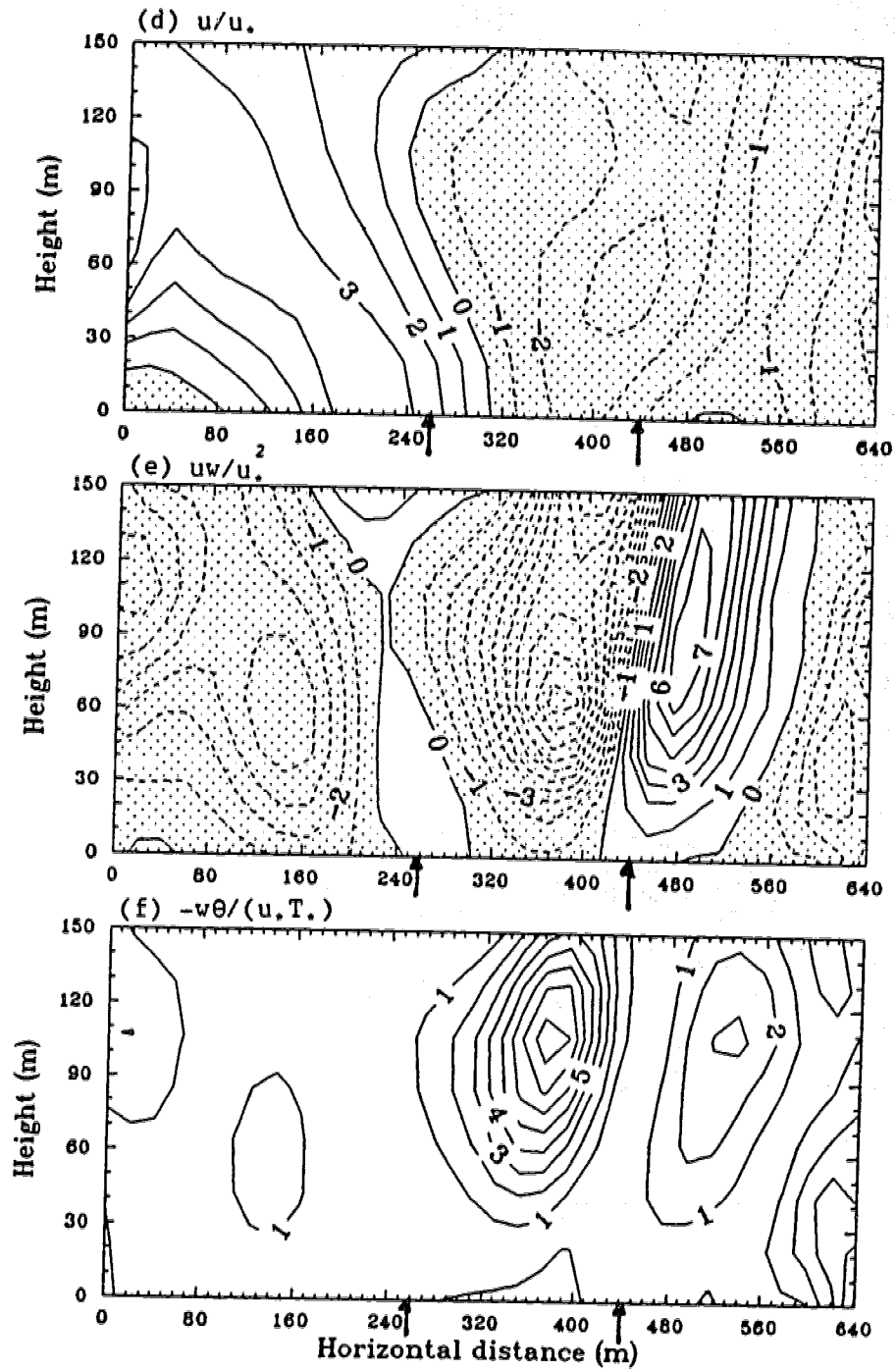
Fig. 8 A snap shot of vertical cross sections of flow variables of a observed convective plume in the atmospheric surface layer. In (a), the unit is arbitrary. The variables in (b) - (f) are normalized by u.(0.46 m·s⁻¹) and T.(-0.43°C). Negative values are shaded. The updraft of the convective plume is indicated by the length between the two arrows.

(d) u/u$_*$

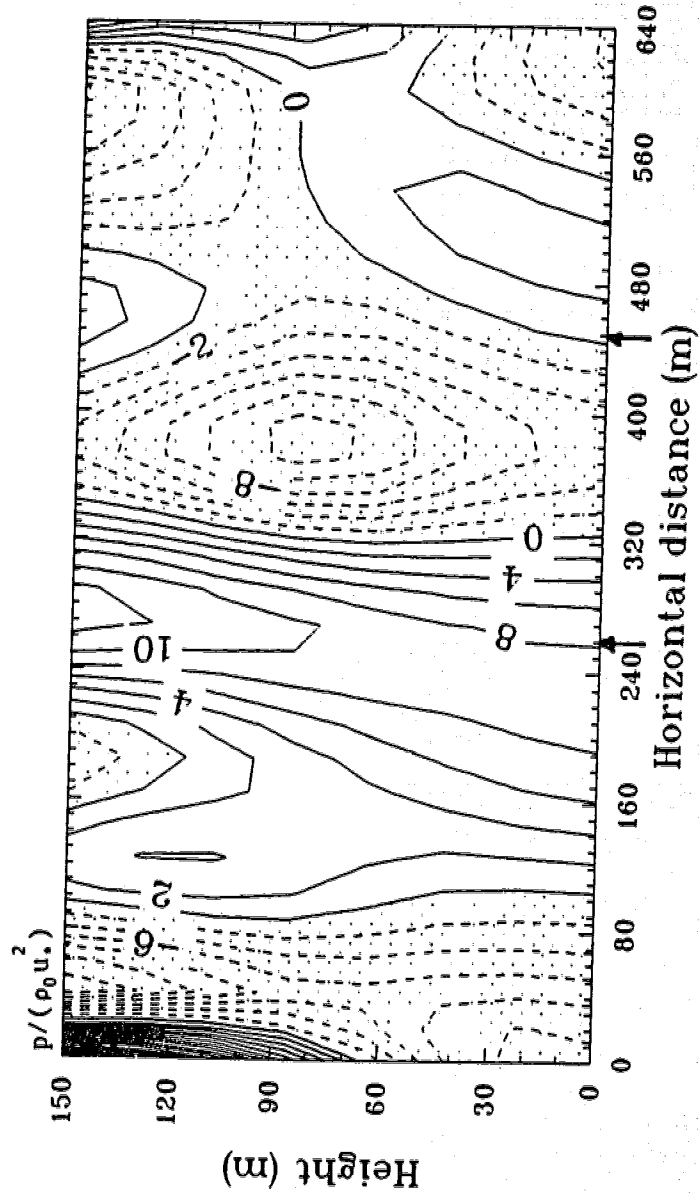(e) uw/u$_*^2$

(f) $-w\theta/(u_*T_*)$

Horizontal distance (m)

Fig. 9 The pressure fluctuation within the convective plume (Fig. 8) calculated by the low-order model, using the experimental observation (at t = 0) of velocities and temperatures. The pressure is normalized. Contour interval is 0.63 P_a. Negative values are shaded.
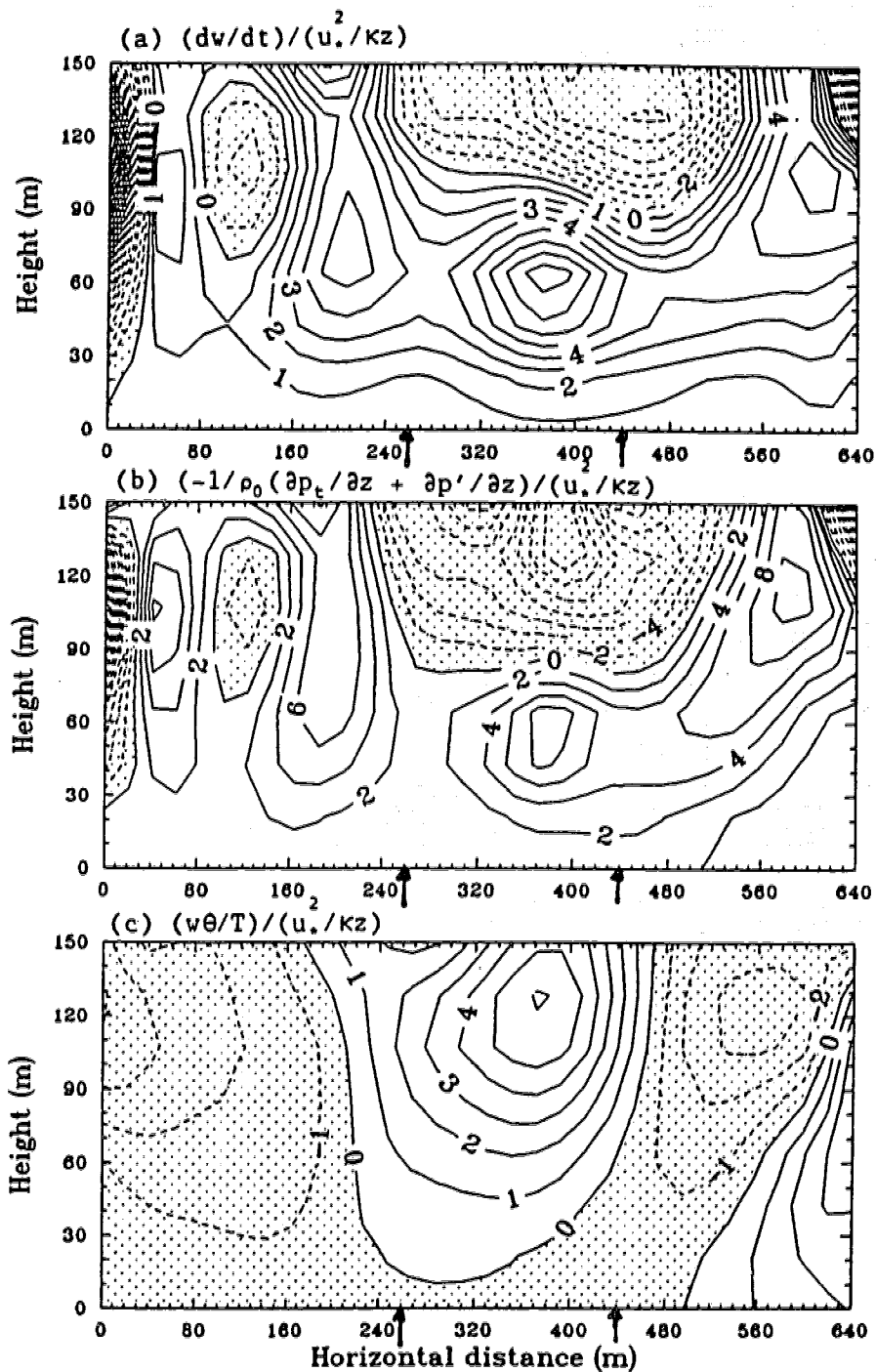
Fig. 10 (a) Vertical acceleration, dw/dt = ∂w/∂t +(U + u) ∂w/∂x + v∂w/∂z,
(b) pressure gradient, $-1/\rho_0(\partial p_t/\partial z + \partial p'/\partial z)$, and
(c) buoyancy θg/T fields of the CS. Variables are normalized.
κ = 0.4. Negative values are shaded.
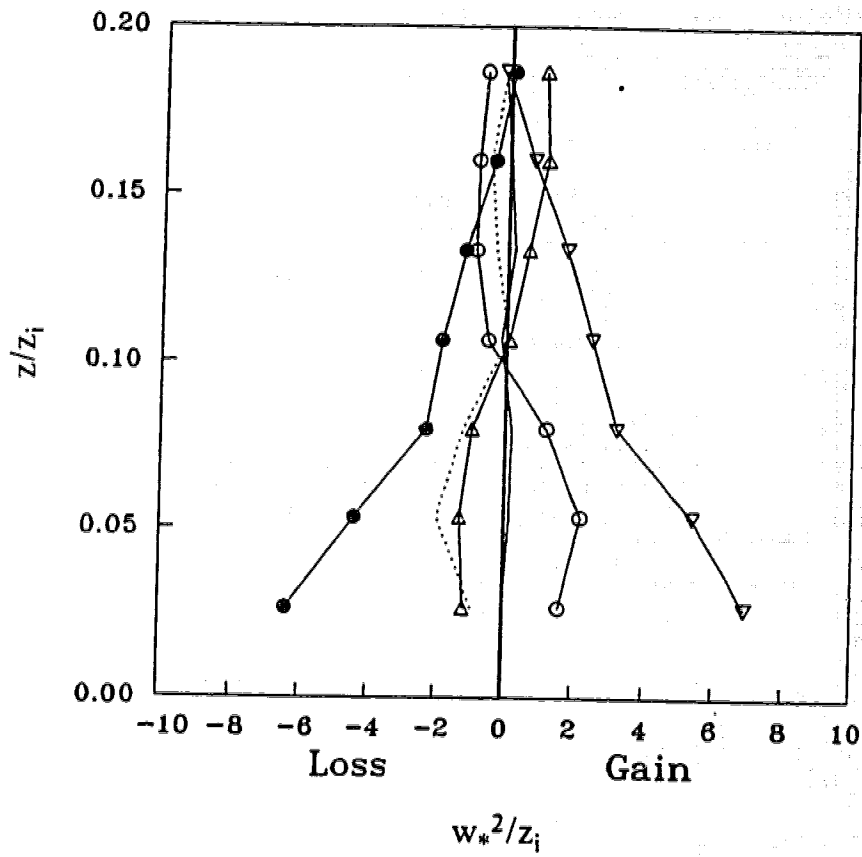
Fig. 11 Same as Fig. 3(b), except a translation velocity $U_t = 1.1\ U_m$ was used in the calculation.

(a) $U_t = 0.9\ U_m$

(b) $U_t = 1.1\ U_m$

Horizontal distance (m)
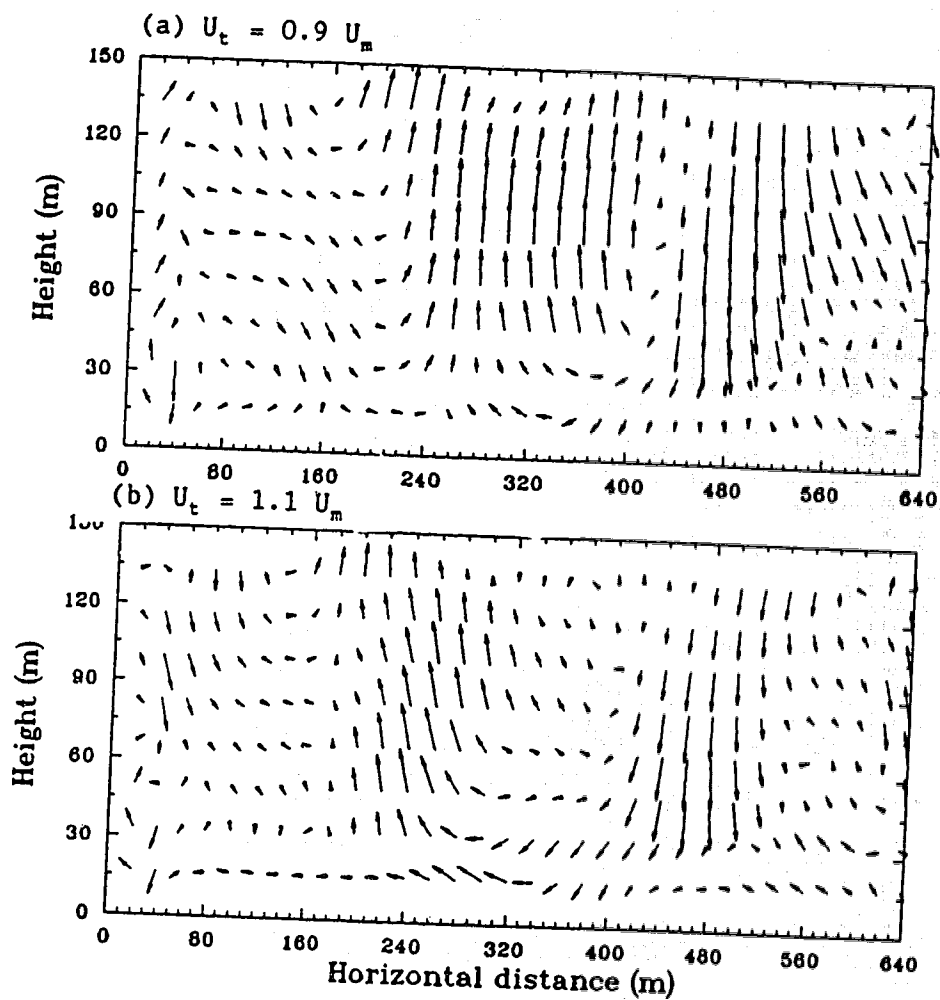
Fig. 12 Flow fields of the the convective plume (Fig. 8) after 2 min's evolution, calculated using (a) $U_t = 0.9\ U_m$ and (b) $U_t = 1.1\ U_m$.

Fig. 13. Trajectories of 10 fluid elements initially within the convective plume. The circles are the initial (t = 0) positions of the elements. The time interval between two arrows on any trajectory is 5 s.

REFERENCES

Antonia, R.A., A.J. Chambers, C.A. Friehe, and C.W. Van Atta, 1979: Temperature ramps in the atmospheric surface layer. J. Atmos. Sci., 36, 99-108.

Antonia, R.A., S. Rajagopalan, and A.J. Chamber, 1983: Conditional sampling of turbulence in the atmospheric surface layer. J. Climate App. Meteor., 22, 69-78.
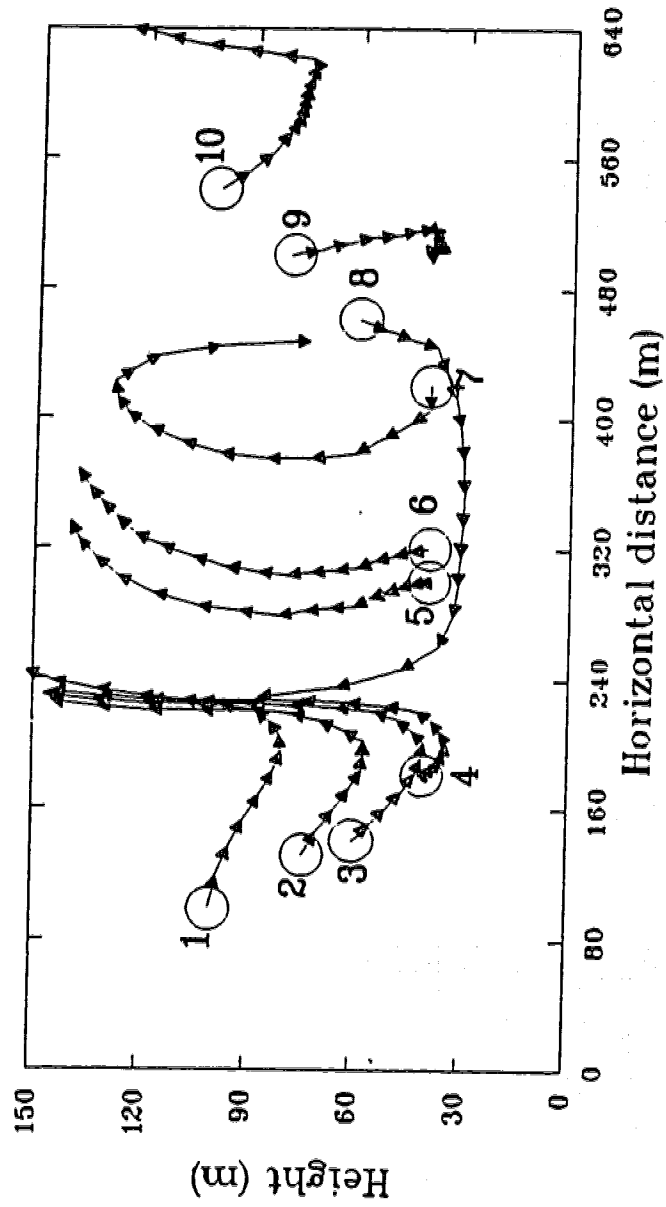
Batchelor, G.K., 1970: The Theory of Homogeneous Turbulence , Cambridge University press, London, pp 197.

Berge, P., Y. Pomeau, and C. Vidal, 1984: Order within chaos. John Wiley & Sons. N.Y., 274 pp.

Brown, R.A., 1980: Longitudinal instabilities and secondary flows in planetary boundary layer: a review. Rev. Geophys. Space Phys., 18, 683-697.

Businger, J.A., 1982: Equations and concepts. Atmospheric Turbulence and Air Pollution Modelling, F.T.M. Nieuwstadt and H. Van Dop, eds., Reidel Publishing Company, 1-36.

Davison, D.S., 1974: The translation velocity of convective plumes. Quart. J. R. Met. Soc. 100, 572-592.

Deardroff, J.M., 1971: On the Magnitude of the Subgrid Scale Eddy Coefficient. J. Comput. Phys. 7, 120-133.

Deardroff, J.W., and G.E. Willis, 1965: The effect of two dimensionality on the suppression of thermal turbulence. J. Fluid Mech., 23, 337-353.

Elliot, J.A., 1972: Microscale pressure fluctuations measured within the lower atmospheric boundary layer. J. Fluid Mech., 53, 251-383.

Greenhut, G.K., and S.J.S. Khalsa, 1982: Updraft and downdraft events in the atmospheric boundary layer over the equatorial Pacific ocean, J. Atmos. Sci., 39, 1803-1818.

Hunt, J.C.R., J.C. Kaimal, and J.E. Gaynor, 1988: Eddy structure in the convective boundary layer-new measurements and new concepts. Q.J.R. Meteorol. Soc., 114, 827-858.

Kaimal, J.C., 1974: Translation speed of convective plumes in the atmospheric surface layer.Q. J. R. Met. Soc., 100, 46-52.

Kaimal, J.C., and J.A. Businger, 1970: Case studies of a convective plume and a dust devil. J. Applied Meteoro., 9, 612-620.

Kaimal, J.C., Abshire, N.L., Chadwick, R.B., Decker, M.T., Hooke, W.H., Kropfli, R.A., Neff, W.D., and F. Pasqualucci, 1982: Estimating the depth of the convective boundary layer, J. Appl. Meteoro., 21, 1123-1129.

Lamb, R.G., 1982: Diffusion in the convective boundary layer. In Atmospheric turbulence and air pollution modelling, F.T.M. Nieuwstadt and H. van Dop (eds), D. Reidel Publishing Company, Boston, U.S.A., 159-230.

Lenschow, D.H., and P.L. Stephens, 1980: The role of thermals in the convective boundary layer. Bound.-Layer Meteorol. 19, 509-532.

Lumley, J.L., 1981: Coherent structures in turbulence. Transition and turbulence. R.E. Meyer. ed., Academic press. 215-242.

Mahrt, L., 1991: Eddy Asymmetry in the sheared heated boundary layer. J. Atmos. Sci., 48, 472-492.

Mason, P.J., and N.S. Callen, 1986: On the magnitude of the subgrid-scale coefficient in large-eddy-simulations of turbulent channel flow. J. Fluid Mech., 162, 439-462.

McBean, G.A., 1974: The turbulent transfer mechanisms: A time domain analysis, <fo74>Q. J. R. Met. Soc., 100, 53-66.

McBean, G.A., and J.A. Elliott, 1978: The vertical budgets of the turbulent velocity components and the velocity-pressure gradient interactions, J.Atmos. Sci., 35, 1890-1899.

Moeng and Wyngaard, 1986: Analysis of closures for pressure-scalar covariances in the convective boundary layer. J. Atmos. Sci., 43, 2499-2513.

Newton, C.W., 1967: Circulations in large sheared cumulrnimbus. Tellus XVIII, 768-713.

Rotta, J.C., 1951: Statistische Theorie nicht-homogener Turbulenz. Arch. Phys., 129, 547-572.

Rotunno, R., and J.B. Klemp, 1982: The influence of shear-induced pressure gradient on thunderstorm motion. Mon. Wea. Rev. , 110, 135-151.

Schmidt, H. and U. Schumann, 1989: Coherent structure of the convective boundary layer derived from large-eddy simulations. J. Fluid Mech., 200, 511-562.

Schols, J.L.J., A.E. Jansen, and J.G. Krom, 1985: Characteristics of turbulent structures in the unstable atmospheric surface layer. Boundary-Layer Meteor., 33, 173-196.

Schols, J.L.J. and L. Wartena, 1986: A dynamical description of turbulent structures in the near neutral atmospheric surface layer: the role of static pressure fluctuations. Bound.-Layer Meteoro. 34, 1-15

Schumann, U., and C-H. Moeng, 1991: Plume budgets in clear and cloudy convective boundary layers. J. Atmos. Sci., 48, 1758-1770.

Telford, J.W., 1970: Convective plumes in a convective field. J. Atmos. Sci., 27, 652-666.

Telford, J.W., 1986: Comment on "Large-scale eddies in the unstably stratified atmospheric surface layer. Part I: velocity and temperature structure" and "Part II: turbulent pressure fluctuations and the budgets of heat flux, stress and turbulent kinetic energy". J. Atmos. Sci., 43, 499-500.

Tennekes, H., and J.L. Lumley, 1971: A first course in turbulence. MIT press, Cambridge, Mass.

Wilczak, J.M., and J.E. Tillman, 1980: The three-dimensional structure of convection in the atmospheric surface layer. J. Atmos. Sci., 37, 2424-2442.

Wilczak, J.M., 1984: Large-scale eddies in the unstably stratified atmospheric surface layer. part I: velocity and temperature structure. J. Atmos. Sci., 41, 3537-3550.

Wilczak, J.M., and J.A. Businger, 1984: Large-scale eddies in the unstably stratified atmospheric surface layer. part II: turbulent pressure fluctuations and the budgets of heat flux, stress and turbulent kinetic energy. J. Atmos. Sci., 41, 3551-3567.

Williams, A.G., and J.M. Hacker, 1992: The composite shape and structure of coherent eddies in the convective boundary layer. Bound. - Layer Meteorol., 61, 213-245.

Wyngaard, J.C., 1980: The atmospheric boundary layer modelling and measurements. In Turbulent Shear Flows 2, Bradbury, L.J.S., F. Durst, B.E. Launder, F.W. Schmidt and J.H. Whitelaw (eds), Springer-Verlag, New-York, 352-365.

Wyngaard, J.C., 1982: Boundary layer modelling. Atmospheric Turbulence and Air Pollution Modellling., F.T.M. Niewstadt and H. Van Dop, eds., 69-106.

Wyngaard, J.C., 1988: Structure of the PBL. In Air pollution modeling. Eds. A. Venkatram, and J.C. Wyngaard, 9-62.

Young, G.S., 1988: Turbulence structure of the convective boundary layer. Part III: the vertical velocity budgets of thermals and their environment. J. Atmos. Sci. 45, 2039-2049.

Zeman, O., 1981: Progress in the modeling of planetary boundary layers. Ann. Rev. Fluid Mech., 13, 253-272.

Zhuang, Y., and J. Wilson, 1992: Extraction of the coherent motions in the atmospheric surface layer using Shot-Effect method. 10th Symposium on Turbulence and Diffusion, 230-233.

CHAPTER VI

GENERAL CONCLUSIONS

The objective of this thesis was to study transport properties of coherent motion in the atmospheric surface layer. I have achieved this by extracting and interpreting coherent structures from measured turbulence records, and by developing and applying a low-order model for a rational study of coherent structures in the convective atmospheric surface layer.

Two types of coherent motions, i.e., vortical motions in windbreak flows and convective plumes in the atmospheric surface layer, have been identified and discussed. It has been shown that both coherent motions play a major role in the turbulent transports, and largely shape the observed turbulent statistics, in their respective flows.

However, from the modelling point of view, the importance of the two coherent motions varies significantly. On one hand, because of the self-similar properties in the mixing region of a windbreak flow, the transport properties of the vortical motions can be adequately described by an eddy diffusivity concept. On the other hand, the turbulent transport associated with the convective plumes bear little relation to the local mean flow quantities, and change with atmospheric stability. Thus, ad hoc adjustment in an ensemble-average atmospheric turbulence model without explicitly taking the convective plumes into account is warranted.

This structural and deterministic study of turbulent flows by no means opposes the usefulness of the well established statistical

theories of turbulence. Rather, its objective is to provide detailed flow mechanisms for a better understanding and modelling of the flow. I believe that the detailed flow structures revealed in this study (Chapter V) have offered information that could be useful for improving ensemble-average turbulence models for flow prediction and air quality modelling. I also believe that incorporating coherent structures into a flow description will eventually reduce the parameterization needed to quantify the flow.

Appendix A   <u>QUADRANT ANALYSIS</u>
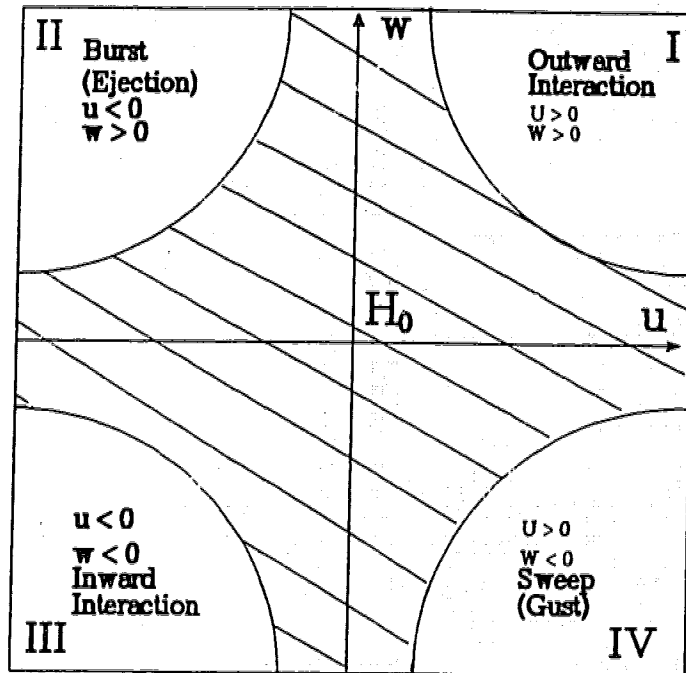
(Referred in Chapters II)

Figure 1A   Schematic representation of Quadrants and the hole
used for Quadrant analysis.

Quadrant analysis (Willmarth and Lu 1974) has been used to provide
detailed information about   the   momentum   transport   process.   This is
done by sorting the instantaneous   samples   of alongwind velocity u and
vertical velocity w into five bins,   depending on which quadrant of the
uw plane the sample occurred, and   whether or not the magnitude |uw| of
the event exceeds   (or   otherwise)   an   optional   threshold value $H_0 u_*^2$
(Fig. 1A).   The events   in   quadrants   II and IV, representing ejection

and sweep, respectively, make a positive contribution to the overall mean momentum flux $-\overline{uw}$; on the other hand, the motion in quadrants I and III, consisting turbulent outward and inward interactions, make a negative contribution to the overall momentum flux $-uw$.

The "hole" is a hyperbolically bounded region of events that are "small" in the sense that $|uw| \le H_0 u_*^2$, where H_0 is the "hole size" (Fig. 1A), a parameter free to be chosen to sort out dominant events. It is a subjective matter to choose the hole size, so as to reveal "the structure" of the momentum flux. The structure of momentum flux can be studied by sorting events as a flux fraction varying with H_0 in each of the quadrants. For example, at $H_0 = 0$, all samples of u and w will be sorted into quadrants I, II, III, and IV. By progressively increasing the magnitude of H_0, the samples that make only a small contribution to the Reynolds stress are sorted into the hole region, while the violent events, possibly corresponding to large-scale structures, remain and are identified within each quadrant.

The flux fraction $S_{i,H0}$ is defined as

$$S_{i,H0} = \frac{(uw)_{i,H0}}{|\overline{uw}|} , \tag{1A}$$

where the subscript i refers to quadrant number, and $(uw)_{i,H0}$ is the conditional average flux in ith quadrant at hole size H_0, defined as

$$(uw)_{i,H0} = \lim_{T\to\infty} \frac{1}{T} \int_0^T uw\, I_{i,H0}\, dt , \tag{2A}$$

and $I_{i,H0}$, the indicating function, is

$$I_{i,H_0} = \begin{cases} 1 & \text{if } u, w \text{ lies in the } i\text{th quadrant and } |uw| \geq H_0 |\overline{uw}| \\ 0 & \text{otherwise} \end{cases} .$$

Obviously, if $H_0 = 0$, we obtain from (1A)

$$\sum_{i=1}^{4} S_{i,H_0} = \overline{uw}/|\overline{uw}| = -1 \tag{3A}$$

Quadrant analysis has been used in many turbulent flows to study flux structures, and has provided considerable information about turbulent transport processes (see Antonia (1981) for a review).

References

Willmarth, W.W., and S.S. Lu, 1974: Structure of the Reynolds stress and the occurrence of bursts in the turbulent boundary layer. Advances in Geophysics, 18A, 287-314.

Antonia, R.A., 1981: Conditional sampling in turbulence measurements, Annual Review of Fluid Mechanics, 13, 131-156.

Appendix B Proper orthogonal decomposition

The proper orthogonal decomposition (POD) is a classical probability theory (Loeve 1955). It states that a variable fluctuation can be expanded as a series of deterministic functions (proper orthogonal functions) with random coefficients. Lumley (1967) introduced it to the field of turbulence research for objectively defining coherent structures from random turbulent signals. The major advantage of the POD is that it converges optimally faster in quadratic mean than any other expansion. For example, when an ensemble of events is selected from flow with high degree of organization, this decomposition has been found very effective in the sense that the first a few orthogonal functions will effectively retain most information in the velocity covariance of the selected events.

Because of its efficient data representation, recently the POD has been applied, in connection with the dynamical systems theory, to derive low-dimensional dynamical systems for turbulence studies (Sirovich 1987; Aubry et al. 1988). Readers are referred to Aubry (1991) for an extensive review of the POD and its applications in fluid dynamics. Here only a simple version of the POD (in time domain) will be described.

Suppose $f_1(t)$, $f_2(t)$,.. $f_N(t)$ are N realizations (or events) of a fluctuating signal, each of which can be either a single variable or a composite of variables, sampled periodically at t_m with a time interval, $\Delta t = (T_2 - T_1)/M$, within the closed domain $[T_1, T_2]$. We intend to find a function $\phi(t)$ within the domain $[T_1, T_2]$ that, in a statistical sense, "resembles" the dominant structure embedded in these realizations.

Let us pick the square of the correlation

$$\lambda = \frac{1}{N} \sum_{i=1}^{N} \frac{\left\{ \sum_{m=0}^{M} f_i(t_m)\phi(t_m) \right\}^2}{\sum_{m=0}^{M} \phi^2(t_m)} \tag{1B}$$

as a measure of the resemblance, where $t_m = T_1 + m\Delta t$. We select $\phi(t)$ by requiring λ to be maximum. This is done by applying the calculus of variations. Perturbing $\phi(t_m)$ by amount $\varepsilon\Delta\phi(t_m)$, then replacing $\phi(t_m)$ in Equation (1B) with $\phi(t_m)+\varepsilon\Delta\phi(t_m)$, and taking the limit

$$\lim_{\varepsilon \to 0} \frac{d\lambda(\varepsilon)}{d\varepsilon} = 0 \tag{2B}$$

we obtain

$$\sum_{m=0}^{M} R(t_m,t_k)\phi(t_m) = \lambda\phi(t_k) \quad , \tag{3B}$$

where λ is the eigenvalue, and

$$R(t_m,t_k) = \frac{1}{N} \sum_{i=1}^{N} f_i(t_m) \ f_i(t_k)$$

is the two-point covariance function formed from the N realizations, which is a $(M+1)\times(M+1)$ matrix. By definition $R(t_m,t_k)$ is

a. symmetric, i.e. $R(t_m,t_k) = R(t_k,t_m)$,

b. continuous if the sample functions are continuous and

c. defined on a closed integral $[T_1, T_2]$.

For $R(t_m,t_k)$ thus defined, it may be shown that (Loeve, 1955)

1. There are not one, but a discrete set of solutions to (3B), i.e.,

$$\sum_{m=0}^{M} R(t_m, t_k) \phi_n(t_m) = \lambda_n \phi_n(t_k) \quad , \qquad n = 1, 2, 3, \ldots N.$$

2. All the eigenvalues λ_n are real, non-negative and ordered such that $\lambda_1 > \lambda_2 > \ldots > \lambda_N > 0$. The sum of the the eigenvalues $\sum_{n}^{N} \lambda_n$ is called the total variance of the samples. The eigenfunctions ϕ_n are real and orthogonal to each other over the domain $[T_1, T_2]$, i.e.,

$\phi_1(t)$, explains a fraction of the total variance, $\lambda_1 / \sum_{n}^{N} \lambda_n$, and is orthogonal (i.e., uncorrelated in the domain $[T_1, T_2]$) to the rest of variance, and

$\phi_2(t)$, explains a fraction of the total variance, $\lambda_2 / \sum_{n}^{N} \lambda_n$, and is orthogonal to $\phi_1(t)$ and the rest of the variance, and

.   .
.   .
.   .

$\phi_N(t)$,   .

etc.

3. Any realization $f_i(t)$ can be expanded in the ϕ_n as basis functions

$$f_i(t) = \sum_{n=1}^{N} \alpha_{in} \phi_n(t) \quad , \tag{4B}$$

where

$$\alpha_{in} = \sum_{m=0}^{M} f_i(t_m) \phi_n(t_m) \quad \text{and} \quad \lambda_n = \sum_{i=1}^{N} \alpha_{in} \alpha_{in}$$

4. The covariance can be decomposed as

$$R(t_m, t_k) = \sum_{n=1}^{N} \lambda_n \phi_n(t_m) \phi_n(t_k) \qquad (5B)$$

Equation (3B) is the well-known problem of determining eigenvalues and eigenvectors of a matrix $(R(t_m, t_k))$. A standard solver of Equation (3B) can be found in the IMSL MATH/LIBRARY (IMSL 1989). The decomposition will reduce to the Fourier decomposition when the realizations are stationary (i.e., $R(t_m, t_k)$ depending only on $|t_m - t_k|$).

References

Aubry, N., P. Holmes, J.L. Lumley, and E. Stone, 1988: The dynamics of coherent structures in the wall region of a turbulent boundary layer, J. Fluid Mech., 192, 115–173.

Aubry, N., 1991: On the hidden beauty of the Proper Orthogonal Decomposition, Theoret. Comput. Fluid Dynamics, 2, 339–352.

Sirovich, L., 1987: Turbulence and dynamics of coherent structures: I, II, III, Quart. Appl. Math. ,5, 561–590.

Lumley, J.L., 1967: The structure of inhomogeneous turbulent flows. In Atmospheric Turbulence and Radio Wave Propagation, A.M. Yaglom and V.I. Takarski (eds), 166–178, Moscow.

Loeve, M., 1955: Probability Theory, Academic Press, New York.

Appendix C   The Boulder Atmospheric Observatory

The Boulder Atmospheric Observatory 300-tower is a research facility operated by NOAA for studying the atmospheric boundary layer. It is located 25 km east of the foothills of the Colorado Rockies on a section of agricultural land, with gentle slopes in the immediate area. The instrumentation levels on the tower are distributed linearly with height, except for the lowest two levels (Table C1). Table C1 lists the standard measurements on the tower, including the characteristics of the sensors, their sampling rates, and the error estimates. The sonic anemometers at all levels are pulsed synchronously 200 times per second, but only 20-point nonoverlapping block averages of the readings are recorded. This is done to minimize aliasing in spectra computed from the time series. A detailed description of this facility, the associated remote sensing systems, and the data acquisition system is given by Kaimal and Gaynor (1983).

Extensive site evaluations have been performed to determine how the unevenness of the terrain influences the temporal and spatial structure of the boundary layer over the site (Schotz and Panofsky, 1980; Kaimal et al., 1982; Hunt et al., 1988). These studies have demonstrated that the measurements at this facility agree with those made over flat land.

The facility has been a site of many cooperative experiments. The archived data are generally available to external users. In addition, data acquisition at the site proceeds on a continuous basis even during periods between experiments. The data chosen in this study were collected as routine measurements in the summer 1986. The data were

selected on the basis of the data summary sheets, which provide twenty-
minute summary listings of mean winds, temperatures, dewpoints, Monin-
Obukhov length, variances and turbulent fluxes (momentum and heat) etc.

TABLE C1 BAO sensor characteristics and sampling rates.

Standard sensors	Location	Parameters measured	Rate sampled (s^{-1})	Response characteristic	Basic accuracy
Sonic anemometer	Eight levels (10, 22, 50, 100, 150, 200, 250, 300 m)	u, v, w (velocity fluctuations)	10	20-point low-pass filter (~ 5Hz cut-off)	> 1% or > 1 cm s^{-1}
Propeller-vane anemometer	Eight levels on the opposite side from the sonic anemometers	S, D (wind speed and direction)	1	1 m distance constant	~3%
Platinum wire thermometer	Attached to sonic probe	θ (temperature fluctuation)	10	5-10 Hz cut-off	~1% °C
Quartz thermometer	Eight levels	T (mean temperature)	1	~1 min time constant	0.05°C
Cooled-mirror hygrometer	Eight levels	T_d (dew point)	1	~1 s cycle time	0.5°C
Lyman-α hygrometer	On selected levels	q (specific humidity)	10	1-2 cm path averaged	5%
Absolute pressure	Surface, near tower base	P	1	3 min time constant	1 mb
Fluctuating pressure	Five surface locations	p	1	3 min time constant	1 mb
Solar radiation	Surface, 100 m W of tower	R	1	~5 min	~5%

APPENDIX D   DETAILED EXPRESSIONS OF THE LOW-ORDER EQUATIONS
(Referred in Chapter IV)

$$
\frac{d\alpha_m}{dt} = \iint \left\{ \left[\frac{\partial}{\partial x^i}(\sum_i^N \alpha_i \phi_i^u \sum_j^N \alpha_j \phi_j^u) + \frac{\partial}{\partial z^i}(\sum_i^N \alpha_i \phi_i^u \sum_j^N \alpha_j \phi_j^w) \right] \phi_m^u \right.
$$

$$
+ \left[\frac{\partial}{\partial x^i}(\sum_i^N \alpha_i \phi_i^u \sum_j^N \alpha_j \phi_j^w) + \frac{\partial}{\partial z^i}(\sum_i^N \alpha_i \phi_i^w \sum_j^N \alpha_j \phi_j^w) \right] \phi_m^w
$$

$$
\left. + \left[\frac{\partial}{\partial x^i}(\sum_i^N \alpha_i \phi_i^u \sum_j^N \alpha_j \phi_j^\theta) + \frac{\partial}{\partial z^i}(\sum_i^N \alpha_i \phi_i^w \sum_j^N \alpha_j \phi_j^\theta) \right] \phi_m^\theta \right\} dxdz
$$

Turbulence interaction
$\sum_{i,j=1}^{N} {}^1 c_{ij}^m \, \alpha_i \alpha_j$

$$
+ \iint \left\{ \left(\frac{\partial \tau_{12}}{\partial z} - \frac{\partial \overline{uw}}{\partial z} \right) \phi_m^u + \left(\frac{\partial \tau_{12}}{\partial x} - \frac{\partial \overline{w^2}}{\partial z} \right) \phi_m^w + \right.
$$

$$
\left. \left(\frac{\partial H_x}{\partial x} + \frac{\partial H_z}{\partial z} - \frac{\partial \overline{w\theta}}{\partial z} \right) \phi_m^\theta \right\} dxdz
$$

Subgrid turbulence
$\sum_{i,j=1}^{N} {}^2 c_{ij}^m \, \alpha_i \alpha_j$

$$
+ \iint \left\{ \left(\overline{U} \frac{\partial}{\partial x^i} \sum_i^N \alpha_i \phi_i^u + \frac{\partial \overline{U}}{\partial z} \sum_i^N \alpha_i \phi_i^w \right) \phi_m^u + \right.
$$

$$
\left(\overline{U} \frac{\partial}{\partial x^i} \sum_i^N \alpha_i \phi_i^w - \frac{g}{T} \sum_i^N \alpha_i \phi_i^\theta \right) \phi_m^w +
$$

$$
\left. \left(\overline{U} \frac{\partial}{\partial x^i} \sum_i^N \alpha_i \phi_i^\theta + \frac{\partial \overline{T}}{\partial z^i} \sum_i^N \alpha_i \phi_i^w \right) \phi_m^\theta \right\} dxdz
$$

Mean-turbulence interaction
$\sum_{i,j,k=1}^{N} c_{ijk}^m \alpha_i \alpha_j \alpha_k$

$$
+ \iint \left(-\frac{1}{\rho_0} \nabla p^* \cdot \phi_m^v \right) dxdz
$$

Pressure term

$$
m = 1, \ldots, N.
$$

where H_x, H_z are subgrid heat fluxes, and $\overline{U}$ and $\overline{T}$ are derived by Eq. (14).

Note that although $^1c_{ij}^m$ can be easily calculated using orthogonal

functions, $^2c_{ij}^m$ and c_{ijk}^m need to be evaluated at each time step because

of the required calculation of the absolute value of the strain rate in

the subgrid stress terms, and the mean flow quantities ($\bar{U}$ and $\bar{\bar{T}}$).

Therefore more detailed expression on the low-order equations is not

possible as far as the analytical expression is concerned.

Appendix E Flow Chart for Calculating the Low-Order Equations
          (Referred in Chapter IV)

INITIALIZATION

Step 1 Calculate the derivatives of the fifteen orthogonal functions obtained from Eq. (7), using Fourier Transform method (Eq. (25)) in x direction and finite difference in z direction
Step 2 A snapshot of a flow realization, represented by a set of expansion coefficients α_m obtained from Eq. (29), is selected as an initial condition
Step 3 Set the simulation time $T_s = 0$
Step 4 Set the desired duration of the simulation T_d

CALCULATION OF FLOW FIELD

Step 5 Form velocities, and their derivatives with Eq. (19) and the results saved in step 1, using the new expansion coefficients α_m.

Step 6 Obtain the current mean wind and temperature profiles using Eq. (14) as a negative feedback to stabilize the simulation

Step 7 Calculate the coefficients $c_{i,j}^m$, $c_{i,j,k}^m$ and pressure term in the low-order equations (Eq. (23))

DATA STORAGE AND STEP AHEAD

Step 8 Advance the expansion coefficients α_m using Eq. (23) and save the current values of α_m

If $T_s > T_d$ No

Yes

End